


Summer 7-9-2019

Characterization of single- and multi-phase shock-accelerated flows

Patrick John Wayne
University of New Mexico

Follow this and additional works at: https://digitalrepository.unm.edu/me_etds

 Part of the [Fluid Dynamics Commons](#), and the [Other Mechanical Engineering Commons](#)

Recommended Citation

Wayne, Patrick John. "Characterization of single- and multi-phase shock-accelerated flows." (2019).
https://digitalrepository.unm.edu/me_etds/170

This Dissertation is brought to you for free and open access by the Engineering ETDs at UNM Digital Repository. It has been accepted for inclusion in Mechanical Engineering ETDs by an authorized administrator of UNM Digital Repository. For more information, please contact amywinter@unm.edu.

Patrick John Wayne

Candidate

Mechanical Engineering

Department

This dissertation is approved, and it is acceptable in quality and form for publication:

Approved by the Dissertation Committee:

Professor Peter Vorobieff, Chairperson

Professor C. Randall Truman, Member

Professor Andrea Mammoli, Member

Professor Monika Nitsche, Member

Characterization of single- and multi-phase shock-accelerated flows

by

Patrick J. Wayne

B. S., Mechanical Engineering, University of New Mexico, 2012
M. S., Mechanical Engineering, University of New Mexico, 2015

DISSERTATION

Submitted in Partial Fulfillment of the
Requirements for the Degree of

Doctor of Philosophy
Mechanical Engineering

The University of New Mexico

Albuquerque, New Mexico

July, 2019

©2019, Patrick J. Wayne

Dedication

*For my Mother and Father; without their love and support, this would not have
been possible.*

Acknowledgments

I would first like to thank the many undergraduate and graduate students who have helped and guided me the past 8 years in the Shock Tube Lab at UNM: Mike Anderson, Joe Conroy, Ross White, Clint Corbin, Garrett Kuehner, Tennille Bernard, Dell Olmstead, Dylan Simons, Jason Yoo, Ignacio Trueba-Monje, Daniel Davis, Sean Cooper, Elizabeth Keller, Sumanth Reddy Lingampally, Daniel Freelong, Gregory Vigil, and Josh Ludwigen.

I would especially like to thank Dr. Peter Vorobieff and Dr. C. Randall Truman. They have both been examples of the type of engineer and person I want to be. Their advice, encouragement, and most of all, patience over the last 8 years has been invaluable; I cannot thank them enough.

Dissertation Committee Members

- Dr. Peter Vorobieff (Chair)
- Dr. C Randall Truman
- Dr. Andrea Mammoli
- Dr. Monika Nitsche

Funding

The work contained in this dissertation was supported by:

- Agent Characterization Threat Agent Science (TAS), RD-CB Basic and Supporting Science, Defense Threat Reduction Agency (DTRA) Project CB10-CBSFTE2-2-0071
- The National Nuclear Security Administration (NNSA) grant DE-NA-0002220
- The National Nuclear Security Administration (NNSA) grant DE-NA-0002913

Characterization of single- and multi-phase shock-accelerated flows

by

Patrick J. Wayne

B. S., Mechanical Engineering, University of New Mexico, 2012

M. S., Mechanical Engineering, University of New Mexico, 2015

Ph. D., Mechanical Engineering, University of New Mexico, 2019

Abstract

Experiments conducted in the Shock Tube Facility at the University of New Mexico are focused on characterization of shock-accelerated flows. Single-phase (gaseous) initial conditions consist of a heavy gas column of sulfur hexafluoride seeded with approximately 11% acetone gas by mass. Visualization of the image plane for gaseous initial conditions is accomplished via planar laser-induced fluorescence (PLIF) with a high-powered Nd:YAG ultraviolet laser and an Apogee Alta U-42 monochrome CCD camera, with a quantum efficiency $> 90\%$. Multi-phase (gas-solid) initial conditions consist of glass micro-beads deposited on small 1-cm diameter discs of specific surface chemistry, mounted flush with the bottom wall of the test section. Visualization of the resulting multi-phase instabilities is achieved via Mie-scattering of visible light (532nm wavelength) laser pulses and a Hadland Imacon 200, with an effective frame rate of 200×10^6 frames per second. Fundamental properties of disparate gas mixtures of sulfur hexafluoride and helium, subjected to shock wave acceleration, are also studied, with implications that kinetic molecular theory can account for discrepancies between theory and experiment.

Contents

Preface	1
Significance of Shock Waves	3
References	13
I Shock-Driven Particle Lift-Off from a Surface	
1 Shock-driven particle transport off smooth and rough surfaces	18
1.1 Introduction	19
1.2 Experimental Setup	22
1.2.1 Surface Chemistry and Particle Size	25
1.2.2 Measurement of adhesion force	27
1.2.3 Deposition of the Particle Layer	28
1.2.4 Data Collection Process	30
1.2.5 Recovery Process	31
1.2.6 Additional considerations for the experimental procedure . . .	31
1.3 Experimental observations	33
1.4 Analysis of respirable particle cloud growth	36
1.5 Conclusions and future work	43
References	45

CONTENTS

II Shock Interaction with Single-Phase Initial Conditions

2 Oblique shock interaction with a cylindrical density interface 49

2.1 Introduction 50

2.2 Experimental Arrangement and Diagnostics 51

2.3 Results and Discussion 53

2.4 Conclusions 58

References 59

3 Oblique shock interaction with a laminar cylindrical jet 61

3.1 Introduction 62

3.2 Experimental Results 64

3.2.1 Qualitative Data 65

3.2.2 Quantitative Analysis 67

3.3 Conclusions 69

References 70

III Fundamental Physics of Gas Mixtures with Shock Propagation

4 Investigation of Dalton and Amagat’s laws for gas mixtures with shock propagation 73

4.1 Introduction 74

4.2 Theory 75

4.2.1 Shock Wave Theory 76

4.3 Experimental Arrangement and Diagnostics 79

4.3.1 Calibration Procedure 80

CONTENTS

4.3.2	Shock Tube Procedure	82
4.4	Results and Discussion	84
4.5	Future Work	86
	References	88
5	Dalton's and Amagat's laws fail in gas mixtures with shock prop- agation	89
5.1	Introduction	90
5.2	Results	94
5.3	Discussion	98
5.4	Materials and Methods	102
5.4.1	Experimental setup	102
5.4.2	Thermodynamic models	104
5.4.3	Kinetic molecular theory	106
5.4.4	Statistical analysis	108
	References	112

List of Figures

0.1	Schematic of the shock tube in the Mechanical Engineering Department at the University of New Mexico. Length dimensions for each of the four sections are approximate.	3
0.2	x-t diagram of a Mach 1.40 experiment showing the progression of incident shock, rarefaction wave, and pressure distribution within the shock tube, where low pressure regions are colored yellow and high pressure regions are colored green. The blue dotted lines correspond to the upstream and downstream locations of the test section imaging window, and the brown dotted line shows progression of the contact surface. The driver gas is nitrogen and the shock wave propagates through air.	5
0.3	Computational fluid dynamics (CFD) cross-section of a developing mixing layer in an inertial confinement fusion (ICF) fuel capsule. . . .	9
0.4	Plot of the infrared transmission spectrum of pure sulfur hexafluoride. The x -axis is wavelength λ (μm), and the y -axis is percent transmission. This curve has been digitized and recreated from Ref [40]. . . .	12
1.1	Schematic of the shock tube facility. Shock direction is from right to left.	22

LIST OF FIGURES

1.2 Experimental arrangement for inserting surface samples with a layer of particles into the test section. Top: image and schematic of the mounting rod. Bottom: closeup of test section with adapter for the mounting rod, as seen from below. Arrow indicates the rod insertion direction. 24

1.3 View of micro-rough (left) and smooth (right) surfaces 26

1.4 View of atomic-force microscope cantilever tip with attached particle and schematic of a colloidal-probe adhesion force measurement. A. Cantilever tip initially not in contact with sample surface. B. Sample is slowly raised towards the tip; cantilever snaps onto the surface due to attractive forces. C. Sample continues to raise, cantilever beam deflects to a set point (pre-defined force). D. Sample is lowered, particle adheres until it snaps off surface. Then $F_{ad} = -kz$ (Hooke's Law). . . 28

1.5 Sonication and shock acceleration processes. Left – schematic of scintillation vial with surface sample attached to mounting rod during particle deposition in sonicator. Right – mounting rod with surface sample and deposited monolayer of particles in test section (blue line denotes shock front). 29

1.6 Top – view of rough surfaces with depleted outer layers (left) and unused rough surfaces (right). Bottom – view of a smooth surface with a broken mica disc (left) and a fresh smooth surface (right). Arrows point to the depleted or damaged areas. 33

LIST OF FIGURES

- 1.7 Image sequence of respirable particle transport by a Mach 1.67 shock off a smooth surface. Flow direction is from left to right, the first frame depicts the initial conditions just before the shock arrives, the time intervals between dynamic frames are 50 microseconds. Horizontal extent of each image is 6.5 cm. In each image, the extent of the space occupied by the particles is marked by a blue dotted line (before cloud forms) or rectangle (for images of clouds). Inserts show frame fragments containing the particles with $2\times$ enlargement and inversion, to simplify interpretation. The image of the initial conditions (top left) has been subtracted from each dynamic image to reduce glare. . . . 34

- 1.8 Image sequence of respirable particle transport by a Mach 1.67 shock off a rough surface. Flow direction is from left to right, the first frame depicts the initial conditions just before the shock arrives, the time intervals between dynamic frames are 50 microseconds. Horizontal extent of each image is 6.5 cm. In each image, the extent of the space occupied by the particles is marked by a blue dotted line (before cloud forms) or rectangle (for images of clouds). Inserts show frame fragments containing the particles with $2\times$ enlargement and inversion, to simplify interpretation. The image of the initial conditions (top left) has been subtracted from each dynamic image to reduce glare. . . . 35

LIST OF FIGURES

1.9 Initial conditions image (a) and comparison of two late-time images of respirable particle transport by a Mach 1.67 shock off a smooth surface (b) and off a rough surface (c). Flow direction is from left to right. Images (a) - (c) are inverted for ease of interpretation, black arrows show the streamwise extent of the particle cloud. The first non-inverted image (d) is a close-up of the particle cloud from the rough surface case (c). Note that the laser-illuminated particle clouds reflect in the far wall of the test section, producing a “ghost” image of the cloud, labeled “reflection” in (c). Images (e) and (f) show additional examples of clouds with Kelvin-Helmholtz vortex formation. Yellow arrows point to vortices. 36

1.10 Schematic of thresholding procedure to determine the particle-cloud width and height. The vertical line denotes the streamwise (x) location where the cloud upper edge coordinate is sought. The blue line shows the variation of pixel intensity in the corresponding pixel column, the edge y_{max} of the cloud at the given x is where the intensity decreases to half between its maximum and minimum in the direction away from the surface. The highest value of y_{max} within the horizontal extent of the cloud gives the cloud height. The cloud image is inverted, with the darker area corresponding to the cloud. 38

1.11 Evolution of the particle cloud widths. Solid and dashed horizontal lines refer to average heights after 150 μ s for the cases of rough and smooth surfaces respectively. 40

1.12 Downstream positions of leading and trailing edges of respirable particle clouds vs. time after shock acceleration. Cases of smooth and rough surfaces are considered. Tinted areas serve as guides for the streamwise extent of the particle clouds. 41

LIST OF FIGURES

2.1 Shock tube inclined to 30° . The driver and driven sections are separated by a polyester diaphragm. Pressure transducers are located on top of the driven section. Flow direction is from left to right. 52

2.2 Sketch of three-dimensional vorticity deposition showing (a) pressure and density gradients [8] and (b) air moving down the upstream edge of the column. 53

2.3 Areas of interest where measurements of KHI were taken for (a) 30° and (b) 20° inclination angles. The full cross-sectional extent of the test section of the shock tube is 7.62 cm, images at 20° were taken at a higher resolution, but the area of interest has the same physical dimensions. 54

2.4 Temporal evolution of KHI for $M = 2.00$, $\theta = 30^\circ$. Each image is labeled with actual time after shock acceleration and dimensionless time τ (Eq. 2.1). 55

2.5 Comparison of KHI vortices at different Mach numbers (as labeled) for 30° inclined shock tube. Mach number increases from left to right. 56

2.6 Comparison of KHI vortices at different Mach numbers (as labeled) for 30° inclined shock tube. At $M = 1.13$, vortices form on *both* sides of the high density region. 57

2.7 KHI wavelength λ vs. Mach number M for (a) 30° and (b) 20° inclination. The data suggest that λ decreases as inclination angle $\theta \rightarrow 0$. Power-law fits are used as a visual aid. 58

LIST OF FIGURES

3.1 (a) Schematic of shock tube at UNM showing the angle of inclination α , and the driver, driven, test, and run-off sections, respectively. (b) Cross-section view of the test section (7.62 cm \times 7.62 cm), showing the vertical and centerline imaging planes. (c) Schematic of the shock tube test section, where ΔV = velocity of air behind the shock (piston velocity), ρ_1 = density of air at room temperature and pressure, and ρ_2 = density of the injected material. 63

3.2 Sequence of images showing evolution of the heavy gas column accelerated by an oblique shock. Top: vertical plane, bottom: centerline plane. Here $M = 1.13$, $A = 0.61$, and $\alpha = 20^\circ$. Lighter colors (see color bar) correspond to regions of high SF₆/acetone concentration, and darker colors correspond to regions of lower density, with pure air colored black. 66

3.3 Image showing the effect of Mach number on KHI wavelength λ . As the Mach number increases, wavelength decreases. Inclination angle here is 20° and the Atwood number is 0.61. Mach numbers from left to right are $M = 1.13$, $M = 1.45$, $M = 1.70$, and $M = 2.00$ 67

3.4 (a) Centerline plane: graph of CRVP spanwise width w vs. dimensionless time τ , for each Mach number and inclination angle α . (b) Vertical plane: graph of normalized KHI wavelengths with respect to Mach number for inclination angles $\alpha = 20^\circ$ (red line), and $\alpha = 30^\circ$ (blue line). Here, $\lambda_c = \lambda/(\sqrt{MD_c \tan \phi})$ 68

4.1 Experimental setup used to calibrate the MCT detector. 80

4.2 Shock tube experimental setup showing the driver and driven sections of the tube as well as the configuration of the detector and infrared source, located coincident with the 4th downstream pressure transducer. 83

4.3 A sample signal from the MCT detector shown (a) before and (b) after application of the Savitzky-Golay smoothing algorithm. 85

LIST OF FIGURES

4.4 Calibration curve(s) generated using Matlab for 48.0 psia calibration cylinder chamber pressure. Upward facing triangles correspond to measurements taken with the infrared source and dark blue squares correspond to measurements taken with the source. Six samples at each temperature increment were taken. 86

4.5 Sample graph of the pressure and temperature traces obtained in a shock tube experiment, with a driver pressure of 166 psia. The pressure of the test gas in the driven section was 11.4 psia (local atmospheric pressure). 87

5.1 **Time history of recorded signals and post-shock pressure dependence on initial pressure ratio.** **A.** Sample pressure transducer (PT) and MCT detector signal traces, showing locations of incident and reflected shocks, as well as the 2 ms averaging window (dashed blue lines) used in data analysis. The black line is the signal trace from the 4th downstream PT, and the magenta line is the MCT signal trace. **B.-D.** Post-shock pressure, P_2 , versus pressure ratio, P_r for a 50/50 (by mole) binary mixture of SF₆ and helium, respectively. **E.-G.** Post-shock pressure versus pressure ratio for a 25/75 binary mixture of SF₆ and helium. In all panels (**B.-G.**), black symbols correspond to experimental values, blue symbols represent Dalton’s law predictions, and red symbols denote Amagat’s law predictions. Vertical error bars correspond to total uncertainty in post-shock pressure P_2 . Horizontal error bars are omitted as they do not extend past the physical size of the symbols. The driven pressure associated with each dataset is displayed above the corresponding panel. 93

LIST OF FIGURES

5.2 **Post-shock pressure variation with incident shock speed. A.**
Post-shock pressure (P_2) versus incident shock speed (u_1) for a 50/50
(by mole) binary mixture of SF₆ to helium, respectively. **B.** Post-
shock pressure versus incident shock speed for a 25/75 binary mixture
of SF₆ to helium. In both plots, experimental values are given by black
symbols, blue symbols correspond to Dalton’s law predictions, and red
symbols represent Amagat’s law predictions. Black arrows show the
direction of increasing driver pressure from 1006 kPa to 1282 kPa.
Vertical error bars correspond to the total uncertainty in post-shock
pressure P_2 (experimental measurements and theoretical predictions),
which includes random and systematic uncertainties. Horizontal er-
ror bars correspond to total uncertainty in velocity measurements.
Horizontal error bars for theoretical predictions are omitted, as the
uncertainty in incident shock speed for both thermodynamic laws are
identical to that of the experimental measurements. 96

LIST OF FIGURES

5.3 **Post-shock temperature dependence on initial pressure ratio.** In both plots, black symbols correspond to experimental values, blue symbols represent Dalton’s law predictions, red symbols denote Amagat’s law predictions. Blue and red dotted lines in both plots are curve fits to Dalton’s and Amagat’s law predictions, respectively; they are simply used as guides to the eye. Vertical error bars correspond to total uncertainty in post-shock temperature T_2 , which includes both random and systematic uncertainties. **A.** post-shock temperature (T_2) versus pressure ratio (P_r) for a 50/50 binary mixture of SF₆ to helium. Here, experimental values are closer to Dalton’s law predictions. **B.** post-shock temperature versus pressure ratio for a 25/75 binary mixture of SF₆ to helium. In contrast to data presented in **A**, experimental values for a 25/75 mixture are closer to Amagat’s law predictions. 98

5.4 **Kinetic theory correlations with incident shock speed.****A.** change in collision time, $\Delta\tau = \tau_{He} - \tau_{SF_6}$, for a 50/50 (by mole) binary mixture of SF₆ to helium, respectively. **B.** change in collision time for a 25/75 binary mixture of SF₆ to helium. In both plots, experimental values are given by black symbols, blue symbols denote Dalton’s law predictions, and red symbols represent Amagat’s law predictions. Vertical error bars correspond to total uncertainty in $\Delta\tau$, and horizontal error bars correspond to total uncertainty in velocity measurements. Similar to Fig. 5.2, horizontal error bars for theoretical predictions are omitted, and black arrows show the direction of increasing driver pressure from 1006 kPa to 1282 kPa. These data closely resemble the trends we observe above (Figs. 1-3). 101

List of Tables

1.1	Summary of experimental observations of respirable particle propagation. Cloud height and cloud propagation speed estimates are based on data at times after 150 μs	43
4.1	Pressures tested in the calibration process, according to driver pressure and initial conditions.	85
5.1	Statistical information of experimental measurements for a 50/50 binary mixture of SF ₆ and helium, where n is the number of samples, ν is the degrees of freedom (combined or otherwise), and t is the student's t -distribution value.	110
5.2	Statistical information of experimental measurements for a 25/75 binary mixture of SF ₆ and helium, where n is the number of samples, ν is the degrees of freedom (combined or otherwise), and t is the student's t -distribution value.	111

Preface

Draw from your past, but do not let your past draw from you.

– Master Bratac

I thought it best, given the unconventional nature of this dissertation, to provide some context before proceeding further. This thesis is a compilation of first-authored, peer-reviewed papers, based on the work I have done in the Shock Tube Facility at UNM for the past 8 years (although they do not comprise the entirety of my research). The manuscript consists of three parts (5 chapters), each of which involves interaction of shock waves with specific initial conditions; either single- (gas-gas) or multi-phase (gas-solid).

One important feature of the Shock Tube Facility at UNM I wanted to discuss is the modular design of the shock tube itself. There are four main sections: the driver (high pressure region), the driven (low pressure region), the test section (initial conditions), and the runoff. The test section is made of polycarbonate and can be modified to accommodate any type of initial conditions, e.g. a curtain of falling particles, or a small-diameter column of gas. Another key feature - which makes this shock tube unique - is that the entire tube can be tilted anywhere from horizontal (0°) to approximately 45° , in order to simulate oblique (or inclined) shock waves. In fact, in the experiments described in Part II, Chapters 2 & 3, data were collected at inclination angles of 20° and 30° .

Chapters 1 through 4 are written in a format indicative of a scientific journal: (1) Background and introduction to the research material, including references to similar work; (2) Experimental setup and/or theoretical basis; (3) Results of the investigation and a discussion of the implications; (4) a Conclusion section highlighting some of the more important observations and a description of future work. Chapter 5 (Part III) is arranged in a slightly unorthodox manner, due to the formatting rules and submission guidelines for the intended journal; a short introductory section is given, followed by the results of the experiment, and a brief conclusion. The experimental setup, an explanation of the theory involved, and statistical analysis section are provided afterwards. The citation for each journal article is provided as a footnote on the first page of each chapter.

Following this is a section devoted to providing the reader with background into shock wave research, including its significance in the present work.

– Patrick John Wayne

University of New Mexico
Mechanical Engineering Department
Albuquerque, NM
May, 2019

Significance of Shock Waves

A shock wave is a type of propagating discontinuity which travels faster than the speed of sound in a local medium. The propagation of a shock wave in any medium is associated with an *instantaneous* increase in pressure, temperature, and density; hence the term discontinuity, an instantaneous transition from one state to another. A shock tube is used to study planar shock wave interactions with various initial conditions (ICs). These can be single-phase gaseous ICs, or multi-phase ICs, consisting of a gas and embedded solid phase material. Consider the shock tube depicted in Fig. 0.1, which is indicative of the experimental shock tube in the Mechanical Engineering Department at the University of New Mexico (UNM). This tube consists of

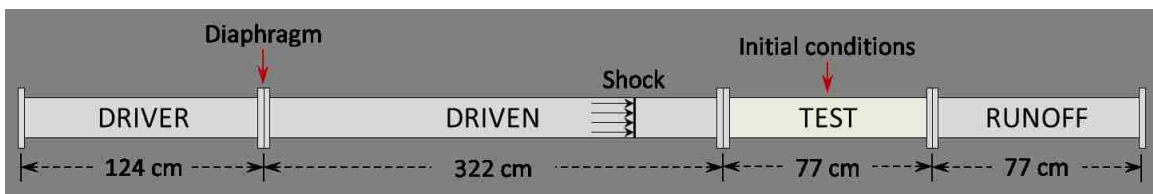


Figure 0.1: Schematic of the shock tube in the Mechanical Engineering Department at the University of New Mexico. Length dimensions for each of the four sections are approximate.

four main sections: the driver, driven, test, and runoff. To begin an experiment, the driver and driven sections are separated by a thin-film diaphragm (usually made of polyester, or mylar). The driver is then pressurized to some predetermined pressure

which depends on the desired strength of the shock wave; the driven, test, and runoff sections are initially at atmospheric pressure and temperature. Once the pressure in the driver stabilizes, a puncture rod tipped with a broad arrowhead is pneumatically fired into the diaphragm.

Two concurrent processes occur when the diaphragm is punctured. These processes are depicted in Fig. 0.2, which is a distance versus time (x - t) plot of a Mach 1.40 shock wave experiment on the UNM shock tube. Once the diaphragm is punctured (at $x = 0$, $t = 0$), a rarefaction (or expansion) wave is generated, traveling through the high pressure gas in the driver (Fig. 0.2, left), and a compression (or shock) wave is produced, traveling in the opposite direction (Fig. 0.2, right), through the low pressure gas in the driven, test, and runoff sections of the shock tube. Here, low pressure regions are colored yellow and high pressure regions are colored green. The rarefaction wave reflects off the back of the driver and travels down the length of the shock tube. If the driver is too short, the rarefaction wave can catch up with, and accelerate the incident shock. If the end of the shock tube is closed to the environment, the incident shock wave will reflect off the end of the tube and travel in the opposite direction (Fig. 0.2, right). Flow behind the incident shock wave is subsonic, with a velocity that depends on the Mach number of the experiment. Online gas dynamics calculators [1] can be used to determine this speed. For instance, flow behind the propagating shock wave in Fig. 0.2 travels at approximately 196.0 m/s.

The vertical dotted blue lines correspond to the up- and down-stream locations of the test section, where shock wave interactions with various initial conditions are recorded via high resolution cameras. The brown dotted line - which begins at the diaphragm - represents the edge of the contact surface; the interface separating the driven gas (air) and the driver gas (nitrogen).

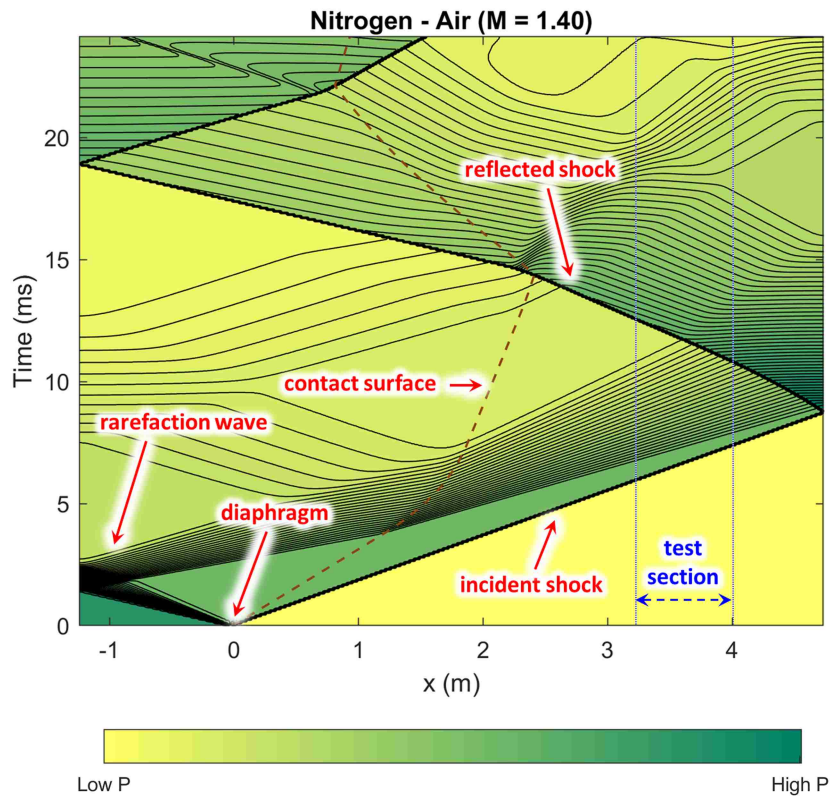


Figure 0.2: x-t diagram of a Mach 1.40 experiment showing the progression of incident shock, rarefaction wave, and pressure distribution within the shock tube, where low pressure regions are colored yellow and high pressure regions are colored green. The blue dotted lines correspond to the upstream and downstream locations of the test section imaging window, and the brown dotted line shows progression of the contact surface. The driver gas is nitrogen and the shock wave propagates through air.

The study of shock waves and their interactions with various media, such as solid particles, gases, and even plasma are essential in many engineering, medical, and physical phenomena. For instance, in the microelectronics industry, shock waves are used to remove micron-sized dust particles from silicon wafer surfaces [2]. In supersonic and hypersonic vehicles, aerospike are used as a means of drag and heat reduction by creating a detached shock ahead of the body. Extensive experimental [3, 4, 5, 6, 7] and numerical [8, 9, 10, 11] work has shown that the detached shock creates

a recirculation zone around the forebody of the vehicle, creating a more streamlined profile, thus reducing drag.

For the past three decades, shock waves have been used in the noninvasive disintegration of kidney stones by means of extracorporeal shockwave lithotripsy (ESWL), which is underwater focusing (using a shock wave) onto kidney stones from outside a human body [12, 13]. After the first successful attempt in 1980, ESWL was expanded to other types of stones, including gallbladder stones, pancreatic calculi, and salivary gland stones [14]. Shock waves have also been used in orthopaedics and traumatology, and in the treatment of horse tendons, ligaments, and bones in veterinary medicine [15].

In the field of astrophysics, several studies [16, 17, 18, 19] have been conducted into collisionless, relativistic shock waves (which propagate at a significant fraction of the speed of light), created by powerful sources such as gamma ray bursts, pulsar wind nebulae, and active galactic nuclei [20]. Shock waves are also generated by coronal mass ejections [21], and in the interstellar medium, where the strongest shocks are produced by supernovae [22].

Given the multitude of applications, it would be impractical to assume our current or future knowledge in shock waves is absolute. Therefore, it seems only prudent to focus research on specific cases of shock wave interactions. This paper presents several studies of shock wave effects on various initial conditions, including solid sphere particles, heavy gas columns consisting of sulfur hexafluoride and acetone gas, and disparate gas mixtures of sulfur hexafluoride and helium. Each study is a self-contained manuscript previously published in a peer-reviewed journal, with the exception of the last, which is currently under review. It would also be reasonable to preface these studies with an explanation of the motivation behind each, which not only includes advancing our knowledge of the subject material, but also applications

of the research to real-world situations.

Shock induced particle lift-off

The interaction of a shock wave with particles on surfaces is of particular interest in semiconductor and data storage industry, where even a submicron particle may induce fatal damages to the system [23]. In a process called laser shock cleaning (LSC), a high-powered laser pulse induces optical breakdown of the ambient gas close to the solid surface to be cleaned [24]. The shock wave created by this optical breakdown is followed by a high speed flow which detaches particles from the surface. In the LSC method, the surface is not directly exposed to the laser-pulse irradiation, which precludes the chance of potential damage in photosensitive parts, and a relatively large area can be cleaned by a single pulse [24].

In forensic science, particle lift-off from a surface is especially important in the detection of explosive residue, drugs, and biological contaminants. Shock-induced entrainment of particles may provide a suitable non-contact means to transport residue to analytical instruments, thus enhancing the detectability of contaminants [25].

In the medical industry, understanding how particles of different sizes (respirable and non-respirable) are lifted off surfaces (shock-induced or otherwise) is of particular importance as this can be applied directly toward the delivery of medicinal aerosols into the human lungs by way of dry powder inhalers (DPIs), or metered dose inhalers (MDIs). For diseases such as asthma, or COPD (chronic obstructive pulmonary disease), inhalation has become the primary route of administration of pharmacological agents [27]. Therefore, a base understanding of the physics involved in DPI and MDI particle flow is crucial for the effective delivery of the medication into the bloodstream.

The first part of this dissertation (Chapter 1) focuses specifically on respirable and non-respirable particle lift-off from micro-rough and smooth surfaces. Each of the surfaces has identical surface chemistries, with smooth surfaces consisting of a 1 cm diameter mica disc glued to a stainless steel disc, and micro-rough surfaces consist of a stainless steel disc roughened with 240-grit sandpaper, where surface features have a representative 2-micron scale. The particles used in this experiment consist of 3M glass micro-beads, with nominal size ranges of $0.5 \mu\text{m} - 10\mu\text{m}$ (respirable) and $20 \mu\text{m} - 50 \mu\text{m}$ (non-respirable).

The heavy gas interface and turbulent mixing

The Richtmyer-Meshkov instability (or RMI) develops when an interface between two fluids of different densities is impulsively accelerated (like the passage of a shock wave). This instability was first described by Robert D. Richtmyer in 1954 [28]. Several years later, Richtmyer's work was confirmed experimentally by Evgeny E. Meshkov [29]. A misalignment of the pressure and density gradients results in three-dimensional vorticity deposition on the gas-gas interface [30]. Any perturbation initially on the interface will be amplified following the passage of the shock wave. As the interface between the two fluids becomes more distorted, secondary instabilities, such as the Kelvin-Helmholtz shearing instability (KHI), develop and a region of turbulence and mixing ultimately results [31].

RMI (and correspondingly KHI) has been observed in many natural and engineering phenomena, from the evolution of supernova remnants, to high energy density physics, e.g. inertial confinement fusion (ICF). The goal of ICF is to initiate fusion in a small (spherical) capsule of deuterium-tritium gas. To reach the conditions of high temperature and density required for fusion, the capsule needs to be exposed to an enormous burst of energy (10^5 J) applied as symmetrically as possible and on

a time scale on the order of picoseconds (10^{-12} sec) [32]. As the burst of energy hits the outer shell of the capsule (ablator), the shell vaporizes and implodes onto the deuterium-tritium (D-T) fuel, accelerating the fuel toward the center of the sphere, compressing the gas to extremely high densities and temperatures so that ignition can occur. However, when the outer shell of the capsule implodes, sending a shock wave through the D-T fuel, small perturbations along the interface begin to amplify – due to RMI and other instabilities – and a mixing layer develops, causing non-uniform compression of the fuel capsule (Fig. 0.3).

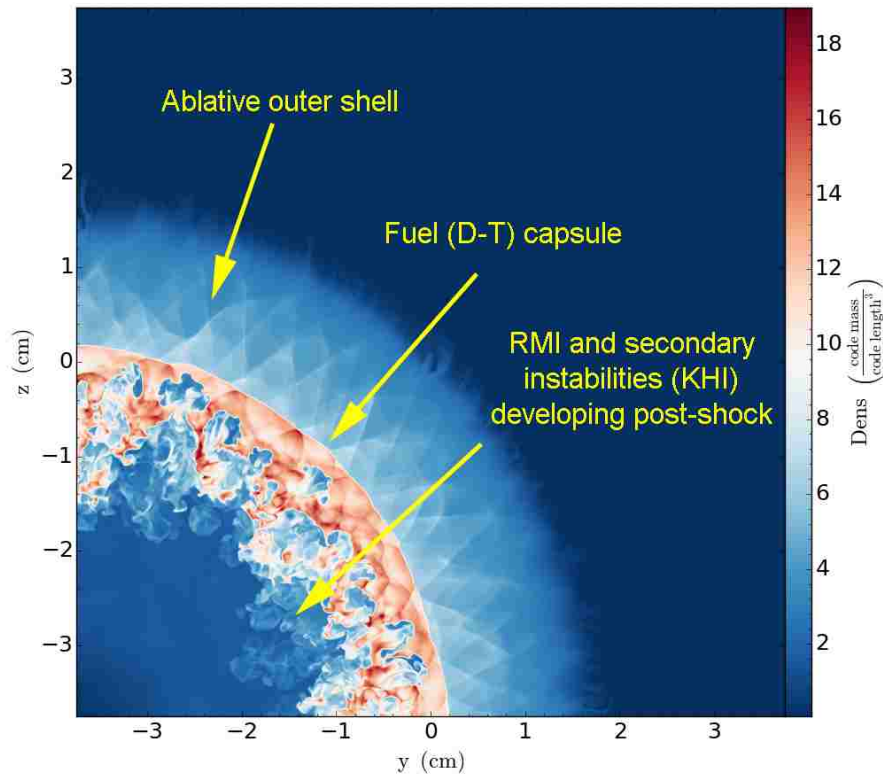


Figure 0.3: Cross-section of a developing mixing layer in an inertial confinement fusion (ICF) fuel capsule¹.

This complication preventing successful ignition (and fusion) requires further study of RMI and other instabilities that arise due to non-uniform implosion. Part II

(Chapters 2 & 3) of this dissertation is focused mainly on secondary instabilities, such as Kelvin-Helmholtz instabilities, developing from inclined shock interaction with a heavy gas column. The results of the experiments described in this section may aid future researchers in developing a method of mitigating mixing in ICF experiments, as well as help describe the evolution of natural astrophysical phenomena.

Gas mixtures and thermodynamic models

Gas mixtures affect our everyday lives and are prevalent throughout the universe - from the air we breathe to the solar system's largest anticyclonic storm on Jupiter (Great Red Spot). Applications range from the automotive industry [33] and SCUBA diving [14], to turbulence intensification in free convection flows [35, 36]. In many analytical and computational models used to describe the behavior of gas mixtures, classical thermodynamic laws, such as Dalton's law of partial pressures and Amagat's law of partial volumes, are used to predict properties of the mixture. The third part of this dissertation describes experiments aimed at determining the viability of these two laws in predicting post-shock behavior of a disparate gas mixture of sulfur-hexafluoride (SF_6) and helium (He). Specifically by measuring pressure and temperature immediately before and immediately after shock impact, then comparing these measurements with theoretical predictions based on Dalton's and Amagat's laws.

While this endeavor might not seem so demanding at first, given the availability of fast-response pressure transducers available on the market, a significant problem lies in the method of temperature measurement and the time scale on which they are collected. For instance, a shock wave with a Mach number of 1.2 travels in air (at

¹Image taken from: <http://flud.aeromech.usyd.edu.au/index.php/projects/compressible-turbulent-mixing/>

normal atmospheric conditions) at roughly 413 m/s (1,355 ft/s). At this speed, the shock wave would traverse a distance of 6 meters – the entire length of the shock tube – in approximately 15 milliseconds. Currently, there exist no viable thermocouples capable of measurements on this time scale (or anywhere close to it). In addition, thermocouples are an intrusive measurement device; they must be placed in the bulk fluid flow to function properly.

The solution to the problem of temperature measurements is the use of an infrared detector (IR). Most IR detectors have ultra-fast response times (≤ 1 ms), and are inherently non-intrusive. They operate by measuring emission of infrared radiation from a target object, or in this case, fluid. Although this method of temperature measurement seems straight-forward, there is one caveat. Each detector is specific to the gas mixture being studied. Therefore, knowledge of the infrared absorption spectrum of the gas components is mandatory. For helium, this does present a problem. The IR absorption spectrum of helium is known only for very high temperatures and pressures [37, 38, 39], but there has been some research [40] documenting the absorption spectrum of sulfur hexafluoride. Figure 0.4 is a plot of the wavelength-dependent transmission spectrum of infrared light through pure SF₆ (digitized and recreated from Ref [40]). Peak absorption (corresponding to minimum transmission) of IR radiation occurs in the mid-IR range between 10 μm and 11 μm . However, several strong, secondary peaks are visible between 5 μm and 10 μm . The yellow tinted region in Fig. 0.4 corresponds to the wavelength range ($7.5 \mu\text{m} \leq \lambda \leq 8.5 \mu\text{m}$) chosen for these experiments.

Chapter 4 (Part III) provides a detailed description of the experimental setup, a comprehensive explanation of the theoretical models used, and some preliminary results. Chapter 5 expands on this work and provides a qualitative explanation for the observations, based on kinetic molecular theory.

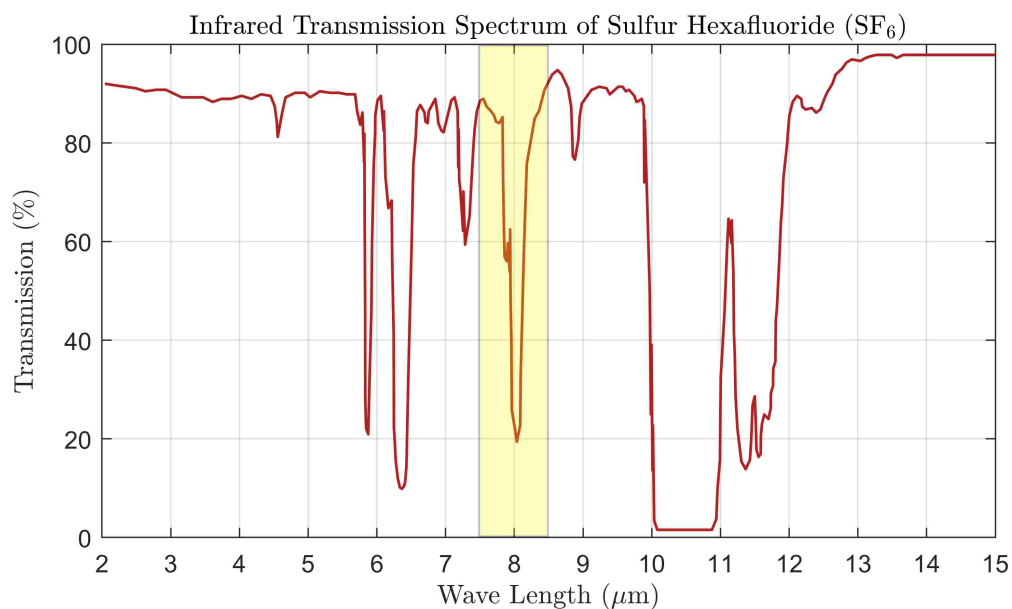


Figure 0.4: Plot of the infrared transmission spectrum of pure sulfur hexafluoride. The x -axis is wavelength λ (μm), and the y -axis is percent transmission. This curve has been digitized and recreated from Ref [40].

Note: Raw data from each experiment, Matlab code used to analyze results, and statistical information for all variables is available upon request.

References

- [1] "WiSTL Wisconsin Shock Tube Laboratory: Gas Dynamics Calculator," Aug. 7, 2008. Accessed on: April 20, 2019. [Online]. Available: <http://silver.neep.wisc.edu/shock/tools/gdcalc.html>
- [2] G. Jagadeesh, "Industrial applications of shock waves," *Proceedings of the Institution of Mechanical Engineers, Part G: Journal of Aerospace Engineering*, vol. 222, issue 5, pp. 575-583, 2008.
- [3] S. Srinath, and K. P. J. Reddy, "Experimental investigation of the effect of aerospike geometry on drag reduction and heat transfer rates at hypersonic Mach numbers," *International Journal of Hypersonics*, vol. 1, no. 2, pp. 93-114, 2010.
- [4] O. Wysocki, E. Schülein, and C. Schnepf, "Experimental study on wave drag reduction at slender bodies by a self-aligning aerospike," *New Results in Numerical and Experimental Fluid Mechanics IX. Notes on Numerical Fluid Mechanics and Multidisciplinary Design*, vol. 124, 2014.
- [5] C. Schnepf, O. Wysocki, and E. Schülein, "Wave drag reduction with a self-aligning aerodisk on a missile configuration," *Progress in Flight Physics*, vol. 9, pp. 149-172, 2017.
- [6] V. Kulkarni, "Effectiveness of aerospike for drag reduction on a blunt cone in hypersonic flow," *Journal of Spacecraft and Rockets*, vol. 47, no. 3, pp. 542-544, 2010.
- [7] V. Kulkarni, P. Kulkarni, and K. Reddy, *Drag reduction by a forward facing aerospike for a large angle blunt cone in high enthalpy flows*, Shock Waves, Springer, Berlin, Heidelberg, 2009.
- [8] T. Wan, and C. M. Liu, "Drag reduction optimization for hypersonic blunt body with aerospikes," *Journal of Aeronautics and Aerospace Engineering*, vol. 6, issue 4, p. 202, 2017.

References

- [9] N. Soori, "Numerical study of heat flux developed on an aero-spike structure in hypersonic flow," *2015 IEEE Aerospace Conference*, March, 2015.
- [10] C. Marley, and D. W. Riggins, "Numerical study of novel drag reduction techniques for hypersonic blunt bodies," *AIAA Journal*, vol. 49, pp. 1871-1882, 2011.
- [11] X. Sun, W. Huang, M. Ou, R. Zhang, and S. Li, "A survey on numerical simulations of drag and heat reduction mechanism in supersonic/hypersonic flows," *Chinese Journal of Aeronautics*, 2019.
- [12] K. Takayama, and K. Ohtani, "Applications of shock wave research to medicine," *Computational Methods and Experimental Measurements XII*, WIT Press, vol. 41, pp. 653-661, 2005.
- [13] G. G. Tailly, "Extracorporeal shock wave lithotripsy today," *Indian Journal of Urology*, vol. 29, no. 3, pp. 200-207, 2013.
- [14] A. M. Loske, "Medical and biomedical applications of shock waves: the state of the art and the near future," *30th International Symposium on Shock Waves I, July 2015 Tel Aviv, Israel*, G. Ben-Dor, O. Sadot, and O. Izra, Eds., 2017, pp. 28-34.
- [15] M. Thiel, M. Nieswand, and M. Dörffel, "Review: The use of shock waves in medicine – a tool of the modern OR: An overview of basic physical principles, history and research," *Minimally Invasive Therapy and Allied Technologies*, vol. 9, no. 3-4, pp. 247-253, 2000.
- [16] N. Borisov, and M. Fraenz, "Formation of a collisionless shock wave in a multi-component plasma," *Physics of Plasmas*, vol. 23, p. 122109, 2016.
- [17] D. B. Shaeffer, W. Fox, D. Haderberger, G. Fiskel, A. Bhattacharjee, D. H. Barnak, S. X. Hu, and K. Germaschewski, "Generation and evolution of high-Mach-number laser-driven magnetized collisionless shocks in the laboratory," *Physical Review Letters*, vol. 119, p. 025001, 2017.
- [18] M. S. Weidl, D. Winske, F. Jenko, and C. Niemann, "Hybrid simulations of a parallel collisionless shock in the large plasma device," *Physics of Plasmas*, vol. 23, p. 1222102, 2016.
- [19] A. Spitkovsky, "Particle acceleration in relativistic collisionless shocks: Fermi process at last?," *The Astrophysical Journal*, vol. 682, pp. L5-L8, 2008.
- [20] M. Lemoine, and G. Pelletier, "Particle acceleration at relativistic shock waves," *AIP Conference Proceedings*, November, 2011.

References

- [21] A. Petukhova, I. Petukhov, S. Petukhov, and L. Ksenofontov, "Solar energetic particle acceleration by a shock wave accompanying a coronal mass ejection in the solar atmosphere," *The Astrophysical Journal*, vol. 836, no. 1, pp. 36-45, 2017.
- [22] C. McKee, and D. Hollenbach, "Interstellar shock waves," *Ann. Rev. Astron. Astrophys.*, vol. 18, pp. 219-262, 1980.
- [23] Y. Zheng, B. Luk'yanchuk, Y. Lu, W. Song, and Z. Mai, "Dry laser cleaning of particles from solid substrates," *Journal of Applied Physics*, vol. 90, no. 5, pp. 2135-2142.
- [24] H. Lim, D. Jang, D. Kim, and J. Lee, "Correlation between particle removal and shock-wave dynamics in the laser shock cleaning process," *Journal of Applied Physics*, vol. 97, p. 054903, 2005.
- [25] G. Smedley, D. Phares, and R. Flagan, "Entrainment of fine particles from surfaces by impinging shock waves," *Experiments in Fluids*, vol. 26, pp. 116-125, 1999.
- [26] V. Rodriguez, R. Saurel, G. Jourdan, and L. Houas, "On solid particle jet formation under shock wave acceleration," *Physical Review E, Statistical, Nonlinear, and Soft Matter Physics*, vol. 88, p. 063011, 2013.
- [27] A. R. Clark, "Medical aerosol inhalers: Past, present, and future," *Aerosol Science and Technology*, vol. 22, pp. 374-391, 1995.
- [28] R. Richtmyer, "Taylor instability in shock acceleration of compressible fluids," Tech. Rep. LA-1914, Scientific Laboratory of the University of California, Los Alamos, New Mexico, 1954.
- [29] E. E. Meshkov, "Instability of the interface of two gases accelerated by a shock-wave," *Izv. AN SSSR, Mekh. Zhidk. Gaza*, vol. 5, no. 5, pp. 151-157, 1969.
- [30] P. Wayne, *Analysis of Kelvin-Helmholtz instabilities developing from oblique shock interaction with a heavy gas column*, Master's Thesis, University of New Mexico, 2015.
- [31] M. Brouillette, "The Richtmyer-Meshkov instability," *Annu. Rev. Fluid Mech.*, vol. 34, pp. 445-468, 2002.
- [32] S. Pfalzner, *Series in Plasma Physics: An Introduction to Inertial Confinement Fusion.*, New York: Taylor & Francis, 2006.
- [33] G. Velasco, and J.-Ph. Schnell, "Gas sensors and their applications in the automotive industry," *J. Phys. E: Sci. Instrum.*, vol. 16, 1983.

References

- [34] A. Loske, "Fundamentals of SCUBA-diving physics," *International Journal of Sports Science*, vol. 3, issue 2, pp. 37-45, 2013.
- [35] A Campo, S. Chikh, and S. Sablani, "Optimal molar gas composition of selected gas mixtures with helium that maximize turbulent free convection along vertical plates," *Journal of Fluids Engineering* vol. 128, pp. 199-201, 2006.
- [36] C. Warner, and V. Arpaci, "An experimental investigation of turbulent natural convection in air at low pressure along a vertical heated flat plate," *International Journal of Heat and Mass Transfer*, vol. 11, pp. 397-406, 1968.
- [37] R. Tourin, P. Henry, and E. Liang, "Infrared spectra of nitrogen, argon, and helium plasmajets," *Journal of the Optical Society of America*, vol. 51, no. 7, pp. 800-801, 1961.
- [38] P. M. Kowalski, "Infrared absorption of dense helium and its importance in the atmospheres of cool white dwarfs," *Astronomy & Astrophysics*, vol. 566, L8, 2014.
- [39] U. Fantz, "Basics of plasma spectroscopy," *Plasma Sources Science and Technology*, vol. 15, pp. S137-S147, 2006.
- [40] R. T. Lagemann and E. A. Jones, "The infrared spectrum of sulfur hexafluoride," *Journal of Chemical Physics*, vol. 19, no. 5, pp. 534-536, 1951.

Part I

Shock-Driven Particle Lift-Off from a Surface

Chapter 1

Shock-driven particle transport off smooth and rough surfaces²

The behavior of respirable particles being swept off a surface by the passage of a shock wave presents an interesting but little-studied problem. This problem has wide-ranging applications, from military to aerospace, and is being studied both numerically and experimentally. Here we describe how a shock tube facility was modified to provide a dependable platform for such a study, with highly repeatable and well-characterized initial conditions. During the experiments, particle size distribution, surface chemical composition (that determines adhesion force between the particles and the surface), and the Mach number are closely controlled. Time-resolved visualization of the particle cloud forming after the shock passage provides insights into the physics of the flow, including the effect of the adhesion force on the growth of the cloud.

²Originally published as: P. Wayne, P. Vorobieff, H. Smyth, T. Bernard, C. Corbin, A. Maloney, J. Conroy, R. White, M. Anderson, and S. Kumar, "Shock-Driven Particle Transport Off Smooth and Rough Surfaces," *Journal of Fluids Engineering*, American Society of Mechanical Engineers, Vol. **135**, 061302-1 (2013).

1.1 Introduction

The study of particle/surface interactions has considerable relevance for practical applications in the fields of aerospace science, environmental health, chemical and biological warfare, respiratory drug delivery – such as dry-powder inhalers – and even the day-to-day operations at Transportation Security Administration (TSA) security checkpoints at airports and sea terminals, where particles re-aerosolized from a surface of an item under inspection can both yield useful information and present a threat. The need to understand how particles of different sizes are lifted from surfaces by shock waves is of particular interest in modeling a battlefield environment. The explosive forces from grenades, land mines, and even artillery fire can dislodge particles of different sizes, lifting them off surfaces into the post-shock flow. These particles, especially those of respirable size, can represent a significant threat to the troops on the ground, as well as the machinery that must operate on the battlefield. Among the potentially harmful particle types are not just chemical and biological warfare agents. Any particle of size that is sufficiently small to reach the deep lung of humans can do harm [1, 2, 3], or, on the contrary, be used for drug delivery [4].

At the same time, there are practically no systematic experimental studies of shock-driven particle advection or re-aerosolization from a surface in open literature. Shock-driven acceleration of *individual* spheres off a surface has been studied to assess the drag coefficient of a sphere in a non-stationary flow [5]. Also an applied problem rather similar to the one discussed in the present paper has been studied in some detail in relation to dust explosions, where dust particles are lifted from a surface by a passing shock wave generated by a gas explosion. In one such study [6], a layer of dust (black coal or silicon) was deposited onto a surface of a shock tube, and a parametric study of the post-shock propagation of the cloud was conducted for a range of Mach numbers from 1.4 to 1.6 and for dust layer thicknesses 0.1, 0.4, and 0.8 mm. That

Chapter 1. Shock-driven particle transport off smooth and rough surfaces

study found a substantial (on the order of 1 ms) delay between the shock passage and the dust cloud formation. The vertical velocity characterizing the cloud growth was also quantified, with prominent differences due to the cloud material. This study [6] was followed up by a numerical investigation [7], where the numerical results were compared with experiment, and the influence of different factors on the numerical model was considered. It was found that the addition of Saffman and Magnus lift forces to the model did not produce a significant improvement, while accounting for particle collisions produced better agreement with experiment. Several other noteworthy numerical studies have been conducted [8, 9, 10, 11, 12], taking into account effects of turbulence [9] and wall roughness [12]. Because of industrial and other applications, the interest to this problem is considerable, which makes the scarcity of well-quantified experimental studies even more notable.

In these and related problems, the formation of a dusty suspension behind a transient shock wave [13] is generally explained by the action of a system of compression and expansion waves formed due to successive reflection of the leading shock wave from the solid surface and cloud boundary.

The more general problem of shock-particle interaction has attracted more attention, especially recently [14, 15, 16, 17, 18, 19, 20, 21], with studies of both initially densely-packed and disperse particles presenting a considerable challenge both to experimentalists and to numericists because of the range of spatial and temporal scales in the problem and of the number of factors that have to be taken into consideration. Flow interaction with particles can be quite complicated, for example, including situations when a bow shock forms around a cluster of particles [14], and situations when the shock interacts with a disperse cloud of particles by accelerating the gas, with the particles lagging behind [16, 17, 19]. Again, numerical works dominate here, and relatively few experiments are available for quantitative validation of computational results.

Chapter 1. Shock-driven particle transport off smooth and rough surfaces

To gain a better physical understanding of the process of shock-driven advection of particles from a surface, it would be interesting to consider a problem where the initial conditions (ICs) in the experiment can be well characterized in terms of particle size, substrate features, and adhesion between the particles and the surface. The desire to present an experimental case that quantitatively describes all the aspects of a deliberately limited parameter space motivates the present study.

As part of a collaboration between the research groups at the Mechanical Engineering Department at the University of New Mexico (UNM) and at the College of Pharmacy, University of Texas (UT) - Austin, the authors modified an existing shock tube experimental facility to make it possible to observe and record the behavior of particles initially resting on a horizontal surface, as they are impacted by a shock wave and transported into the shock-driven flow. This ongoing investigation into particle advection will ultimately address the effects of variations in particle size, surface chemistry and roughness, as well as reactions to shock waves of different strength.

The question the present paper addresses is whether it is possible to discern variation in the particle cloud behavior due to a change in just one parameter (surface roughness). The narrative begins with a description of how the experiment was created, including an explanation of the challenges that needed to be overcome, followed by a detailed description of the entire data acquisition process and a demonstration of the results pertaining to the apparent relationship between the surface – particle adhesion force and the growth rate of the forming particle clouds.

1.2 Experimental Setup

The UNM shock tube [22] is a facility primarily dedicated to studies of shock interaction with gaseous density interfaces (Richtmyer-Meshkov instability (RMI) and its recently discovered multiphase flow analog [19]; also see Section 1.4 for more details). During experiments, the driver section (Fig. 1.1, right) is pressurized with helium to a prescribed pressure. A Mylar diaphragm initially separates the driver section from the driven section (which is filled with air at atmospheric pressure). The diaphragm is then punctured by a solenoid-driven puncturer, releasing a planar shock wave.

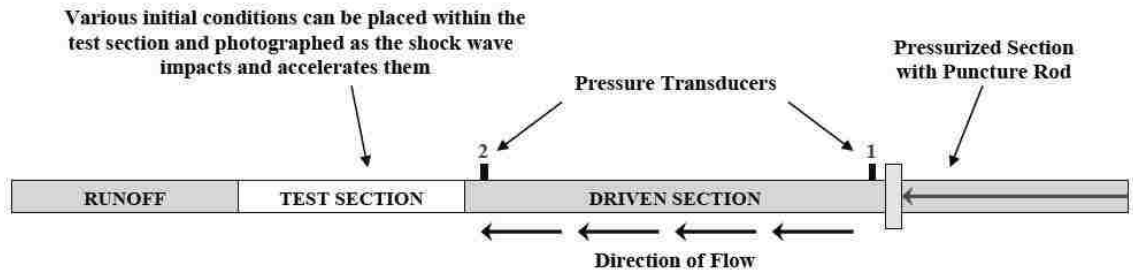


Figure 1.1: Schematic of the shock tube facility. Shock direction is from right to left.

The UNM shock tube has a square cross-section (7.62 cm). The driver section pressure prior to the diaphragm puncture is monitored with an Omega PX303 electronic pressure transducer. The maximum design Mach number of the facility with helium as the driver gas, as determined by the peak pressure the driver section can sustain, is $M = U_s/a = 4.1$, where M is the Mach number, U_s is the velocity of the shock front, and a is the speed of sound in air. The creation of the experiment was initially very simple. The shock tube already had timing (Stanford Research DG-535 digital delay generators) and diagnostic instrumentation (National Instruments NI-5133 digital oscilloscope and two Omega DPX101-250 pressure transducers

with Omega ACC-PS1 power supplies), but was not properly set up to conduct the particle/surface interaction experiment. Figure 1.1 shows a schematic of the shock tube proper. The test section, made of clear polycarbonate, is removable and can be modified to permit experimentation with any number of initial conditions.

The first task in conducting surface advection studies lay in fabricating a test section that would make it possible to insert surface samples of prescribed size, roughness, and chemical properties flush with the bottom wall. That necessitated fabrication of adapters for the surface samples produced and characterized at UT-Austin (the samples were mounted on 10mm round stainless steel plates). Initially, for that purpose we used a simple aluminum plate and a nylon set screw mounted underneath the test section (Fig. 1.2), and a small aluminum rod used to hold the surface during the particle deposition process, transfer to the shock tube, and release of the shock. The central hole of the test section adapter was machined at just over 10mm in diameter, with a threaded hole drilled into the side of the plate to allow installation of a nylon set screw. This simple design allowed seating of the particle-laden surface flush with the bottom of the test section for every shot.

A rare-earth neodymium magnet was pressure-seated in the tip of the aluminum holder, allowing a secure hold on the surfaces for testing. The same holder was used to deposit the particle layer onto the surface using an ultrasonic bath, or sonicator. The sonicator uses sonic waves to disperse particles into a small cloud within the scintillating vial used to hold the particles, depositing them onto the surface.

Once the particles have been deposited onto the reference surface, the aluminum holder is securely placed into the test section (Fig. 1.5, right), making sure the surface is flush with the bottom wall. A diaphragm is then inserted between the driven and pressurized section (refer to Fig. 1.1) of the shock tube. The diaphragm is made of Mylar film or of plastic-coated paper, depending on the Mach number desired. The

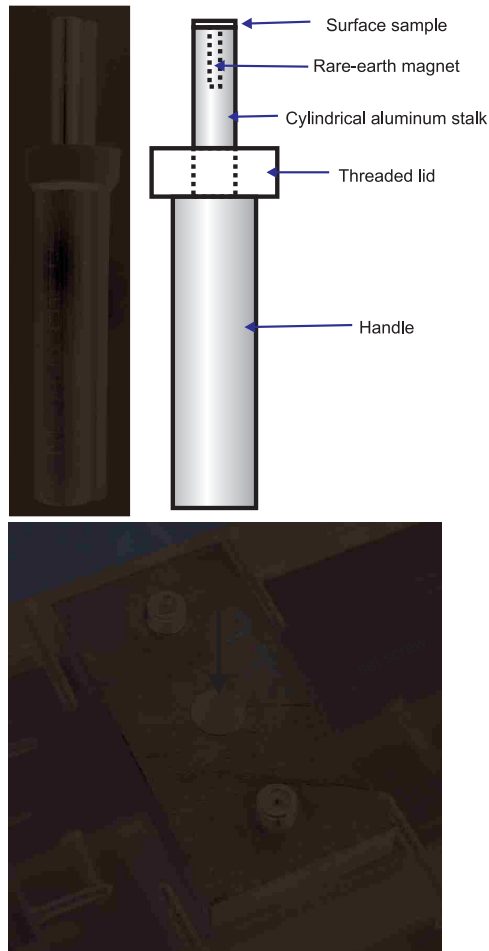


Figure 1.2: Experimental arrangement for inserting surface samples with a layer of particles into the test section. Top: image and schematic of the mounting rod. Bottom: closeup of test section with adapter for the mounting rod, as seen from below. Arrow indicates the rod insertion direction.

pressurized section of the tube is pressurized to a prescribed pressure point, with the pressure calculated using finite strength shock tube theory [23]. An electronic trigger activates the solenoid that drives the puncturer via a thin puncture rod in the pressurized section. The puncturer pierces the diaphragm and releases a shock wave that travels down the length of the tube toward the test section, impacting and accelerating the particles deposited on the sample surface. The pressure transducers are located 2.6 m apart on top of the driven section (Fig. 1.1, middle). They record the pressure pulses produced by the shock wave as it travels downstream. This data is subsequently recorded and displayed on an oscilloscope integrated with a laptop computer. The pressure trace information is subsequently used to confirm the exact Mach number of the shot.

The next subsections explain the details concerning the surfaces and particles used for the experiment.

1.2.1 Surface Chemistry and Particle Size

For initial experiments, a set of two surfaces with different roughness characteristics was selected (Fig. 1.3): smooth and rough. The smooth surfaces are comprised of a 1-cm diameter mica disc glued to a smooth stainless steel disc. The surface of the mica is then covered with a smooth silver coating, a 10.1 nm layer of gold, and a dodecanethiol outer layer. To prepare the surfaces with standardized surface chemistry, self-assembled monolayers (SAMs) of 1-dodecanethiol were formed by simply incubating the prepared surfaces with 1-dodecanethiol creating a uniform hydrophobic surface. Different surface chemistries will be investigated in later experiments using SAMs and thiol chemistry. The surface produced this way is smooth on the microscopic level, with average deviations from perfectly flat not exceeding 1nm. The micro-rough surface has the same surface chemistry as the smooth surface, but is in-

Chapter 1. Shock-driven particle transport off smooth and rough surfaces

stead a stainless steel disc roughened with 240-grit sandpaper. The silver, gold, and dodecanethiol coatings are the same, but the surface features of the rough surface have a representative 2-micron scale.



Figure 1.3: View of micro-rough (left) and smooth (right) surfaces

The particles used in the experiment are small glass beads. They were classified into two categories, respirable and non-respirable. For a particle to be respirable into the human airways, the particle must have an aerodynamic radius between 0.5 and 5 microns. It is around this particle size range that the physics of particle behavior transitions from a gravity influenced system (above 10 microns) to a Van der Waals - or weak electric force - dominated system [24]. This means that for smaller-sized, respirable particles, the weak adhesive forces that attract them to the surface disc can significantly influence how they are advected within the shock-driven flow.

Non-respirable particles are around 20 microns in diameter, and thus less inter-

esting in the context of investigating the effect of weak adhesive forces on the growth of the particle cloud. Thus in the following sections we will focus on the behavior of smaller (respirable) particles deposited onto smooth and rough surfaces.

1.2.2 Measurement of adhesion force

The adhesion force between the prepared surfaces and chosen particles was assessed with the colloidal probe technique [25], which employs the atomic force microscope (AFM) to probe the single-particle adhesion forces. The AFM uses a cantilever probe (sharp probe tips allow high topographical resolution, dull tips allow force measurement) which interacts with a surface; this interaction provides data about topography, elasticity, adhesion, or several other characterizations. A laser is focused onto the backside of the cantilever, and as the tip moves (due to surface interaction), the reflection of the laser onto a position-sensitive diode changes, providing a voltage difference.

Figure 1.4 illustrates the measurement of adhesion force using the colloid probe technique. A probe with a particle glued to its tip is initially suspended above the surface (A). The surface is raised until the probe pops into contact due to attractive forces, which causes a dip in the deflection signal (B). The surface continues to rise, which deflects the cantilever in the opposite direction, until a predefined contact force is achieved (C). The surface is then retracted. Adhesion force keeps the particle attached to the surface, until the bending force in the cantilever overcomes the adhesion, and the tip snaps from the surface (D). The deflection signal can be calibrated to a z -axis distance (nm), which allows the measurement of the distance at which the colloid probe detached from the surface. Using Hooke's Law, and knowing the spring constant of the cantilever (which was previously calibrated), the force of adhesion, F_{ad} , is determined. The results presented in this paper were acquired at

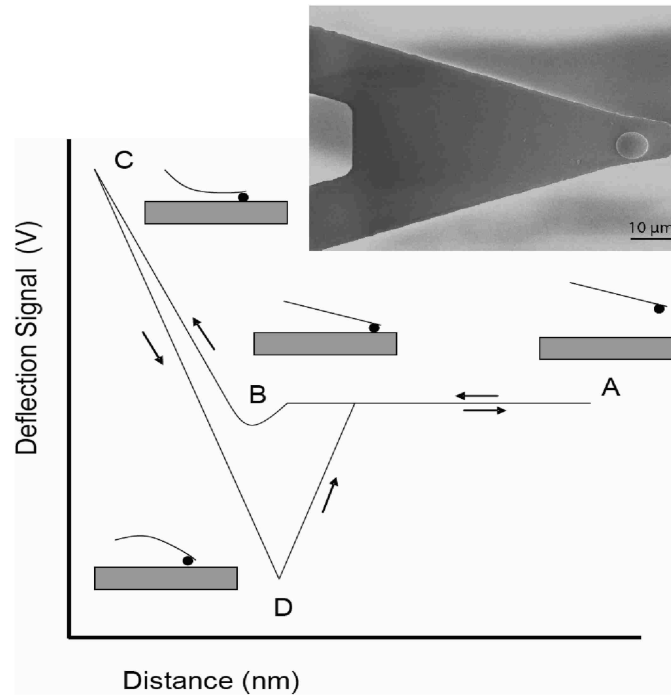


Figure 1.4: View of atomic-force microscope cantilever tip with attached particle and schematic of a colloidal-probe adhesion force measurement. A. Cantilever tip initially not in contact with sample surface. B. Sample is slowly raised towards the tip; cantilever snaps onto the surface due to attractive forces. C. Sample continues to raise, cantilever beam deflects to a set point (pre-defined force). D. Sample is lowered, particle adheres until it snaps off surface. Then $F_{ad} = -kz$ (Hooke's Law).

the University of Texas AFM facility with an Agilent 5500 atomic force microscope.

1.2.3 Deposition of the Particle Layer

As stated previously, an ultrasonic bath (sonicator) was used to deposit the particles on the surface samples. Figure 1.5 shows a schematic of this process. The same aluminum rod used to mount the surfaces within the test section is also used in the sonication process. The surface is attached to the tip of the rod and then inserted into a low-potassium glass scintillation vial, filled with a small amount (~ 1 mg) of the

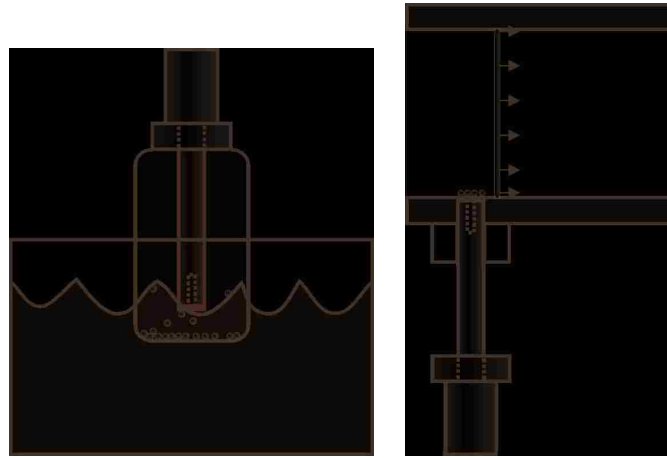


Figure 1.5: Sonication and shock acceleration processes. Left – schematic of scintillation vial with surface sample attached to mounting rod during particle deposition in sonicator. Right – mounting rod with surface sample and deposited monolayer of particles in test section (blue line denotes shock front).

particles. Once the vial is placed into the ultrasonic bath, the sonic motion disperses the particles into a thin cloud. The particles are attracted to the top of the surface by weak electrostatic forces. The goal of the sonication process is to produce a uniform coat of particles on the entire sample. The coating quality is checked visually with the naked eye and with a $30\times$ optical microscope. Sonication times can run anywhere from 20 seconds to 15 minutes. The authors tried to find a correlation between sonication times and either ambient temperature or humidity, but could not obtain a statistically meaningful answer, leaving the variation in sonication time a subject for further study. The properties of the surrounding environment are likely to play a role in particle distribution, but this role is rather subtle within the controlled lab environment, where the temperature only fluctuates within $\pm 2^\circ\text{C}$ from the average value of 20°C , and the relative humidity does not usually exceed 19%. However, the distance between the surface and the bottom of the scintillation vial is extremely important to particle deposition, as described below.

1.2.4 Data Collection Process

The initial conditions and evolving shock-accelerated particle clouds are imaged with an ultra high-speed Hadland IMACON 200 imaging camera, which is capable of framing rates up to 200 million frames per second. The CCD (charge-coupled device) chip on the camera has 14 separate CCD planes. The optical signal is passed through a microchannel intensifier, making it possible to individually adjust gain for each CCD. The camera also provides control for frame exposure durations, timing, and aperture (the latter is the same for each frame). Therefore, the individual frames can be set to capture the initial conditions before the shock wave impacts them, and any subsequent frames set in microsecond intervals to capture the evolution of the particle cloud.

For the experiments described here, the test section is illuminated with a vertical laser sheet produced by two 532nm double-pulsed lasers (New Wave Research Gemini PIV). This leaves four laser pulses at our disposal, allowing the capture of four nominally identical frames of initial conditions followed by four dynamic frames of post-shock particle cloud evolution. These laser pulses are timed to expose four different CCD planes of the IMACON camera. The images are stored on a hard drive of the computer attached to the camera in grayscale TIFF format (1260×900 resolution, 10 bits per pixel) for later data analysis and image processing.

As an alternative to the Imacon 200, an Apogee Alta U42 camera was used. It has a single CCD, facilitating the capture of only two images per experiment (initial conditions and dynamic exposure). The advantages of the Apogee camera are higher spatial resolution (4 megapixels vs. 1 megapixel for the Imacon), more grayscale bits per pixel (16 vs. 10), and very low noise levels. Unlike the Imacon, the single CCD of the Apogee camera is not intensified, but has a very high quantum efficiency ($\sim 90\%$). The images characterizing the late-time evolution of the particle cloud were acquired

with this camera, using the same laser illumination as described above, but only with two images captured per experiment – initial conditions and a single dynamic exposure.

1.2.5 Recovery Process

After each firing of the shock tube, the aluminum holder is recovered from the test section and the reference surface cleaned, prior to any further particle deposition. The cleaning process is relatively straightforward. The sample is cleaned with gentle application of compressed air. If visual inspection reveals any remaining particles, a small CCD sensor swab moistened with 96% ethanol is gently run across the reference surface to wipe away any debris left behind after the shock passage, then dried using a small can of compressed air. A final evaluation of the surface is performed (by optical microscopy) to verify that the surface is clean, then particles are re-deposited onto the surface via the ultrasonic bath and the entire process is repeated.

1.2.6 Additional considerations for the experimental procedure

Although these processes seem simple at first, there are plenty of opportunities for mistakes. Several unexpected challenges in implementing the experimental procedure were encountered during the experiments. The first such challenge, mentioned above, is the variability in the time it takes to deposit a monolayer of particles onto a surface. As the environment within the laboratory is reasonably well controlled in terms of temperature and humidity, this variability likely related to some feature of the sonication process itself. Another significant problem that emerged during the sonication was the fragility of the scintillation vials. The authors determined that

Chapter 1. Shock-driven particle transport off smooth and rough surfaces

each scintillation vial should be used for no longer than two minutes at a time in the sonication bath (or the vial would shatter). Vials would need to be exchanged during the sonication process, if particle deposition did not complete within a two-minute interval.

Fragility of the test surfaces themselves also presented a challenge in shock-driven flow studies. After repeated experiments with the same surface, especially at high Mach numbers, the fragile protective layer of dodecanethiol and the gold/silver coatings underneath became damaged. Figure 1.6 shows two micro-rough surface samples that have been used for a number of experiments (top left) and two unused samples (top right). These problems with reference surfaces are not limited to rough coatings. The smooth coated mica surfaces are exceptionally fragile to the shock wave and cleaning processes. The mica/stainless steel interface is particularly susceptible to any shearing force, like that created after the shock wave encounters the surface covered with particles. If the surface does not sit flush with the bottom of the test section, there exists a risk of losing a portion of the mica disc to the shock-driven flow (as shown in Fig. 1.6, bottom left).

Another challenge faced during experiments with particle/surface interactions was apparently caused by static electricity. The test section of the shock tube is made of strong polycarbonate, but the only method of cleaning the test section involved the use of a micro-fiber sweep. This process created a large enough electrostatic force to dislodge the particles from the surface when inserted into the test section. This may seem like a trivial concern, but the amount of particles dislodged from the surface ranged anywhere from 10% to 50% of the total coat. To correct this problem, the aluminum flange of the test section was grounded directly to the distribution board located in the lab. This method did somewhat improve the situation, but a more permanent solution was needed. High-pressure air lines provided an alternative method of cleaning the test section, one that would not damage the polycarbonate

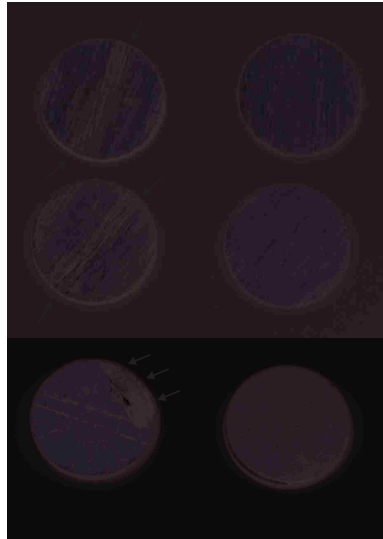


Figure 1.6: Top – view of rough surfaces with depleted outer layers (left) and unused rough surfaces (right). Bottom – view of a smooth surface with a broken mica disc (left) and a fresh smooth surface (right). Arrows point to the depleted or damaged areas.

walls, or deposit static electricity.

With the additional challenges described in this subsection carefully addressed, the initial conditions produced by the experimental setup described above are highly repeatable, producing consistent data from experiment to experiment. The following sections detail some of the data acquired, focusing on the differences in the post-shock flow that are likely attributable to differences in the adhesion force between the particles and the surface.

1.3 Experimental observations

Visualization of the images reveals subtle details of particle cloud formation, including features such as shear-induced vortices. Early-time evolution of the clouds shown

in the first figures is captured with the Imacon 200 camera, the late-time images are acquired with the Apogee camera.

The first image sequence (Fig. 1.7) reveals the onset of particle-cloud transport off a smooth reference surface. The particle-laden surface is approximately 1-cm in diameter as shown (upper left. $t = 0$). After the shock wave has passed the initial conditions, the particle cloud increases in both height (spanwise - normal to the surface) and length (streamwise). Each dynamic exposure is separated by exactly $50 \mu\text{s}$. The timing of the first exposure has some variability due to small fluctuations in the triggering system. Notice that by the last frame (lower right), most, if not all of the particles have been completely transported off the smooth surface.

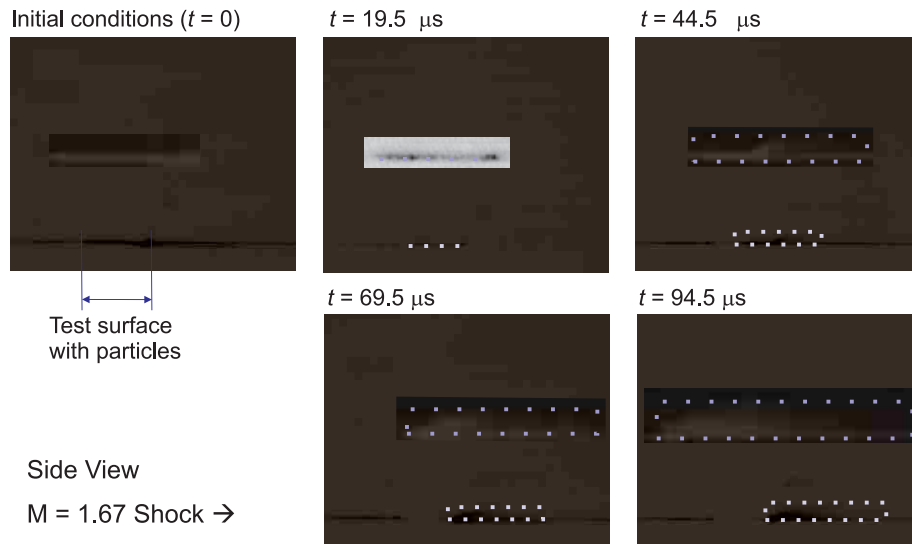


Figure 1.7: Image sequence of respirable particle transport by a Mach 1.67 shock off a smooth surface. Flow direction is from left to right, the first frame depicts the initial conditions just before the shock arrives, the time intervals between dynamic frames are 50 microseconds. Horizontal extent of each image is 6.5 cm. In each image, the extent of the space occupied by the particles is marked by a blue dotted line (before cloud forms) or rectangle (for images of clouds). Inserts show frame fragments containing the particles with $2\times$ enlargement and inversion, to simplify interpretation. The image of the initial conditions (top left) has been subtracted from each dynamic image to reduce glare.

The next set of images shows respirable particle transport off a micro-rough surface. Notice that in the first hundred microseconds after the shock, the leading edge of the cloud propagating downstream in Fig. 1.8 is not completely clear of the reference surface, but the overall cloud size appears larger.

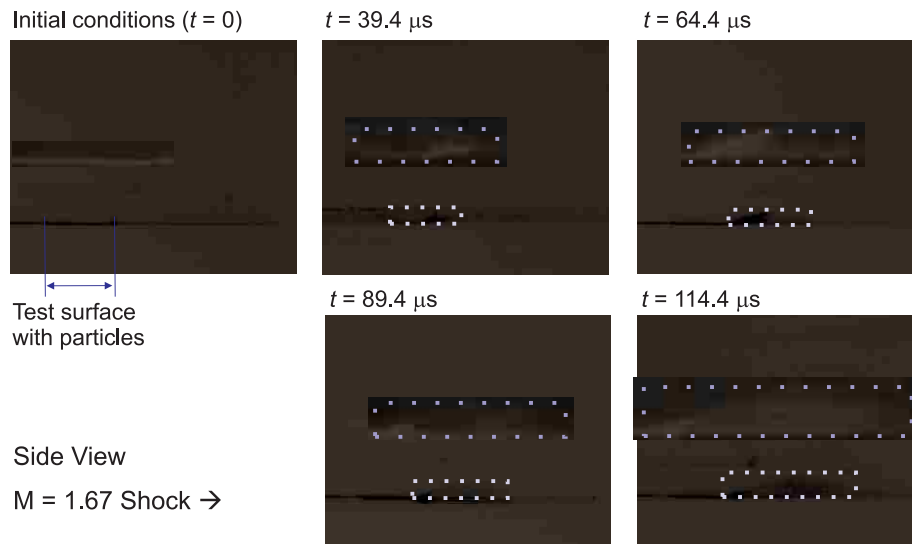


Figure 1.8: Image sequence of respirable particle transport by a Mach 1.67 shock off a rough surface. Flow direction is from left to right, the first frame depicts the initial conditions just before the shock arrives, the time intervals between dynamic frames are 50 microseconds. Horizontal extent of each image is 6.5 cm. In each image, the extent of the space occupied by the particles is marked by a blue dotted line (before cloud forms) or rectangle (for images of clouds). Inserts show frame fragments containing the particles with $2\times$ enlargement and inversion, to simplify interpretation. The image of the initial conditions (top left) has been subtracted from each dynamic image to reduce glare.

These early-time image sequences captured with the Imacon camera are complemented by later-time images captured with the Apogee camera. Figure 1.9 shows a comparison of two flow visualization pictures at about $300 \mu\text{s}$. These images show the differences in particle cloud extent and propagation speed more clearly, with the particle cloud lifted off the rough surface both moving and expanding faster. Late-time images also show formation of vortices (likely shear-driven) near the top edge

of the cloud. The next section describes quantitative measurements of cloud size extracted from the images.

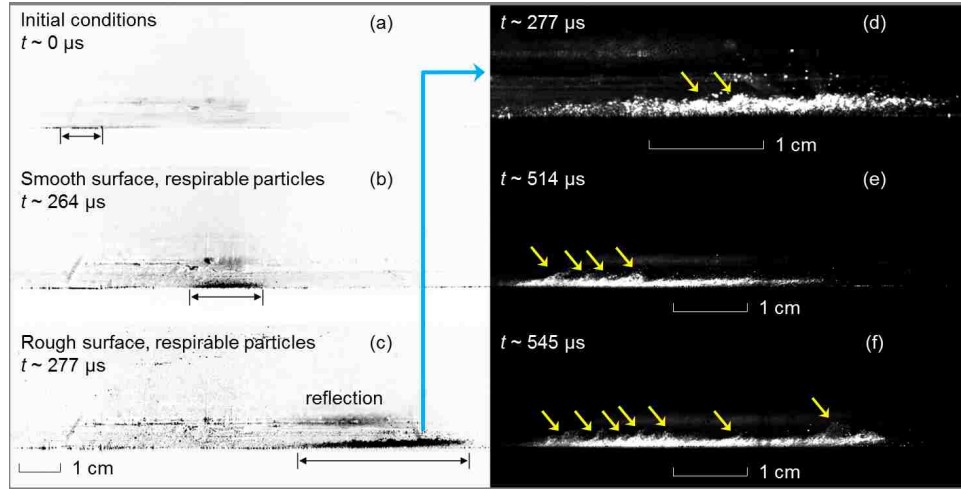


Figure 1.9: Initial conditions image (a) and comparison of two late-time images of respirable particle transport by a Mach 1.67 shock off a smooth surface (b) and off a rough surface (c). Flow direction is from left to right. Images (a) - (c) are inverted for ease of interpretation, black arrows show the streamwise extent of the particle cloud. The first non-inverted image (d) is a close-up of the particle cloud from the rough surface case (c). Note that the laser-illuminated particle clouds reflect in the far wall of the test section, producing a “ghost” image of the cloud, labeled “reflection” in (c). Images (e) and (f) show additional examples of clouds with Kelvin-Helmholtz vortex formation. Yellow arrows point to vortices.

1.4 Analysis of respirable particle cloud growth

The cloud dimensions (width – streamwise, and height – normal to the shock tube wall) were assessed as Fig. 1.10 illustrates. From each dynamic image used for quantification, the background image taken immediately before the experiment was subtracted. Then a bounding box containing the cloud was selected by one of the authors, and within this box, a simple technique was applied to find the leading, the trailing, and the top edge of the cloud (the bottom edge of the cloud always

being the shock tube wall). For example, to trace the top edge of the cloud, for each vertical column of pixels inside the bounding box, a pixel intensity minimum (corresponding to the particle-free flow) and maximum (corresponding to the cloud) were found. The vertical coordinate of the pixel where the intensity value decreased by half from the maximum was stored. This procedure was repeated for each column in the bounding box, and the maximum resulting coordinate was used to determine the cloud height. A similar procedure was applied to pixel rows in the bounding box to determine the streamwise extent of the cloud. The result was then checked by the program operator for consistency with visual observations and rejected if there was no such consistency. Overall, less than 2% of the instantaneous images were rejected. Our initial assertion upon seeing the images in the previous section, with the long and wide cloud shape, was that the particles stay confined within the boundary layer. To check this assertion, prior to analyzing the cloud growth, let us consider the shock-accelerated flow, specifically its mean velocity and boundary layer width near the walls. Given the well-characterized pre-shock conditions, as well as the confirmed Mach number from pressure traces, the pressure and the velocity of the piston flow following the passage of the shock are easy to determine [23]. Thus, for a Mach number of 1.67, the freestream velocity of the flow is 306 m/s.

Assessing the extent of the wall boundary layer evolving after the passage of the shock is generally a non-trivial problem involving unsteady effects coupled with compressibility and heat transfer effects. Luckily, extensive studies (see Refs. [26, 27] and citations therein) of the boundary layer development behind a moving shock wave have been conducted. As the result of these studies, correlations have been developed for estimating shock-tube boundary layer parameters both for laminar [26] and turbulent [27] cases. The estimates of boundary layer parameters obtained from these studies agree to within a few percent with experimental values. Thus the same correlations were used to estimate the boundary layer thickness in the present work.

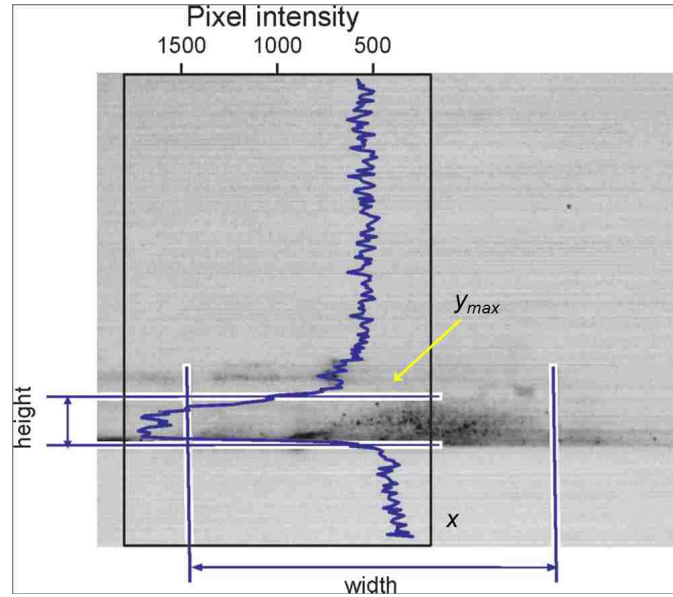


Figure 1.10: Schematic of thresholding procedure to determine the particle-cloud width and height. The vertical line denotes the streamwise (x) location where the cloud upper edge coordinate is sought. The blue line shows the variation of pixel intensity in the corresponding pixel column, the edge y_{max} of the cloud at the given x is where the intensity decreases to half between its maximum and minimum in the direction away from the surface. The highest value of y_{max} within the horizontal extent of the cloud gives the cloud height. The cloud image is inverted, with the darker area corresponding to the cloud.

For a given time t after the shock, the distance x between the “edge” of the boundary layer and the location of interest in the flow would be the distance from that location to the shock front (where the boundary layer thickness is zero). For example, consider $t = 300 \mu\text{s}$ (the timing close to that of the dynamic images in Fig. 1.9). At that time, the shock is at a distance of 0.17 m from the surface sample. At the same time, the middle of the particle cloud lifted off the rough surface (Fig. 1.9, bottom left) is 0.07 m downstream from the surface sample, and $x = 0.17 - 0.07 = 0.1$ m. Given the known conditions in the shocked flow (air at 0.31 MPa and 421 K), the kinematic viscosity is $\nu = 9.26 \times 10^{-6} \text{ m}^2/\text{s}$. The correlations of Mirels [26, 27] produce the estimates for the boundary layer thickness

as 0.18 mm and 1.47 mm for the laminar and turbulent cases, respectively, for the present experimental conditions. Consider $Re_x = Ux/\nu$, the Reynolds number (Re) based on the piston velocity U and the distance from the edge of the boundary layer x . For the chosen time and location, $Re_x \sim 3.3 \times 10^6$, which indicates that the boundary layer should transition to turbulence. However, it is not clear whether sufficient time will have elapsed for this transition to develop, so the laminar estimate (0.18 mm) and the turbulent estimate (1.47 mm) can be treated as upper and lower bounds on the boundary layer thickness.

The boundary layer thickness can also be estimated with momentum integral [28] method, which would only rely on our knowledge of the boundary conditions on the surface (no-slip) and on the edge of the boundary layer (piston velocity), and post-shock pressure. Then we assume that the *average* velocity profile inside the boundary layer can be approximated by a second-order polynomial, and solve for the coefficients of the polynomial using the momentum integral and the boundary conditions (no-slip at the boundary, smooth transition to freestream velocity at the edge). Thus one can arrive at an approximate solution for the average boundary layer thickness δ [29]

$$\frac{\delta}{x} = \frac{\sqrt{30}}{\sqrt{Re_x}} \approx \frac{5.48}{\sqrt{Re_x}} \quad (1.1)$$

This method disregards compressibility and heat transfer effects (although it is “blind” to whether the flow is laminar or turbulent, if the average profile is considered), and it leads to an estimate of $\delta \sim 0.30$ mm, roughly consistent with the laminar result of Mirels [26]. An explicitly laminar, incompressible result not taking heat transfer into account can also be produced by considering the similarity solution of Stokes’ first problem [30] for an impulsively started boundary layer:

$$\delta = 3\sqrt{\nu t} \quad (1.2)$$

where t is the time after impulsive acceleration. In our case for the timing of the

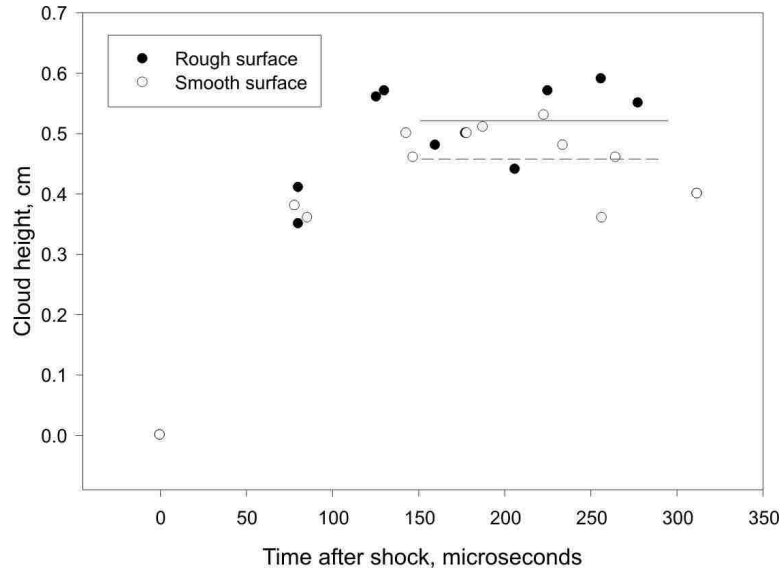


Figure 1.11: Evolution of the particle cloud widths. Solid and dashed horizontal lines refer to average heights after $150 \mu\text{s}$ for the cases of rough and smooth surfaces respectively.

images in Fig. 1.9, $t = 300 \mu\text{s}$ and $\delta \sim 0.16 \text{ mm}$, again, consistent with the laminar estimate, despite the very crude assumptions involved.

At the same time, the observed maximum height of the cloud (distance from surface to edge) is $5.2 \pm 0.6 \text{ mm}$ for the case of the rough surface at this timing, and $4.5 \pm 0.6 \text{ cm}$ for the case of the smooth surface (figures after \pm describing the standard deviation). Figure 1.11 shows the growth trends for the clouds, and for both cases, the cloud height (spanwise) growth is significantly slowed after about $150 \mu\text{s}$. In both cases, the observed height of the cloud exceeds the boundary layer thickness estimated with either laminar formulas [26, 30], the integral method [29], or the turbulent correlation [27].

It is also notable that the cloud heights lifted off the rough and the smooth surfaces are different, and, based on the data shown in Fig. 1.11, the averages of cloud heights for times after $150 \mu\text{s}$ are statistically distinct (t -test [31]) for the

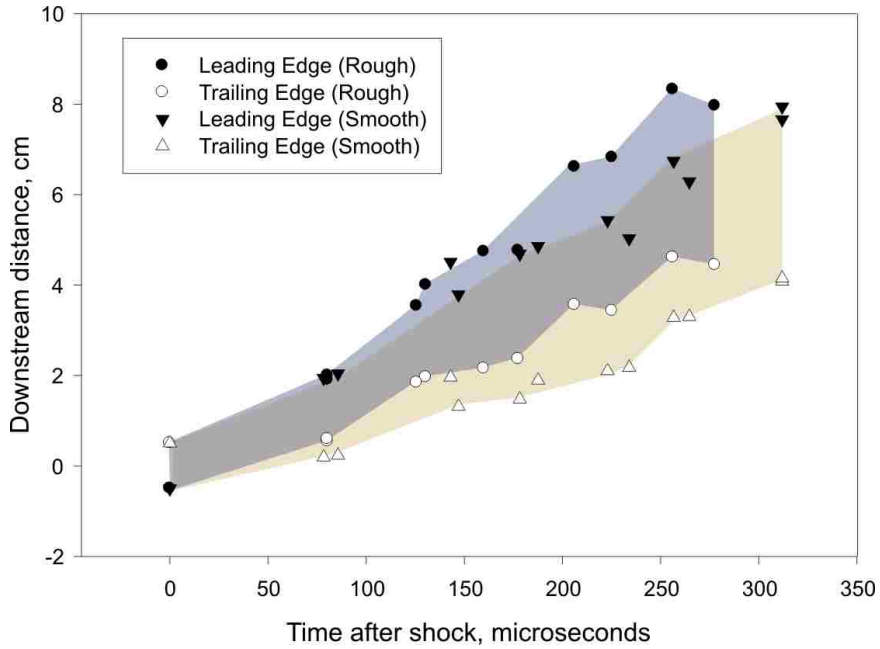


Figure 1.12: Downstream positions of leading and trailing edges of respirable particle clouds vs. time after shock acceleration. Cases of smooth and rough surfaces are considered. Tinted areas serve as guides for the streamwise extent of the particle clouds.

rough and the smooth surface at a 95% confidence level. Note that the late-time data analyzed here were acquired one set of measurements (time, cloud leading edge, trailing edge, height) per experiment, thus the entries comprising the datasets for height measurements are statistically independent.

The differences become even more prominent when we consider the evolution of the width (streamwise extent) of the cloud. Figure 1.12 shows a comparison of experimental data recording the downstream position of the leading and trailing edges of the particle cloud.

While after 150 microseconds the growth of the cloud height significantly slows down, the widths continue to grow in a nearly linear fashion. The cloud of particles advected off the rough surface grows appreciably faster than that for the smooth-

surface case. Propagation velocity estimates based on the leading edge positions after 150 μs are about 298 m/s for the rough surface and 210 m/s for the smooth surface.

Results of the experimental observations that are summarized in Table 1.1 show that there is a considerable difference between both the cloud height and the propagation speed of the leading edge of the cloud for the rough- and smooth-surface samples. What is the physical mechanism responsible for that difference? The only thing that differs in the two series of experiments is the material of the sample patch, and with it – the adhesion force between the particles and the surface. This force was carefully measured using atomic force microscopy, and the results are presented in the last column of Table 1.1. The adhesion force is appreciably stronger between the respirable particles and the smooth surface, and this is what likely accounts for the slower growth of the cloud in this case.

Could the difference in the surface roughness of the sample play a role in the development of the boundary layer and thus affect the cloud height? In addition to obtaining the turbulent boundary layer estimate using the correlations of Mirels [27], the estimate of the viscous sublayer thickness at the same observation location was obtained as $\sim 3.6 \mu\text{m}$ using the same study. In the present work the maximum roughness height of the surfaces is $\sim 2 \mu\text{m}$, suggesting that the test surfaces are hydrodynamically smooth for the purposes of the boundary layer development. Moreover, the streamwise extent of the sample is only 1 cm, thus making roughness differences even less likely to affect the boundary layer growth.

It is also noteworthy that for both surface types we considered, the material of the particle cloud does not reach the freestream velocity during the time interval we investigated (about 300 μs), and shear between the cloud and the main flow moving with the freestream (piston) velocity leads to formation of vortices at the edge of

Table 1.1: Summary of experimental observations of respirable particle propagation. Cloud height and cloud propagation speed estimates are based on data at times after $150 \mu\text{s}$.

Surface type	Cloud height (mm)	Cloud leading edge velocity (m/s)	Adhesion force (nN)
Rough	5.2 ± 0.6	298 ± 8	8 ± 4
Smooth	4.5 ± 0.6	210 ± 7	47 ± 9

the cloud (Fig. 1.9, top right). From this behavior, one could infer that the particles and the air in the cloud exhibit a behavior similar to that recently described for a multiphase-flow analogues of Richtmyer-Meshkov [19] and Rayleigh-Taylor [32] instabilities, wherein a gas carrying embedded particles or droplets exhibits a behavior similar to that of a single-phase gas, but with added density. In reality, after shock acceleration, particles lifted by the flow initially lag behind the embedding air, but for a sufficient particle seeding density (which still can be below 5% by volume), the exchange of momentum between particles and air leads to the air-particle mix moving at a uniform velocity, lower than that of the unseeded freestream flow.

1.5 Conclusions and future work

We presented an experimental study of clouds forming after a shock wave passes a surface sample onto which a monolayer of respirable particles was deposited via sonication. To the best of our knowledge, this is the first such study to have been conducted. The streamwise (parallel to the surface) and spanwise (normal to the surface) extent of the cloud is characterized quantitatively based on analysis of instantaneous flow images acquired at different times after a Mach 1.7 shock arrival.

Chapter 1. Shock-driven particle transport off smooth and rough surfaces

The growth of the clouds appears to be affected by several factors, of which the most influential appears to be the adhesion force between the particles and the surface. Surface samples with stronger initial particle-surface adhesion produce smaller and slower-moving particle clouds. It is also noteworthy that the particle clouds for all the conditions we observed extended well beyond the theoretically estimated boundary layer threshold. These behaviors may suggest that a recently discovered particle lag instability in shock-accelerated multiphase media may play a role in the evolution of the flow.

Future work will address the influence of other parameters of the system, such as particle size and composition, the Mach number, the properties of ambient air (humidity, temperature) and so on. The problem also could benefit from modeling the boundary layers and particle cloud, and from a more thorough examination of the 3D structure of the cloud. Investigations of how the particle(s) detach from the surface could also benefit from additional considerations that would address several questions, such as the differences between a single particle liftoff and that of a layer of particles, or the details of how the adhesion force is overcome by hydrodynamic forces. Conceivably, the latter study could warrant a numerical approach resolving the microscale, *e.g.*, a molecular dynamics (MD) simulation.

References

- [1] D. F. S. Natusch, J. R. Wallace, and C. A. Evans, "Toxic trace elements: preferential concentration in respirable particles," *Science*, vol. 183, pp. 202-204, 1974.
- [2] B. Ferris, Jr., F. Speizer, J. Spengler, D. Dockery, Y. Bishop, M. Wolfson, and C. Humble, "Effects of sulfur oxides and respirable particles on human health: methodology and demography of populations in study," *American Review of Respiratory Disease*, vol. 120, no. 4, pp.767-779, 1979.
- [3] R. Wilson, and J. D. Spengler, *Particles in Our Air: Concentrations and Health Effects*, Harvard School of Public Health, Cambridge, Massachusetts, 1996.
- [4] D. Ganderton, "General factors influencing drug delivery to the lung," *Respirable Medicine*, vol. 91, suppl. 1, pp. 13-16, 1997.
- [5] O. Igra, and K. Takayama, "Shock tube study of the drag coefficient of a sphere in non-stationary flow," *Proceedings of the Royal Society of London. Series A*, vol. 442, pp. 213-247, 1993.
- [6] R. Klemens, P. Zydak, M. Kaluzny, D. Litwin, and P. Wolanski, "Dynamics of dust dispersion from the layer behind the propagating shock wave," *Journal of Loss Prevention in the Process Industries*, vol. 19, pp. 200-209, 2006.
- [7] P. Zydak, and R. Klemens, "Modelling of dust lifting process behind propagating shock wave," *Journal of Loss Prevention in the Process Industries*, vol. 20, pp. 417-426, 2007.
- [8] Y. Gosteev, and A. Fedorov, "Mathematical simulation of lifting and ignition of particles in coal deposits," *Combustion, Explosion, and Shock Waves*, vol. 39, pp.177-184, 2003.

References

- [9] A. Fedorov, and I. Fedorchenko, "Computation of dust lifting behind a shock wave sliding along the layer. Verification of the model," *Combustion, Explosion, and Shock Waves*, vol. 41, pp. 336-345, 2005.
- [10] P. Kosinski, A. Hoffmann, and R. Klemens, "Dust lifting behind shock waves: comparison of two modelling techniques," *Chemical Engineering Science*, vol. 60, pp. 5219-5230, 2005.
- [11] P. Kosinski, and A. Hoffmann, "An eulerian-lagrangian model for dense particle clouds," *Computers & Fluids*, vol. 36, pp. 714-723, 2007.
- [12] C. Ilea, P. Kosinski, and A. Hoffmann, "Simulation of a dust lifting process with rough walls," *Chemical Engineering Science*, vol. 63, pp. 3864-3876, 2008.
- [13] A. Borisov, A. Lyubimov, S. Kogarko, and V. Kozenko, "Instability of the surface of a granular medium behind sliding shock and detonation waves," *Combustion, Explosion, and Shock Waves*, vol. 3, pp. 95-97, 1967.
- [14] V. Boiko, V. Kiselev, S. Kiselev, A. Papyrin, S. Poplavsky, and V. Fomin, "Shock wave interaction with a cloud of particles," *Shock Waves*, vol. 7, pp. 275-285, 1997.
- [15] X. Rogue, G. Rodriguez, J. Haas, and R. Samuel, "Experimental and numerical investigation of the shock-induced fluidization of a particles bed," *Shock Waves*, vol. 8, pp. 29-45, 1998.
- [16] V. Boiko, K. Klinkov, and S. Poplavskii, "Collective bow shock ahead of a transverse system of spheres in a supersonic flow behind a moving shock wave," *Fluid Dynamics*, vol. 39, pp. 330-338, 2004.
- [17] T. Suzuki, Y. Sakamura, O. Igra, T. Adachi, S. Kobayashi, A. Kotani, and Y. Funawatashi, "Shock tube study of particles' motion behind a planar shock wave," *Measurement Science and Technology*, vol. 16, pp. 2431-2436, 2005.
- [18] P. Kosinski, "On shock wave propagation in a branched channel with particles," *Shock Waves*, vol. 15, pp. 13-20, 2006.
- [19] P. Vorobieff, M. Anderson, J. Conroy, R. White, C. R. Truman, and S. Kumar, "Vortex formation in a shock-accelerated gas induced by particle seeding," *Physical Review Letters*, vol. 106, no. 18, p. 184503, 2011.
- [20] I. Bedarev, A. Fedorov, and V. Fomin, "Numerical analysis of the flow around a system of bodies behind the shock wave," *Combustion, Explosion, and Shock Waves*, vol. 48, pp. 446-454, 2012.

References

- [21] J. Wagner, S. Baresh, S. Kearney, W. Trott, J. Castaneda, B. Pruett, and M. Baer, "A multiphase shock tube for shock wave interactions with dense particle fields," *Experiments in Fluids*, vol. 52, pp. 1507-1517, 2012.
- [22] E. Johnson, *Planar and oblique shock wave interaction with a droplet seeded gas cylinder*, M. S. Thesis, University of New Mexico, 2009.
- [23] I. Currie, *Fundamental Mechanics of Fluids*, 3rd. ed., Marcel Dekker, Inc., New York, New York, chap. 12, 2002.
- [24] A. Hinkey, "Pharmaceutical inhalation aerosol powder dispersion: an unbalancing act," *American Pharmaceutical Review*, vol. 6, no. 4, pp. 106-110, 2003.
- [25] M. Kappl, and H.-J. Butt, "The colloidal probe technique and its application to adhesion force measurements," *Particle & Particle Systems Characterization*, vol. 19, pp. 129-143, 2002.
- [26] H. Mirels, "Correlation formulas for laminar shock tube boundary layer," *Physics of Fluids*, vol. 9, pp. 1265-1272, 1969.
- [27] H. Mirels, "Turbulent boundary layer behind constant velocity shock inducing wall blowing effects," *AIAA Journal*, vol. 22, pp. 1042-1047, 1984.
- [28] K. Pohlhausen, "Zur Naherungsweise Integration der Differentialgleichung der Laminaren Grenzschicht," *Zeitschrift fur Angewandte Mathematik und Mechanik*, vol. 1, pp. 252-268, 1921.
- [29] H. Schlichting, and K. Gersten, *Boundary Layer Theory*, McGraw-Hill, New York, New York, chap. 7-8, 2000.
- [30] I. Currie, *Fundamental Mechanics of Fluids*, 3rd ed., Marcel Dekker, Inc., New York, New York, chap. 7, 2002.
- [31] B. Welch, "The generalization of 'Student's' problem when several different population variances are involved," *Biometrika*, vol. 34, pp. 28-35, 1947.
- [32] P. Vorobieff, M. Anderson, J. Conroy, R. White, C. R. Truman, and S. Kumar, "Analogues of Rayleigh-Taylor and Richtmyer-Meshkov instabilities in flows with nonuniform particle and droplet seeding," *Computational Methods in Multiphase Flow VI*, vol. 70, pp. 17-28, 2011.

Part II

Shock Interaction with Single-Phase Initial Conditions

Chapter 2

Oblique shock interaction with a cylindrical density interface³

A cylindrical, initially diffuse density interface is formed by injecting a laminar jet of heavy gas into the test section of a shock tube. The injected gas is mixed with a fluorescent gaseous tracer, small liquid droplets, or smoke particles. The shock tube is tilted with respect to the horizontal. Thus the axis of the gravity-stabilized heavy gas jet is at an oblique angle with the plane of the arriving shock front. The flow structure forming after the oblique shock wave interaction with the column of heavy gas is revealed by visualization in multiple planes. We observe the formation of the well-known counter-rotating vortex columns (same as caused by normal shock waves). However, along with them, periodic co-rotating vortices form in the vertical plane in the flow downstream of the oblique shock. The size of these vortices varies both with the Mach number and with the initial angle between the column and the shock front.

³Originally published as: P. Wayne, D. Olmstead, C.R. Truman, P. Vorobieff, and S. Kumar, "Oblique shock interaction with a cylindrical density interface," *WIT Transactions on Engineering Sciences*, WIT Press, vol. 89, pp. 161-169, 2015, DOI 10.2495/MPF150141.

2.1 Introduction

Richtmyer-Meshkov instability (RMI) occurs when an interface between two fluids of different densities is impulsively accelerated. This acceleration can be the result of an impulsive body force, or a passing shock wave [1]. RMI develops on the interface between a light fluid and a heavy fluid, regardless of the respective direction of the density gradient and the acceleration. This instability is physically relevant for many natural and engineering phenomena, including evolution of supernova remnants, deflagration to detonation transition, inertial confinement fusion (ICF). RMI also plays an important role in mixing during combustion (for a summary, refer to Refs. [2, 3] and citations therein). RMI usually develops in combination with several other hydrodynamic instabilities, one of which is the well-known Kelvin-Helmholtz instability (KHI). KHI occurs when there is a significant velocity difference on the interface between two fluids. Shear created at the interface by this velocity difference induces vorticity which eventually leads to the formation of “cat’s eye” vortices [4]. KHI is present in the cloud bands of giant planets and has been observed in targets accelerated by laser ablation [5].

The recent experiments conducted at the shock tube facility at the University of New Mexico have been focused on oblique shock interactions with a column of heavy gas (sulfur hexafluoride SF_6) surrounded by air. The oblique shock-accelerated gas columns reveal the expected evolution of Richtmyer-Meshkov instabilities, with many features similar to earlier studies with quasi-two-dimensional initial conditions. The oblique case also possesses small-scale three-dimensional (3D) features, physically and morphologically identical to Kelvin-Helmholtz vortices, that develop on the edges of the column. These instabilities present themselves as periodic waves that grow with time and evolve into vortices that cascade down the entire length of the gas column. This paper focuses on these small-scale Kelvin-Helmholtz instabilities,

including a description of the experimental setup, data for 20° and 30° oblique shock angles, and a detailed description of the periodic behavior, including Mach number dependence.

2.2 Experimental Arrangement and Diagnostics

The University of New Mexico Shock Tube Facility is primarily dedicated to the study of RMI. It has been used in several studies of shock wave interactions with a multiphase or heavy gas column [6, 7]. The shock tube itself can operate in a horizontal position or can be inclined to any angle θ , up to 45° above horizontal. Fig. 2.1 shows the shock tube inclined to 30°. Under normal operation, the driver section is pressurized with helium to a predetermined pressure (depending on the desired Mach number). A thin polyester diaphragm separating the driver and driven sections is then punctured, sending a planar normal shock down the length of the tube. Two pressure transducers, located approximately 2.6 m apart on the top of the driven section, record the pressure pulse from the shock wave as it passes. This information is displayed, stored, and is used to trigger the diagnostics and verify the velocity of the shock. The inclined angle of the shock tube, coupled with the planar normal shock impacting the initial conditions (oriented vertically and stabilized by gravity), results in an oblique interaction between the shock and the density interface.

In the experiments described here, initial conditions (ICs) in the test section of the shock tube are formed by vertical injection of sulfur-hexafluoride (SF_6) infused with about 1% acetone gas. The governing parameters of each experiment are the Mach number and the Atwood number. The Mach number here is $M = U/a$, where U is the shock front speed as it propagates through the driven section and a is the speed of sound in air. The Atwood number is $A = (\rho_2 - \rho_1)/(\rho_2 + \rho_1)$, where ρ_2 and ρ_1 are the densities of the heavy and light gas, respectively. For SF_6 and air,

$A = 0.67$.

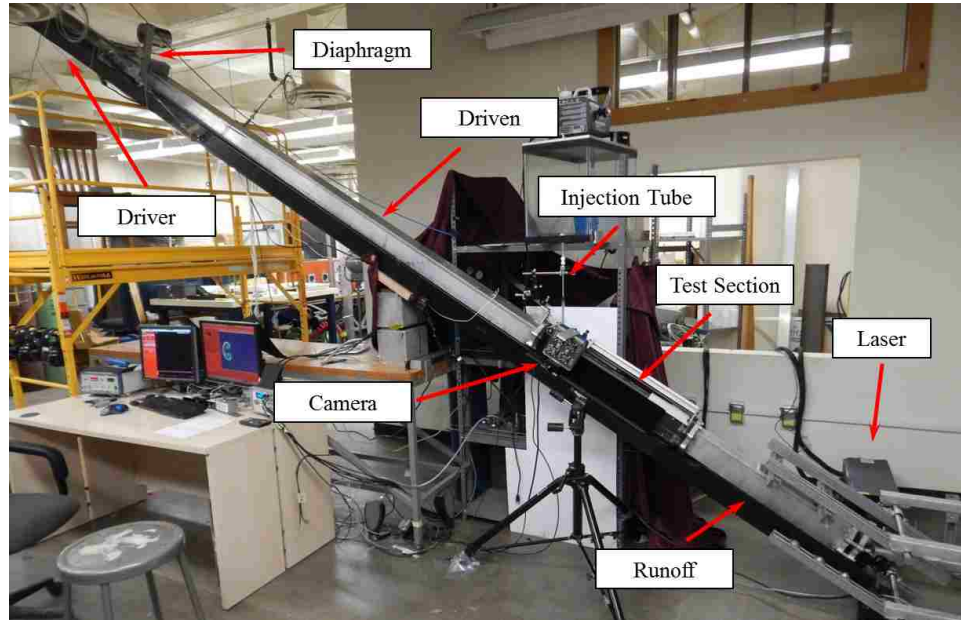


Figure 2.1: Shock tube inclined to 30° . The driver and driven sections are separated by a polyester diaphragm. Pressure transducers are located on top of the driven section. Flow direction is from left to right.

The shock-accelerated column of heavy gas is illuminated by a New Wave Research Gemini 200 UV laser. Planar Laser-Induced Fluorescence (PLIF) images of the column are collected using a four-megapixel Apogee Alta U-42 astronomy camera, with a nominal quantum efficiency of 90%.

The Mach number for each experiment varies by no more than 0.5% from the nominal value, and up to 20 images per Mach number and θ have been used to produce the results presented in the next section, as each experimental run produced one dynamic image at a prescribed timing after shock acceleration.

2.3 Results and Discussion

Misalignment of the pressure p and density ρ gradients in the column of heavy gas accelerated by an oblique shock results in three-dimensional vorticity deposition (Fig. 2.2). The baroclinic vorticity deposited by the shock interaction is proportional to the cross-product $\nabla\rho \times \nabla p$. While in the plane of the cross-section of the column (Fig. 2.2a, top right), this leads to formation of a counter-rotating vortex pair, in the vertical plane (Fig. 2.2a, bottom right), vortex sheets form on the upstream and downstream sides of the column.

As the result, shear layers form on the density interfaces in the vertical plane (Fig. 2.2b), leading to velocity differences between the lighter air and the heavier column material, and to formation of KHI. For example, the air is traveling down the upstream side of the column, resulting in small-amplitude perturbations evolving into vortices. The kinetic energy of the air moving down the edge of the column fuels the vortex growth via shear.

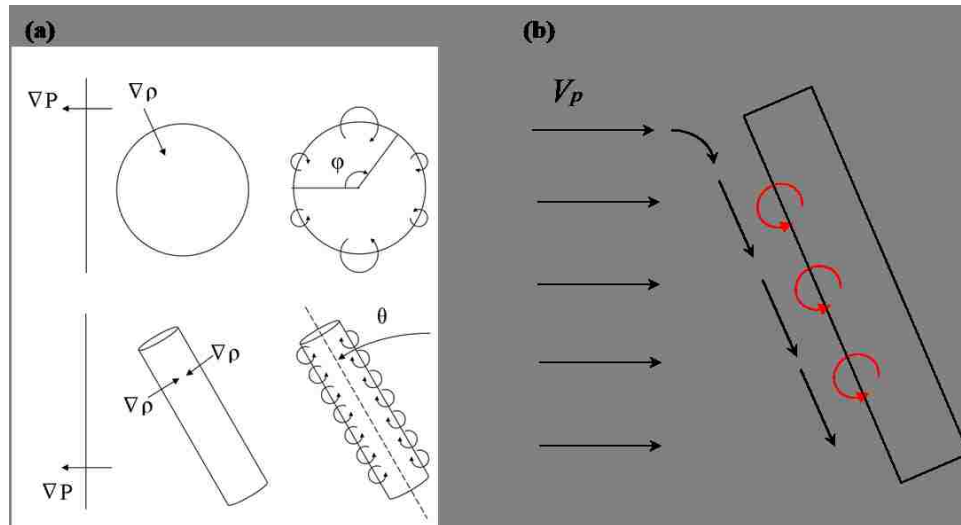


Figure 2.2: Sketch of three-dimensional vorticity deposition showing (a) pressure and density gradients [8] and (b) air moving down the upstream edge of the column.

Chapter 2. Oblique shock interaction with a cylindrical density interface

High repeatability of the initial conditions allows the reconstruction of time history of the flow based on the experimental images acquired at different times after shock arrival for each prescribed M and θ . The quantitative parameter of interest here is the wavelength λ of KHI. Wavelengths are measured as the linear distance between the centers of consecutive vortices using ImageJ software [9]. The measurement area is $1.0 \text{ cm} \times 1.5 \text{ cm}$ (Fig. 2.3) both for the $\theta = 20^\circ$ and $\theta = 30^\circ$ cases, allowing to use a sequence of five consecutive vortices to produce a total of four measurements per image. Measurements were then averaged for each image and sorted according to θ and M . Temporal evolution of the flow was presented in terms of non-dimensional time parameter τ , derived from the linear growth theory of RMI [10]:

$$\tau = kA\Delta V(t - t_0) \quad (2.1)$$

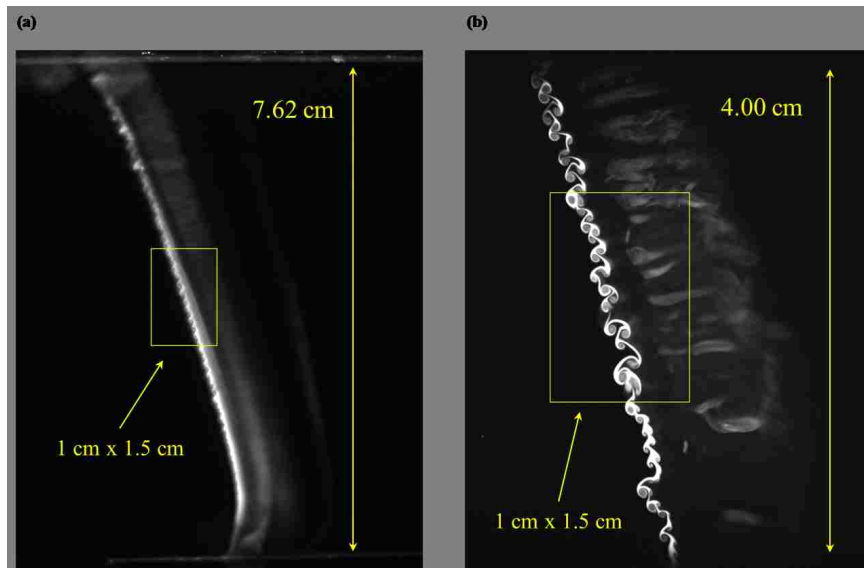


Figure 2.3: Areas of interest where measurements of KHI were taken for (a) 30° and (b) 20° inclination angles. The full cross-sectional extent of the test section of the shock tube is 7.62 cm, images at 20° were taken at a higher resolution, but the area of interest has the same physical dimensions.

Chapter 2. Oblique shock interaction with a cylindrical density interface

Here $k = 2\pi/d$ is the perturbation wavenumber, where d is the diameter of the initial conditions (and the dominant length scale), ΔV is the Mach number-dependent piston velocity, and the expression $(t - t_0)$ is the time after shock arrival at the center of the heavy gas column.

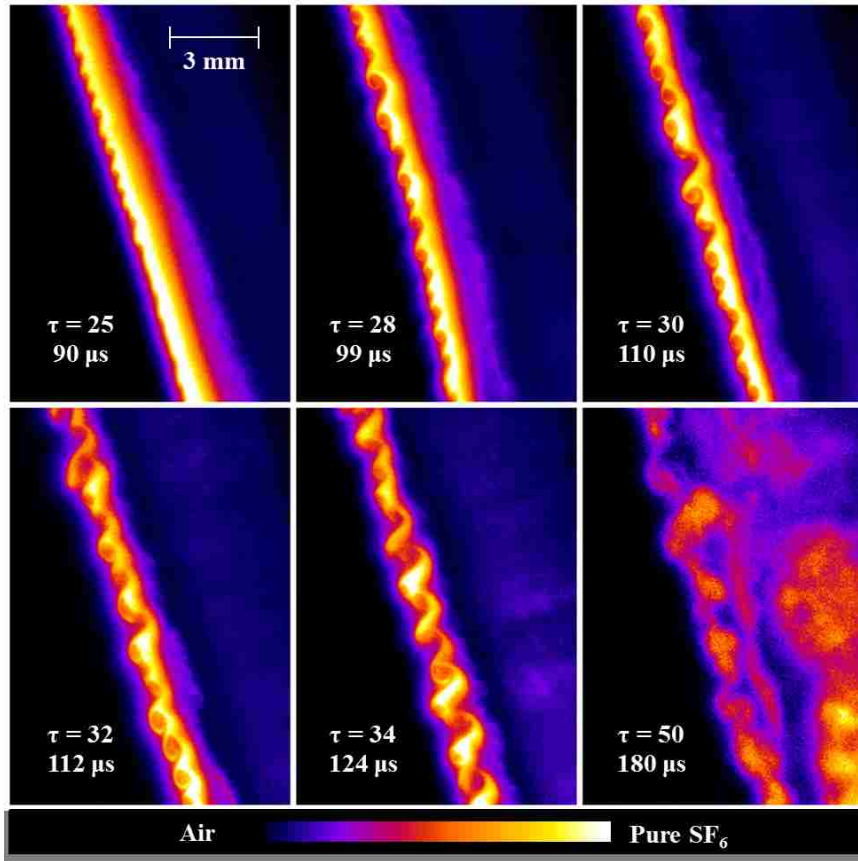


Figure 2.4: Temporal evolution of KHI for $M = 2.00$, $\theta = 30^\circ$. Each image is labeled with actual time after shock acceleration and dimensionless time τ (Eq. 2.1).

Figure 2.4 shows a sequence of six vertical plane images captured at a 30° inclination angle at Mach number $M = 2.00$. KHI first presents itself as small perturbations at the top of the column and moves vertically down the upstream edge ($t = 90 \mu\text{s}$ after shock impact). The instabilities quickly evolve into “cat’s eye” vortices, indicative of KHI ($t = 99, 100 \mu\text{s}$). At later times, same-sign vortices begin to merge

($t = 112 \mu s$). The resulting larger-scale vortices start to mix ($t = 124 \mu s$), resulting in apparent transition to turbulence ($t = 180 \mu s$).

Figure 2.5 shows a comparison of KHI vortices observed at several Mach numbers at a 30° inclination angle. As the Mach number increases, the respective wavelength decreases. This behavior is expected since the dominant length scale amplified by the KHI is the size of the cross-section of the shock-compressed SF_6 column. At higher Mach numbers, there is greater compression and accordingly the dominant post-shock length scale is reduced [8].

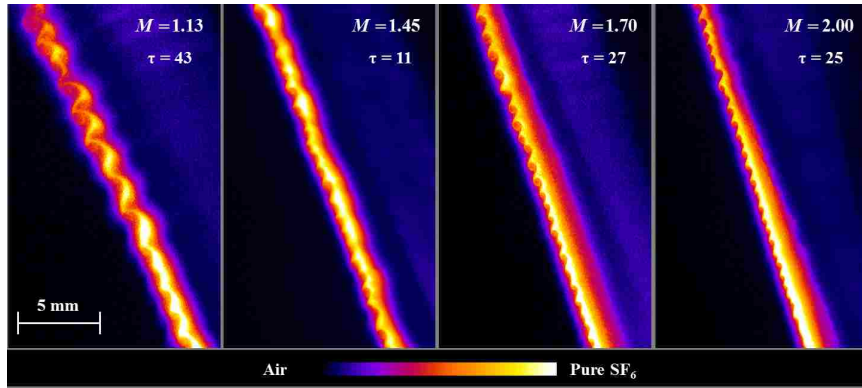


Figure 2.5: Comparison of KHI vortices at different Mach numbers (as labeled) for 30° inclined shock tube. Mach number increases from left to right.

Similar trends can be observed in KHI images acquired at a 20° inclination angle, with one notable difference. For a Mach = 1.13 shock wave, the waves that formed on each sides of the high-density region (Fig. 2.6) quickly evolved to produce staggered counter-rotating vortex pairs. This behavior precipitated mixing and turbulent transition for this case. Images at later times reveal turbulent transition occurring well before that at 30° inclination for the same Mach number.

Measurements of wavelength λ are presented in Fig. 2.7. Here wavelength is normalized by the nominal (pre-shock) diameter of the initial conditions. Horizontal error bars correspond to standard deviation of Mach number while the vertical error

bars are the standard deviation of λ . Power-law fits are superimposed with each data set (Fig. 2.7, $\theta = 30^\circ$, and Fig. 2.7, $\theta = 20^\circ$) to serve as visual aids.

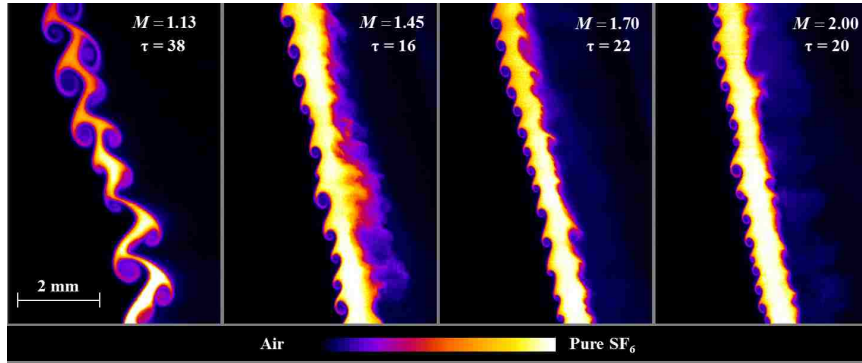


Figure 2.6: Comparison of KHI vortices at different Mach numbers (as labeled) for 30° inclined shock tube. At $M = 1.13$, vortices form on *both* sides of the high density region.

For inclination angle $\theta = 30^\circ$, wavelengths ranged from 1.60 mm for Mach 1.13 to 0.97 mm for Mach 2.00. The average standard deviation of λ for 30° and 20° inclination angles is $101.2 \mu\text{m}$ and $43.58 \mu\text{m}$ respectively. Measurements taken at 20° show that the wavelengths are significantly smaller than those at 30° inclination, varying by as much as 49%. For Mach = 1.13, $\lambda = 1.10 \text{ mm}$, and for Mach = 2.00, $\lambda = 0.49 \text{ mm}$.

While existing theory [8] explains the Mach number dependence for each θ , explanation of the smaller scale of vortices for $\theta = 20^\circ$ will require additional consideration. In the limiting case of a planar normal shock ($\theta = 0$), there would be no macroscopic baroclinic vorticity deposition in the vertical plane, and thus no shear layers. It is possible that the length scale amplified by the KHI is not the compressed size of the gas column d_c , but rather this length scale projected on the direction along the column where KHI evolves, $d_c \tan \theta_c$, where θ_c is the tilt angle of the shock-accelerated column.

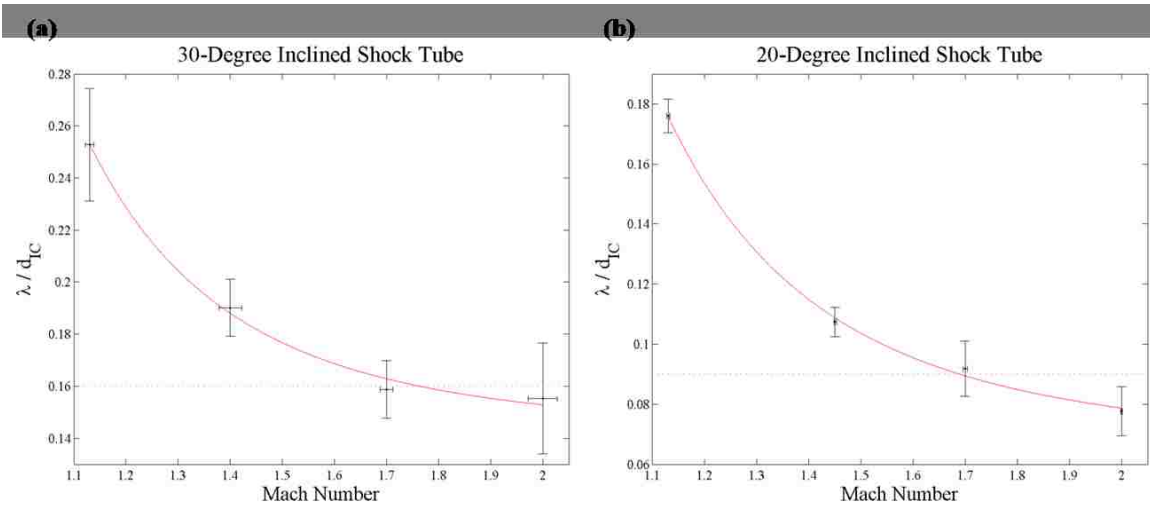


Figure 2.7: KHI wavelength λ vs. Mach number M for (a) 30° and (b) 20° inclination. The data suggest that λ decreases as inclination angle $\theta \rightarrow 0$. Power-law fits are used as a visual aid.

2.4 Conclusions

We have conducted an experimental study of the formation of Kelvin-Helmholtz secondary instability in the flow produced by oblique planar shock interaction with an initially cylindrical density interface. While some of the results are well explained by existing theory, additional studies will be conducted to clarify the nature of the observed relationship between the dominant KHI wavelength and the tilt angle of the gas column with respect to the shock front.

References

- [1] C. E. Niederhaus, *Experiments on the Richtmyer-Meshkov instability of compressible fluids*, Ph.D. Thesis, University of Arizona, 2000.
- [2] M. Brouillette, "The Richtmyer-Meshkov Instability," *Annual Review of Fluid Mechanics*, vol. 34, pp. 445-468, 2002.
- [3] S. Kumar and P. Vorobieff, "Experimental studies of the Richtmyer-Meshkov instability," *Recent Research Developments in Fluid Dynamics*, vol. 5, pp.33-55, 2004.
- [4] D. Ryu, T. W. Jones, and A. Frank, "The magnetohydrodynamic Kelvin-Helmholtz instability: a three-dimensional study of nonlinear evolution," *The Astrophysical Journal*, vol. 545, no. 1, pp. 475-493, 2000.
- [5] M. Emery, J. Gardner, and J. Boris, "Rayleigh- Taylor and Kelvin-Helmholtz instabilities in targets accelerated by laser ablation," *Phys. Rev. Letters*, vol. 48, pp. 677-680, 1982.
- [6] T. Bernard, C. R. Truman, P. Vorobieff, C. Corbin, P. Wayne, G. Kuehner, M. Anderson, and S. Kumar, "Observation of the development of secondary features in a Richtmyer-Meshkov instability driven flow," *Journal of Fluids Engineering*, vol. 137, no. 1, 011206, 2015.
- [7] P. Vorobieff, M. Anderson, J. Conroy, R. White, C. R. Truman, and S. Kumar, "Analogues of Rayleigh-Taylor and Richtmyer-Meshkov instabilities in flows with nonuniform particle and droplet seeding," *Computational Methods in Multiphase Flow VI*, vol. 70, pp. 17-28, 2011.
- [8] D. Olmstead, P. Wayne, J. H. Yoo, S. Kumar, C. R. Truman, and P. Vorobieff, "Experimental study of shock accelerated inclined heavy gas cylinder," *Experiments in Fluids*, vol. 58, p. 71, 2017.

References

- [9] T. Fereira and W. Rasband, ImageJ User Guide, <http://imagej.nih.gov/ij/docs/guide/user-guide.pdf>, 2012.
- [10] R. Richtmyer, "Taylor instability in shock acceleration of compressible fluids," Tech. Rep. LA-1914, Scientific Laboratory of the University of California, Los Alamos, New Mexico, July 1954.

Chapter 3

Oblique shock interaction with a laminar cylindrical jet⁴

We present an experimental study of planar shock interaction with an initially cylindrical, diffuse density interface, where the angle α between the plane of the shock and the axis of the cylinder can be zero (planar normal interaction) or non-zero (oblique interaction). The interface is formed by injecting a laminar jet of a heavy gas mixture (sulfur hexafluoride, acetone, nitrogen) into quiescent air. The jet is stabilized by an annular co-flow of air to minimize diffusion. Interaction between the pressure gradient (shock front) and density gradient leads to vorticity deposition, and during the subsequent evolution, the flow undergoes mixing (injected material - air) and eventually transitions to turbulence. Several parameters affect this evolution, including the angle α , the Atwood number (density ratio), and the Mach number of the shock. For quantitative and qualitative characterization of the influence of these

⁴Originally published as: P. Wayne, D. Olmstead, C.R. Truman, P. Vorobieff, and S. Kumar, "Oblique shock interaction with a laminar cylindrical jet," *AIP Conference Proceedings: Shock Compression of Condensed Matter*, American Institute of Physics, Vol. 1793, No. 1, p. 150004, 2017.

parameters, we use flow visualization in two planes that relies on planar laser-induced fluorescence (PLIF) in acetone, which forms part of the injected material.

3.1 Introduction

Richtmyer-Meshkov instability (RMI) develops when an interface between two fluids of different densities is impulsively accelerated. This impulsive acceleration can be the result of an impulsive body force, or of the passage of a shock wave [1]. This instability develops on the interface between a light fluid and a heavy fluid, regardless of the respective density gradient and the acceleration [2]. In our experiments, a misalignment of the pressure (shock) and density (gas column) gradients results in three-dimensional vorticity deposition on the gas-gas interface. RMI has been observed in many natural phenomena and engineering problems, including large-scale astrophysical structures, fuel-air mixing and combustion in scramjets [3], and experiments in inertial confinement fusion (ICF). While RMI is the dominant feature in many shock tube experiments with a laminar cylindrical jet, other instabilities can be driven by RMI, including Kelvin-Helmholtz instability (KHI). KHI occurs when there is significant velocity difference along the interface between two fluids [2]. Shear created by the velocity difference, induces vorticity on the interface that eventually leads to formation of large co-rotating waves, called billows [4]. KHI have been also observed in cloud bands of giant planets, and targets accelerated by laser ablation [5].

Recent experiments conducted in the shock tube facility at the University of New Mexico (UNM) focus mainly on oblique shock interaction with a heavy gas column, specifically sulfur hexafluoride (SF_6) infused with acetone gas. Planar laser-induced fluorescence (PLIF) images of the shock-accelerated column reveal the expected evolution of Richtmyer-Meshkov instabilities, but also small-scale, three-dimensional fea-

Chapter 3. Oblique shock interaction with a laminar cylindrical jet

tures, characteristic of Kelvin-Helmholtz waves (billows). These instabilities present themselves as periodic waves that grow with time and evolve into vortices that roll down the entire [vertical] length of the gas column [2]. Experiments and data analysis described here focus on how RMI and KHI affect the shock-accelerated column.

The shock tube at UNM is approximately 5.8 meters long and can be operated in a horizontal position, or can be inclined to any angle α from 0° to 45° above horizontal. Figure 3.1(a) is a simple schematic showing the different sections of the shock tube, the angle of inclination α , and the direction of flow. Under normal operation, the driver section is pressurized to a predetermined pressure, which depends on the desired Mach number. A thin-film polyester diaphragm separating the driver and driven sections is then punctured, sending a normal shock down the length of the tube. Two high-frequency response pressure transducers, located on the top of the driven section, record the pressure pulse of the shock wave as it passes. This information is used to verify the velocity of the shock and trigger other experimental diagnostics.

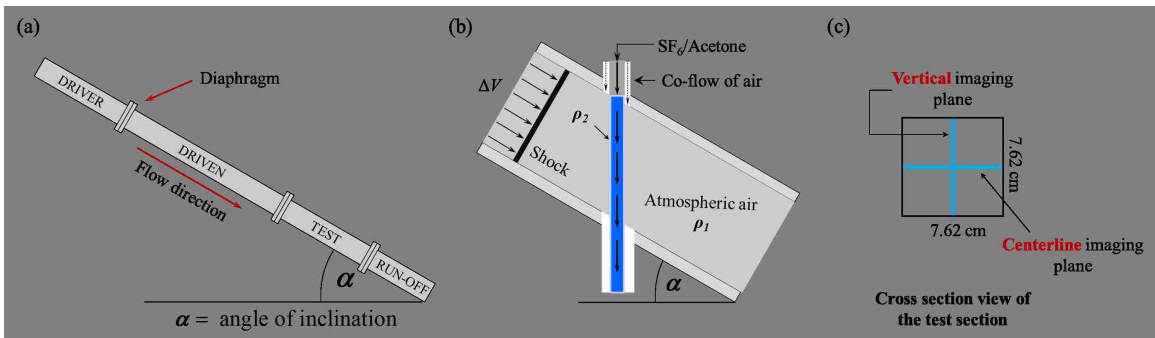


Figure 3.1: (a) Schematic of shock tube at UNM showing the angle of inclination α , and the driver, driven, test, and run-off sections, respectively. (b) Cross-section view of the test section (7.62 cm \times 7.62 cm), showing the vertical and centerline imaging planes. (c) Schematic of the shock tube test section, where ΔV = velocity of air behind the shock (piston velocity), ρ_1 = density of air at room temperature and pressure, and ρ_2 = density of the injected material.

In the experiments described here, the initial conditions (ICs) consist of SF₆, infused with 11% acetone gas by mass. Figure 3.1(b) is an illustration of the injection area of the test section. The ICs are injected vertically down into the test section and stabilized by a co-flow of air. The angle between the axis of the jet and the plane of the shock is also α . PLIF images of the shock-accelerated gas column consist of time-resolved sets of centerline and vertical plane images. Figure 3.1(c) is a cross-section view of the test section, showing the orientation of these two planes.

The governing parameters for these experiments are the Mach number, the Atwood number, and non-dimensional time τ . The Mach number is $M = u/a$, where u = the velocity of the shock front and a = the speed of sound in air at room temperature and pressure. The Atwood number is $A = (\rho_2 - \rho_1) / (\rho_2 + \rho_1)$, where ρ_2 is the density of the heavy gas and ρ_1 is the density of the light gas. Atwood number for pure SF₆ initial conditions (with 11% acetone gas by mass) is 0.61. Non-dimensional time τ here is $\tau = kA\Delta V (t_1 - t_0)$, where the wavenumber $k = 2\pi/6.25$ mm (nominal diameter of ICs = 6.25 mm), ΔV is the piston velocity, and $(t_1 - t_0)$ corresponds to time after shock impact.

3.2 Experimental Results

Three-dimensional vorticity is deposited on the gas column by the oblique shock wave due to a misalignment of the pressure and density gradients. This baroclinic vorticity is proportional to the cross-product $\nabla p \times \nabla \rho$ [6]. In the centerline plane, this results in the formation of a relatively large counter-rotating vortex pair (CRVP), indicative of RMI. However, in the vertical plane, co-rotating vortices form on the upstream and downstream sides of the column (for a more detailed summary, refer to Refs. [2],[7]). These vortices begin as small perturbations on the interface that grow with time and evolve into structures morphologically identical to Kelvin-Helmholtz waves.

Oblique shock experiments were carried out for two inclination angles: $\alpha = 20^\circ$ and $\alpha = 30^\circ$. Four representative Mach numbers were chosen: $M = 1.13$ (lowest possible Mach number with the current setup), $M = 1.45$, $M = 1.70$, $M = 2.00$. All PLIF images presented here were taken using an Apogee Alta U42 CCD high quantum efficiency ($\sim 95\%$) camera. A frequency-quadrupled, double-pulsed Nd:YAG laser operating at 266 nm wavelength (UV) was used as light source. The laser beam was expanded into a light sheet illuminating a planar cross section of the flow. For each data set (Mach number, imaging plane), qualitative and quantitative analysis was conducted.

3.2.1 Qualitative Data

Figure 3.2 illustrates the evolution of the column in both vertical (top row) and centerline (bottom row) planes, from shock impact to turbulent transition. Here, the Mach number is $M = 1.13$, the Atwood number is 0.61, and the inclination angle is 20° . Each image was obtained in a separate experiment and post-shock timings (given in microseconds) were matched for each vertical/centerline pair. Flow direction is from left to right.

In the centerline plane, just after shock impact, a small spike forms due to shock focusing, but quickly collapses back into the high density region, likely due to the flow produced by the CRVP that rapidly develops prominent spiral shaped features extending into the cores of each vortex. The spiral structures continue to wrap into the vortex cores until small-amplitude secondary instabilities form on the outer edges of the CRVP and inside the cores. A relatively short time later, the spiral structures and quasi-symmetric morphology of the column succumb to mixing and transition to turbulence.

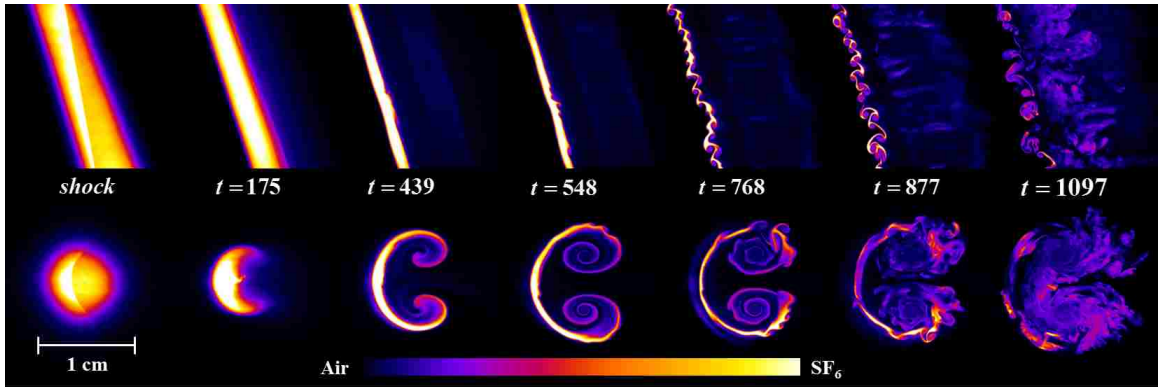


Figure 3.2: Sequence of images showing evolution of the heavy gas column accelerated by an oblique shock. Top: vertical plane, bottom: centerline plane. Here $M = 1.13$, $A = 0.61$, and $\alpha = 20^\circ$. Lighter colors (see color bar) correspond to regions of high SF_6 /acetone concentration, and darker colors correspond to regions of lower density, with pure air colored black.

In the vertical plane, evidence of spike formation can be seen on edge for $t = 175 \mu\text{s}$; the thin line just downstream of the high density region on the bottom half of the image. Later, small perturbations on the upstream and downstream edges of the column begin to develop. These perturbations, amplified by shear on the interface, begin to form billows and waves (indicative of KHI) that quickly grow and combine, before mixing and transitioning to turbulence. These features are more prominent on the interface in the direction from which the shock arrived. Billows on the other side of the column appear smeared, likely due to interaction with the CRVP in the centerline plane (Fig. 3.2). The spacing between the centers of Kelvin-Helmholtz vortex pairs, or wavelength λ (Fig. 3.3), was quantified for each Mach number and angle of inclination.

Analysis of the experimental images revealed KHI wavelengths depended on several factors, the most prevalent being the Mach number of the shock wave and the angle of inclination α . Figure 3.3 suggests that as the Mach number increases, wavelength decreases. Here, $\alpha = 20^\circ$ and $A = 0.61$; similar trends were discovered for the

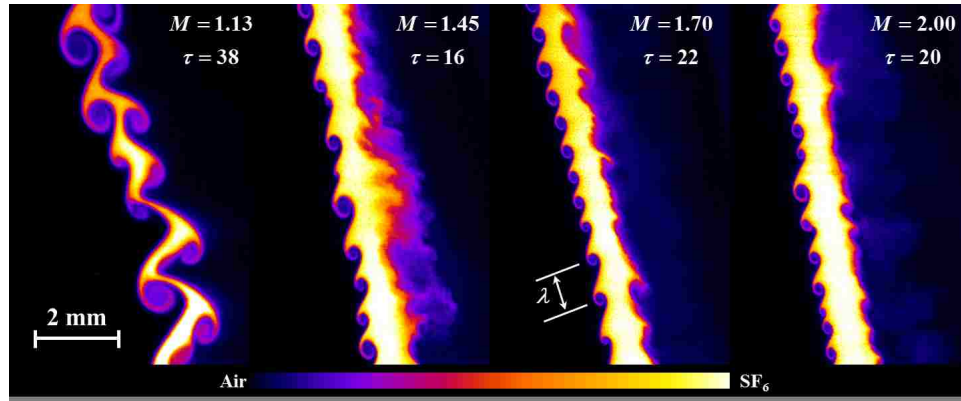


Figure 3.3: Image showing the effect of Mach number on KHI wavelength λ . As the Mach number increases, wavelength decreases. Inclination angle here is 20° and the Atwood number is 0.61. Mach numbers from left to right are $M = 1.13$, $M = 1.45$, $M = 1.70$, and $M = 2.00$.

30° case. Analysis also shows that as the angle of inclination (α) decreases, so does the corresponding wavelength, regardless of Mach number.

3.2.2 Quantitative Analysis

In the centerline plane, the dominant feature was the large CRVP due to RMI. Its growth was quantified in many earlier studies (mostly for planar normal interaction). To match results from previous experiments and to validate numerically predicted values [6], measurements of several features were acquired, including the spanwise extent (or width) and streamwise extent of the CRVP, the full linear extent of the plume, and characteristics of secondary features (for a more thorough explanation of these features, refer to Refs. [6], [7], and [8]). Figure 3.4 shows measured values of the spanwise width (w) of the CRVP as a function of non-dimensional time τ . Filled circles on the graph correspond to data at angle of inclination $\alpha = 20^\circ$, while filled triangles correspond to $\alpha = 30^\circ$. Nondimensionalization for the vertical axis σ is chosen to produce the best collapse for the growth rates at $\tau < 100$, $\sigma =$

$w/(d_{IC}M^{1/2})$. Here d_{IC} is the diameter of the initial conditions. Notice that in these coordinates the respective growth rate for each Mach number and inclination angle α seems to follow the same trend.

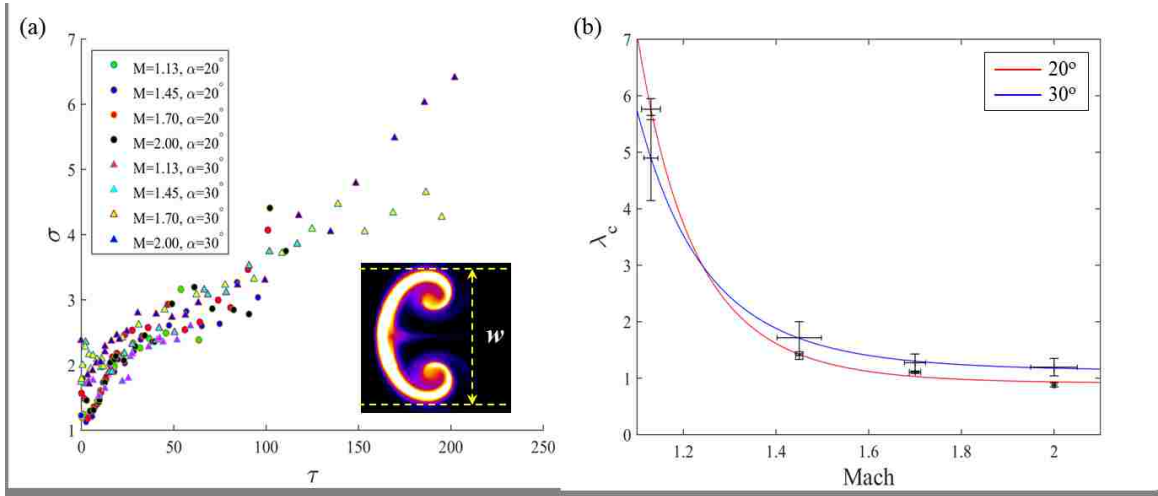


Figure 3.4: (a) Centerline plane: graph of CRVP spanwise width w vs. dimensionless time τ , for each Mach number and inclination angle α . (b) Vertical plane: graph of normalized KHI wavelengths with respect to Mach number for inclination angles $\alpha = 20^\circ$ (red line), and $\alpha = 30^\circ$ (blue line). Here, $\lambda_c = \lambda/(\sqrt{MD_c \tan \phi})$.

In the vertical plane, the most obvious target for analysis is the wavelength λ , or the linear distance between the centers of pairs of Kelvin-Helmholtz vortices. Five consecutive pairs were chosen within a $1.0 \text{ cm} \times 1.5 \text{ cm}$ area of interest within each image. For an inclination angle $\alpha = 30^\circ$, wavelengths varied from 1.60 mm for Mach 1.13, to 0.97 mm for Mach 2.00, decreasing with Mach number. Kelvin-Helmholtz instability amplifies perturbations at all wavelengths, thus the mechanism for selection of λ and its Mach number dependence must be explained.

One scale that is immediately apparent is the compressed diameter (or, more accurately, compressed stream wise extent) of the shock-accelerated column, D_c . The compressed diameter is simply the smallest linear distance from the upstream side of the column to the downstream side. In the images, this can be measured

by finding the exact location where the shock wave exits the gas column. This quantity is of interest to verify theoretical predictions of Ref. [8] and also as a basis for determining the dominant length scale associated with structures (waves) seen in the vertical plane. Figure 3.4b is a graph of non-dimensionalized wavelength λ_c versus Mach number for each inclination angle α . The quantity λ_c is the experimentally measured wavelength λ normalized by the theoretical compressed diameter D_c , the square root of the Mach number, and the tangent of the theoretical turning angle ϕ , which is the angle between the axis of the uncompressed (pre-shock) and compressed (post-shock) gas column. Notice the trend is identical for both inclination angles. Here, the vertical error bars are the standard deviation in λ (normalized by D_c , $M^{1/2}$, and $\tan \phi$) and the horizontal error bars correspond to the standard deviation in Mach number. Collapse of the curves strongly suggests that the chosen scaling is physically relevant.

3.3 Conclusions

Experimental studies of oblique shock interaction with a heavy-gas column show that three-dimensional vorticity deposition introduces significant changes into the flow evolution (compared with the better studied planar normal case). One prominent feature is the roll-up of shear-driven vortices in the vertical plane, whose scaling is dependent on Mach number and tilt angle. A scaling dependent on the square root of the Mach number produces good results in collapsing the data, suggesting that this dependence, originally proposed by [6, 9], has physical relevance. Future work with the same data sets will include structure function analysis [10], mixing interface length measurements [11], and quantification of interfacial fractal properties [12], with focus on transition from deterministic, fully three-dimensional vortex-dominated flow to turbulence.

References

- [1] C. E. Niederhaus, *Experiments on the Richtmyer-Meshkov instability of compressible fluids*, Ph.D. Thesis, University of Arizona, 2000.
- [2] P. Wayne, D. Olmstead, P. Vorobieff, C. R. Truman, and S. Kumar, "Oblique shock interaction with a cylindrical density interface," *Computational Methods in Multiphase Flow VIII*, vol. 89, pp. 161-169, 2015.
- [3] Q. Yang, J. Chang, and W. Bao, "Richtmyer-Meshkov instability inducing mixing enhancement on the scramjet combustor with a central strut," *Advances in Mechanical Engineering*, vol. 6, pp. 1-7, 2014.
- [4] W. Smyth and K. Winters, "Turbulence and mixing in Holmboe waves," *Journal of Physical Oceanography*, vol. 33, pp. 694-711, 2002.
- [5] M. Emery, J. Gardner, and J. Boris, "Rayleigh-Taylor and Kelvin-Helmholtz instabilities in targets accelerated by laser ablation," *Phys. Rev. Letters*, vol. 48, pp. 677-680, 1982.
- [6] M. Anderson, *Oblique shock interactions with perturbed density interfaces*, Ph. D. Thesis, University of New Mexico, 2011.
- [7] D. Olmstead, *Oblique shock wave effects on an impulsively accelerated heavy gas column*, Ph. D. Thesis, University of New Mexico, 2015.
- [8] D. Olmstead, P. Wayne, J. H. Yoo, S. Kumar, C. R. Truman, and P. Vorobieff, "Experimental study of shock accelerated inclined heavy gas cylinder," *Experiments in Fluids*, vol. 58, p. 71, 2017.
- [9] G. Orlicz, *Incident shock Mach number effects on Richtmyer-Meshkov mixing with simultaneous density and velocity measurements*, Ph. D. Thesis, University of New Mexico, 2012.

References

- [10] P. Vorobieff, P. M. Rightley, and R. F. Benjamin, "Power-law spectra of incipient gas-curtain turbulence," *Physical Review Letters*, vol. 81, pp. 2240-2243, 1998.
- [11] S. Kumar, G. Orlicz, C. Tomkins, C. Goodenough, K. Prestridge, P. Vorobieff, and R. Benjamin, "Stretching of material lines in shock-accelerated gaseous flows," *Physics of Fluids*, vol. 17, p. 082107, 2005.
- [12] P. Vorobieff, P. M. Rightley, and R. F. Benjamin, "Shock-driven gas curtain: fractal dimension evolution in transition to turbulence," *Physica D: Nonlinear Phenomena*, vol. 133, no. 1, pp. 469-476, 1999.

Part III

Fundamental Physics of Gas Mixtures with Shock Propagation

Chapter 4

Investigation of Dalton and Amagat's laws for gas mixtures with shock propagation⁵

Dalton's and Amagat's laws (also known as the law of partial pressures and the law of partial volumes respectively) are two well-known thermodynamic models describing gas mixtures. Our current research is focused on determining the suitability of these models in predicting effects of shock propagation through gas mixtures. Experiments are conducted at the Shock Tube Facility at the University of New Mexico (UNM). The gas mixture used in these experiments consists of approximately 50% sulfur hexafluoride (SF₆) and 50% helium (He) by mass. Fast response pressure transducers are used to obtain pressure readings both before and after the shock wave; these data are then used to determine the velocity of the shock wave. Temperature readings

⁵Originally published as: P. Wayne, S. Cooper, D. Simons, I. Trueba-Monje, J. H. Yoo, P. Vorobieff, C. R. Truman, and S. Kumar, "Investigation of Dalton and Amagat's laws for gas mixtures with shock propagation," *Computational Methods and Experimental Measurements*, vol. 6, issue 1, pp. 1-10, 2018, DOI 10.2495/CMEM-V6-N1-1-10.

are obtained using an ultra-fast mercury cadmium telluride (MCT) infrared (IR) detector, with a response time on the order of nanoseconds. Coupled with a stabilized broadband infrared light source (operating at 1500 K), the detector provides pre- and post-shock line-of-sight readings of average temperature within the shock tube, which are used to determine the speed of sound in the gas mixture. Paired with the velocity of the shock wave, this information allows us to determine the Mach number. These experimental results are compared with theoretical predictions of Dalton's and Amagat's laws to determine which one is more suitable.

4.1 Introduction

Dalton's law was observed in 1801 by an English chemist, physicist, and meteorologist John Dalton. In 1802, he reported his findings [1] in *Memoirs of the Literary and Philosophical Society of Manchester*. This law of additive (partial) pressures states that the total pressure of a gas mixture is equal to the sum of the pressures each gas would exert if it existed alone at the mixture temperature and volume.

In 1880, a French physicist Émile Hilaire Amagat published his findings while researching the compressibility of different gases. Amagat's law of additive (partial) volumes is similar to Dalton's law, stating that the total volume of a gas mixture is equal to the sum of the volumes each gas would occupy if it existed alone at the temperature and pressure of the mixture [2]. Although science has evolved considerably since the 1800s, very little is known about the behavior of multicomponent gases in various conditions, especially when these gases experience near-instantaneous increases (or decreases) in properties such as pressure, density, and temperature.

The goal of the experiment described here is to determine the accuracy of Dalton's law and Amagat's law in prediction of the properties of a gas mixture subject to shock

wave propagation. Shock wave effects on gaseous mixtures are important not only for the fundamental understanding of the physics involved, but also for real-world applications such as scramjet/ramjet engine inlets [3], and pneumatic systems and piping [4]. These experimental data can also be used for numerical validation to better predict these effects in computational fluid dynamics (CFD) simulations.

4.2 Theory

Dalton's law and Amagat's law can be expressed by the following equations:

$$\text{Dalton's law: } P_m = \sum_{i=1}^k P_i(T_m, V_m) \quad (4.1)$$

$$\text{Amagat's law: } V_m = \sum_{i=1}^k V_i(T_m, P_m) \quad (4.2)$$

where P_i and V_i correspond to pressure and volume of the individual gas components, P_m and V_m correspond to the pressure and volume of the gas mixture, and T_m is the temperature of the mixture. A system obeying Eqn. (4.1) exactly is known as an ideal mixture, irrespective of whether its components individually behave as ideal gases [5]. The ideal gas equation of state (EOS) is expressed as $PV = nRT$, where n = the amount of the gas (in moles) and $R = 8.314 \text{ J/mol}\cdot\text{K}$ is the universal gas constant. For ideal gas systems, both Eqn. (4.1) and Eqn. (4.2) provide exact results, but only approximate solutions for real gases, due to intermolecular forces, compressibility, and non-equilibrium thermodynamic effects. Real gases can be expressed more precisely by a modified form of the ideal gas EOS,

$$PV = znRT \quad (4.3)$$

$$z = \frac{PV}{nRT} \quad (4.4)$$

where z is the compressibility factor of the gas. Applying Eqn. (4.4) to both Dalton and Amagat's laws gives the compressibility factor of the gas mixture as

$$\text{Dalton: } z_m(P, T) = \sum_i x_i z_i(P_i, T_m) \quad (4.5)$$

$$\text{Amagat: } z_m(P, T) = \sum_i x_i z_i(P_m, T_m) \quad (4.6)$$

where z_m and z_i are the compressibility factors of the mixture and component gases, respectively, and $x_i = n_i/n$ is the mole fraction of the component gas with respect to the mixture. Equation (4.5) implies that the compressibility factor of a gas mixture is approximated by the weighted average of the compressibility factors of the components, each evaluated at the appropriate partial pressure [5]. In contrast, Eqn. (4.6) implies the compressibility factors of the component gases are evaluated at the total pressure of the mixture.

The test gas used in these experiments is a mixture of sulfur hexafluoride (SF_6) and helium (He). The concentration of each gas in the mixture, if evaluated using Eqn. (4.5), is approximately 50% SF_6 and 50% He. On the other hand, if the properties are evaluated using Eqn. (4.6), the concentration of SF_6 and He is approximately 55% and 45%, respectively.

4.2.1 Shock Wave Theory

Creation of shock waves in a shock tube can be considered as a one-dimensional Riemann problem [6]. Initially, two gases at different pressures are separated by a thin membrane (or diaphragm). At time $t = 0$, the membrane is removed and the gases are allowed to come into contact. At this instant, a disturbance is formed as the high pressure gas moves towards the low pressure gas. This original disturbance splits into two opposite waves: a rarefaction (or expansion) wave and a compression (or

shock) wave. The rarefaction wave, which expands the gas at higher pressure, grows thicker while the shock wave, traveling through the low pressure gas at supersonic speed, grows thinner [7], accelerating and compressing the fluid. Shock waves can be described as discontinuities in fluid flow, in which properties such as density, pressure, and temperature increase instantaneously across the shock front. Since the regime is supersonic, properties in the low pressure gas (downstream of the shock wave) remain constant until the shock passes.

Generally, in shock wave analysis, a control volume is established containing the shock region and an infinitesimal amount of fluid on each side of the shock [8]. Applying the conservation equations for mass, momentum, and energy to this control volume (assuming steady, one-dimensional, adiabatic flow) result in three governing equations:

$$\rho_1 u_1 = \rho_2 u_2 \quad (4.7)$$

$$p_1 + \rho_1 u_1^2 = p_2 + \rho_2 u_2^2 \quad (4.8)$$

$$h_1 + \frac{1}{2}u_1^2 = h_2 + \frac{1}{2}u_2^2 \quad (4.9)$$

where ρ is the density of the fluid, u is the fluid velocity, p is the pressure, and h is the enthalpy. The subscripts 1 and 2 correspond to conditions before (downstream) and after (upstream) the shock, respectively. Equations (4.7) through (4.9) are referred to as the Shock Wave equations. The unknown variables in this case are ρ_2 , p_2 , u_2 , and the difference in enthalpy $\Delta h = h_2 - h_1$. Therefore, an additional equation is needed to solve the problem; the change in enthalpy equation, which is given by

$$dh = c_p dT + (1 - \alpha T) v dp \implies \Delta h = \int_1^2 c_p dT + \int_1^2 (1 - \alpha T) v dp \quad (4.10)$$

where c_p represents the specific heat at constant pressure, α is the isobaric thermal expansion coefficient, T is the temperature, and v is the specific volume [6]. In order

Chapter 4. Inv. of Dalton and Amagat's laws for gas mixtures with shock prop.

to characterize the properties of the gas mixture, Equation (4.10) requires the application of a thermodynamic model, such as either Dalton's law or Amagat's law. However, if the temperature T_2 , pressure p_2 , and velocity u_2 can be determined experimentally, Eqns. (4.7)-(4.10) can be solved directly and compared to theoretical predictions from both thermodynamic models.

Pressure measurements in a shock tube are relatively simple to acquire, through the use of high-frequency response pressure transducers (PTs). Various models and configurations of these transducers are commercially available. Temperature on the other hand, is a completely different story. The use of a thermocouple probe is an invasive procedure, which could drastically alter flow physics. Furthermore, there exist no commercially available thermocouples that possess the necessary response time (on the order of microseconds) and are robust enough to survive conditions within the shock tube. An alternative method of temperature measurement is required. This method must be non-invasive, so as to not disturb the flow within the shock tube, and it must have ultra-fast response times to accurately measure temperature across the shock wave. Infrared (IR) detectors offer a solution to both of these problems. They provide line-of-sight measurements of average temperature within the shock tube, and characteristic response times on the order of nanoseconds.

What follows is a description of an experimental setup in the Shock Tube Facility at the University of New Mexico Mechanical Engineering Department in which an infrared detector is used to provide temperature measurements both before and after shock passage. These experimental results are then compared with theoretical predictions of Dalton's law and Amagat's law in an effort to determine which law is more suitable for gas mixtures.

4.3 Experimental Arrangement and Diagnostics

The infrared detector used in these experiments (manufactured by InfraRed Associates, Inc.) utilizes an ultra-fast response liquid nitrogen (LN₂) cooled photoconductive mercury cadmium telluride (MCT) sensor, with a nominal operating temperature of 77 K. A response time of 60 nanoseconds makes this type of thermal sensor ideal for experiments conducted in a shock tube. However, each sensor is unique to the gas mixture tested and information about the infrared absorption (or transmission) spectrum of the gas itself is necessary. In order to obtain accurate results (and due to the sensitivity of the sensor itself), only a small fraction of the IR spectrum should be considered. This is accomplished by the use of a Germanium narrow band-pass filter mounted on the front of the sensor housing. Preliminary research [9] shows that peak absorption ($\sim 98\%$) of IR in sulfur hexafluoride (SF₆) occurs between $\lambda = 10 \mu\text{m}$ and $\lambda = 11 \mu\text{m}$ wavelength. However, absorption drops to $\sim 80\%$ in the range $7.5 \mu\text{m} \leq \lambda \leq 8.5 \mu\text{m}$. This wavelength range was chosen in an effort to properly characterize the amount of IR light transmitted (and absorbed) through the test gas.

LN₂-cooled IR sensors of this type measure line-of-sight transmission of infrared radiation. As the transmission of light through a participating medium decreases, the corresponding signal from the detector also decreases (which implies absorption of IR radiation increases). In order to analyze signals from the detector, it must be calibrated using the test gas, with known temperatures and pressures. Consequently, a calibration experiment was devised and implemented prior to any experiments conducted on the shock tube. Figure 4.1 shows the calibration experiment. The calibration cylinder seen in the center of the image consists of six main components: a small aluminum cylinder (4" in diameter, 0.5" thick) wrapped in an ultra-high temperature heater tape, a larger aluminum cylinder (7" in diameter, 0.5" thick),

two aluminum side plates, and two optical window mounts housing zinc selenide (ZnSe) windows, which operate as bandpass filters for infrared wavelengths between $\lambda = 7 \mu\text{m}$ and $\lambda = 12 \mu\text{m}$. The linear distance between the inner faces of the ZnSe windows is exactly 3 inches, which corresponds to the distance between the inside walls of the shock tube. The radiation source used in both the calibration and shock tube experiments is a Thorlabs SLS203L compact stabilized broadband infrared light source, with a color temperature of 1500 K.

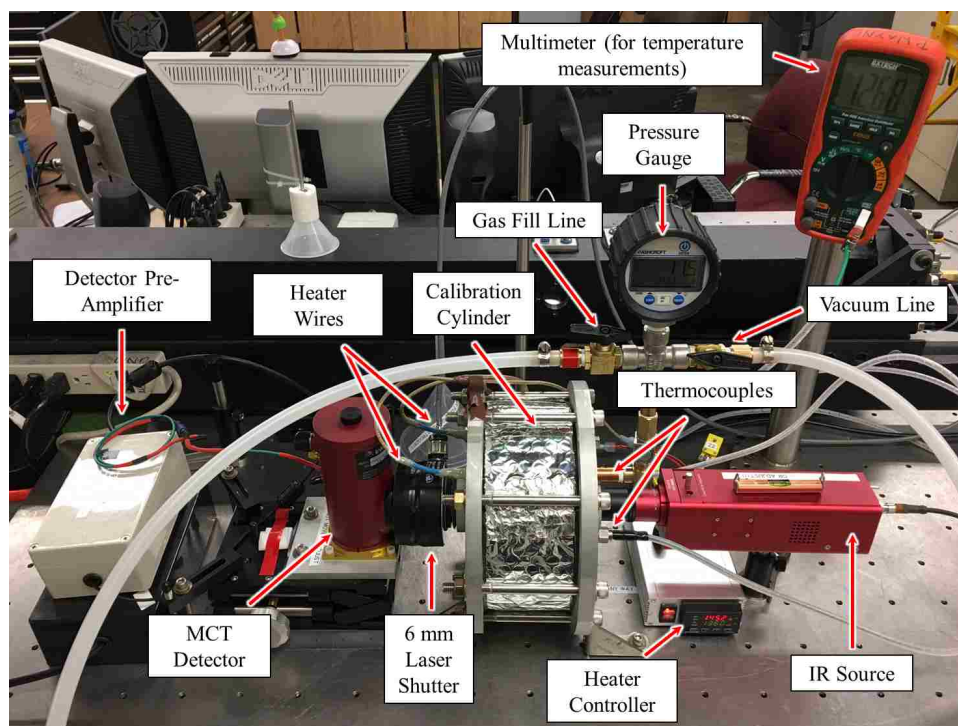


Figure 4.1: Experimental setup used to calibrate the MCT detector.

4.3.1 Calibration Procedure

Prior to each calibration experiment, the IR source is activated and allowed to stabilize for approximately 45 minutes. The glass dewar housing the MCT detector

(Fig. 4.1) is filled with liquid nitrogen and stabilized during this time period. If high temperature readings are needed, the heater tape is also activated via a PID (proportional-integral-derivative) heater temperature controller and allowed to reach thermal equilibrium at the prescribed temperature. The MCT detector and IR source are aligned perpendicular to the optical windows along the same axis. A Vincent Associates Uniblitz LS6 laser shutter (6 mm aperture, 1.7 ms open time) is placed along the optical axis in front of the MCT detector, which effectively simulates an instantaneous increase in temperature, as would be seen by the sensor when the shock wave passes. To maintain repeatability and reduce sources of error, the detector, shutter, and IR source are anchored in the same configuration for the duration of the calibration experiments.

The procedure begins with a thorough mixing of the SF₆/He test gas. The calibration cylinder inner chamber is completely evacuated using a vacuum pump (assuming a near-perfect vacuum). The gas mixture is then injected into the cylinder chamber to one of ten prescribed operating pressures. The laser shutter can then be activated at any time, allowing infrared radiation to pass from the source, through the test chamber containing the gas mixture, and onto the MCT sensor, located on the front of the glass dewar. The pre-amplified electrical signal from the detector is sent to a National Instruments USB-5132 digital oscilloscope and read by corresponding NI-Scope software. The signal (measured in Volts) from the detector is proportional to the amount of infrared radiation transmitted through the test gas (via emission from the gas itself and from the IR source). Assuming the test gas follows the theory of infrared absorption spectroscopy, the signal from the detector should decrease as the temperature of the gas in the calibration chamber increases.

Two thermocouples, mounted parallel to the optical axis, are placed inside the calibration cylinder test chamber. One thermocouple measures the temperature of the gas mixture, the other is used by the heater PID controller to maintain the

desired set temperature. Eight prescribed calibration temperatures were chosen, starting from room temperature ($\sim 22^\circ\text{C}$) to approximately 160°C , in 20°C increments. Six samples were taken for each pressure/temperature combination. The calibration pressures were chosen according to previous experiments of this type [6]; these pressures range from 5.70 psia to 86.0 psia.

4.3.2 Shock Tube Procedure

Figure 4.2 is an image showing the collective components used for conducting experiments in the shock tube. In order to maintain consistency, the infrared detector, ZnSe optical windows, infrared light source, and laser shutter are arranged in the exact same configuration as was used in the calibration experiment (including matching distances between components).

In the current configuration, the shock tube consists of two main sections, the driver section and the driven section. During each experiment, the driver and driven sections are separated by a thin-film (0.01" thick) polyester diaphragm. Each section is then evacuated using a vacuum pump until an assumed near-perfect vacuum is reached. The driver section is then filled with helium to a predetermined pressure (146 psia, 166 psia, or 186 psia) depending on the desired strength (or Mach number) of the shock wave. Once this pressure has been reached, the driven section is pressurized with the SF_6/He gas mixture to one of three prescribed pressures: 5.70 psia, 11.4 psia, and 17.1 psia (monitored by a digital pressure gauge, accurate to $\pm 0.25\%$). For reference, these correspond to the initial conditions for each test. Once this pressure has been reached and the driven section is allowed to stabilize, a pneumatically-driven stainless steel rod, tipped with a broad arrowhead is fired into the diaphragm, sending a planar shock down the length of the driven section. Four high-frequency response pressure transducers located on the top of the driven section

Chapter 4. *Inv. of Dalton and Amagat's laws for gas mixtures with shock prop.*

record the pressure pulse from the shock wave as it passes. These data can then be used to determine the shock speed (u_2) and corresponding pressure jump across the shock front (via manufacturer-supplied calibration curves). Ambient temperature

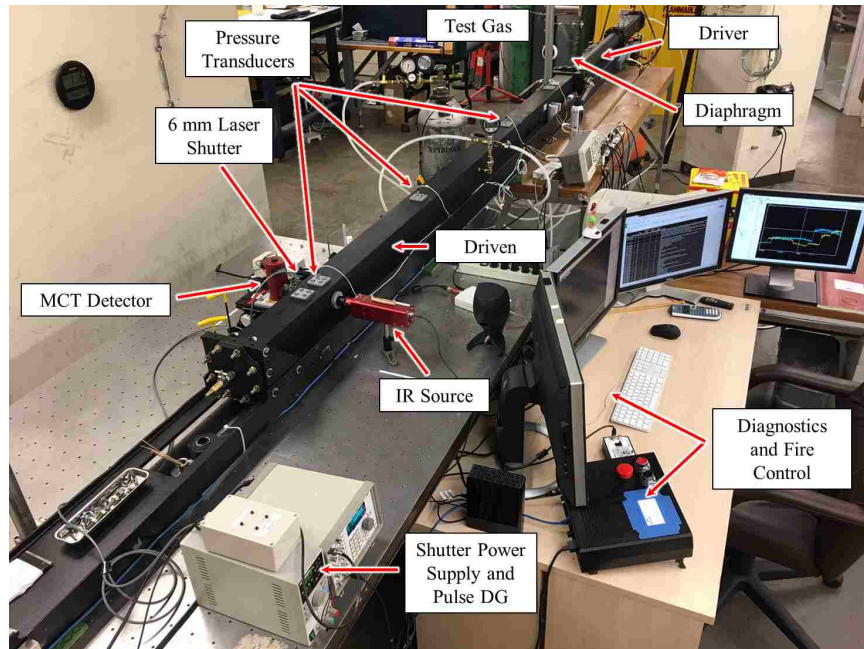


Figure 4.2: Shock tube experimental setup showing the driver and driven sections of the tube as well as the configuration of the detector and infrared source, located coincident with the 4th downstream pressure transducer.

readings (T_1) of the test gas (via the MCT detector) are taken just prior to the shot. These data, when combined with readings of temperature after shock passage (T_2) are used to determine the actual temperature jump across the shock front. The location of the detector is coincident with the position of the 4th pressure transducer, downstream of the diaphragm.

4.4 Results and Discussion

What follows is a summary of the process used to analyze and plot calibration curves for the detector, according to the prescribed pressure in the calibration cylinder. Calibration curves were obtained for each prescribed chamber pressure, both with and without radiation from the IR source. This allows characterization of IR emission from the test gas as well as absorption of infrared light.

The outline for shock tube experiments consists of testing three separate Mach numbers, each paired with three different initial pressures (5.70 psia, 11.4 psia, 17.1 psia) in the driven section of the shock tube. To clarify, the pressure in the driver section depends on the desired strength (or Mach number) of the shock wave; either 146 psia, 166 psia, or 186 psia. However, the actual speed of sound in the mixture is unknown. Therefore, the Mach number in each experiment can only be determined through post-processing and analysis.

Previous experiments [6] have shown that the pressure across the shock front, p_2 varies according to the strength of the shock wave and the initial conditions inside the driven section. In order to obtain accurate measurements of post-shock temperature T_2 during experiments, the infrared detector must be calibrated at each known value of p_2 . Table 4.1 outlines the various pressures tested during the calibration process.

Each data sample was imported into Matlab and filtered using a 50 point moving average Savitzky-Golay smoothing algorithm to reduce noise in the signal. Figure 4.3 is an example of the application of this algorithm, showing a drastic reduction in signal noise. The maximum value of each processed signal was determined and used to plot calibration curves. In order to minimize error, only the first 2 ms of the 10 ms total time window were chosen. These curves will be used to analyze temperature (and pressure) data obtained in the shock tube experiments.

Table 4.1: Pressures tested in the calibration process, according to driver pressure and initial conditions.

p_{driver} (psia)	Initial Conditions (p_1)	Calibration Chamber Pressure (p_c)
146	5.70 psia	48.0 psia
	11.4 psia	56.0 psia
	17.1 psia	61.0 psia
166	5.70 psia	56.0 psia
	11.4 psia	68.0 psia
	17.1 psia	74.0 psia
186	5.70 psia	61.0 psia
	11.4 psia	79.0 psia
	17.1 psia	86.0 psia

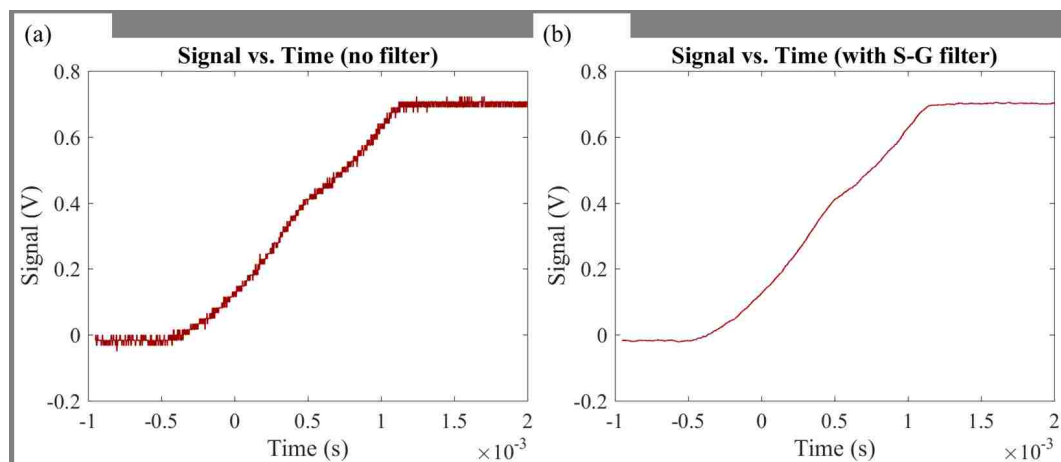


Figure 4.3: A sample signal from the MCT detector shown (a) before and (b) after application of the Savitzky-Golay smoothing algorithm.

Figure 4.4 is a calibration curve (both with and without the IR source) corresponding to a calibration cylinder chamber pressure of 48.0 psia. The x -axis is the temperature within the chamber ($^{\circ}\text{C}$), and the y -axis is the signal from the detector (V). Upward-facing triangles correspond to data obtained with the IR source, while dark blue squares correspond to data obtained without the IR source (self-emission of infrared from the test gas itself). Correlation coefficients (R^2) for both curves are also shown to demonstrate highly accurate linear curve fits.

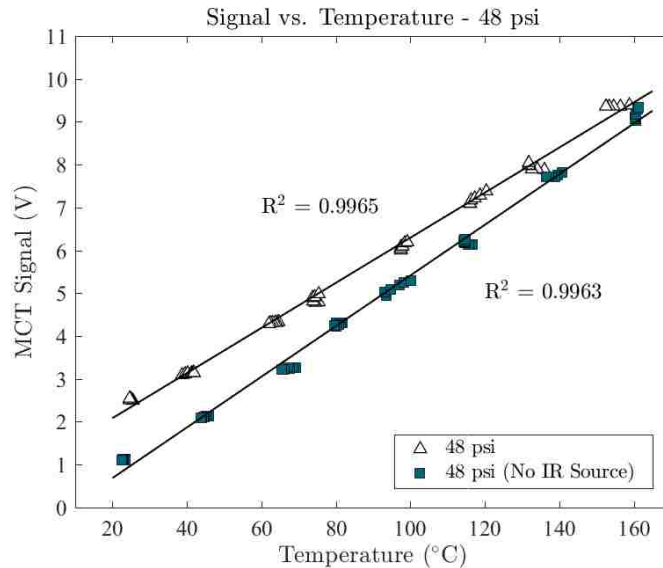


Figure 4.4: Calibration curve(s) generated using Matlab for 48.0 psia calibration cylinder chamber pressure. Upward facing triangles correspond to measurements taken with the infrared source and dark blue squares correspond to measurements taken with the source. Six samples at each temperature increment were taken.

4.5 Future Work

As this research is ongoing, future work will include experimental measurements of post-shock temperature in a gas mixture of sulfur hexafluoride and helium, subject to a moving normal shock. Figure 4.5 below is a preliminary sample trace showing the

response of the 4th downstream pressure transducer (blue line) and MCT detector (red line). Note that the MCT detector is placed coincident with the location of the pressure transducer. Here, increases in signal correspond to higher values of pressure and temperature. Driver and driven (test) pressures for this experiment were 166 psia and 11.4 psia, respectively.

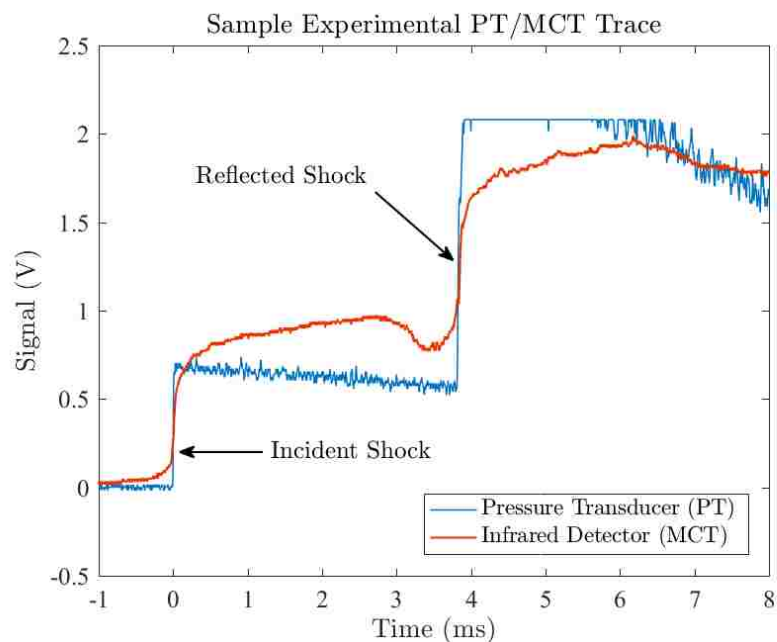


Figure 4.5: Sample graph of the pressure and temperature traces obtained in a shock tube experiment, with a driver pressure of 166 psia. The pressure of the test gas in the driven section was 11.4 psia (local atmospheric pressure).

Several concentrations of each component gas will be tested, including mixtures of 25%/75% and 75%/25% SF₆/Helium by molar mass, respectively. These data will be used to calculate speed of sound in the mixture and corresponding Mach number of the shock wave. The results will be compared with theoretical predictions using both Dalton's law of partial pressures and Amagat's law of partial volumes, in an effort to determine which law is more suitable.

References

- [1] J. Dalton, "Essay IV. On the expansion of elastic fluids by heat," *Memoirs of the Literary and Philosophical Society of Manchester*, vol. 5, pp. 595-602, 1802.
- [2] Y. A. Çengel, J. M. Cimbala, and R. H. Turner, *Fundamentals of Thermal Fluids Sciences*, McGraw-Hill, New York, New York, 4th ed., chap. 24, 2011.
- [3] H. Ran, and D. Mavris, "Preliminary design of a 2D supersonic inlet to maximize total pressure recovery," *AIAA 5th Aviation, Technology, Integration, and Operations Conference (ATIO)*, vol. AIAA 2005-7357, 2005.
- [4] Z. Liang, T. Curran, and J. E. Shepherd, *Structural Response to Detonating Loading in a 90-Degree Bend*, Springer Berlin Heidelberg, Berlin, Heidelberg, pp. 383-388, 2009.
- [5] K. W. Woo and S. I. Yeo, "Dalton's law vs. Amagat's law for the mixture of real gases," *The SNU Journal of Education Research*, pp. 127-134, 2011.
- [6] I. Trueba-Monje and J. H. Yoo, "Investigation of Dalton's law and Amagat's law for gas mixtures using shock wave propagation," *AIAA Region IV Student Conference*, Arlington, Texas, 2016.
- [7] P. O. Krehl, *History of Shock Waves, Explosions and Impact: A Chronological and Biographical Reference*, Springer-Verlag, New York, New York, chap. 3, 2008.
- [8] R. D. Zucker and O. Biblarz, *Fundamentals of Gas Dynamics*, John Wiley and Sons, Hoboken, New Jersey, 2002.
- [9] R. T. Lagemann and E. A. Jones, "The infrared spectrum of sulfur hexafluoride," *Journal of Chemical Physics*, vol. 19, no. 5, pp. 534-536, 1951.

Chapter 5

Dalton's and Amagat's laws fail in gas mixtures with shock propagation⁶

As a shock wave propagates through a gas mixture, pressure, temperature, and density increase across the shock front. Rankine-Hugoniot (R-H) relations quantify these changes, correlating post-shock quantities with upstream conditions (pre-shock) and incident shock Mach number [1, 2, 3, 4, 5]. These equations describe a calorically perfect gas, but deliver a good approximation for real gases, provided the upstream conditions are well-characterized with a thermodynamic mixing model. Two classic thermodynamic models of gas mixtures are Dalton's law of partial pressures and Amagat's law of partial volumes [6]. Here we show that neither thermodynamic model can accurately predict the post-shock quantities of interest (temperature and

⁶To be published as: P. Wayne, S. Cooper, D. Simons, I. Trueba-Monje, G. Vigil, D. Freelong, P. Vorobieff, C. R. Truman, V. Vorob'ev, and T. Clark, "Dalton's and Amagat's laws fail in gas mixtures with shock propagation," *Science Advances* (Under Review 8 July 2019), Manuscript No. aax4749.

pressure), on time scales much longer than those associated with the shock front passage, due to their implicit assumptions about behavior on the molecular level, including mixing reversibility. We found that in non-reacting binary mixtures of sulfur hexafluoride (SF_6) and helium (He), kinetic molecular theory (KMT) can be used to quantify the discrepancies found between theoretical and experimental values for post-shock pressure and temperature. Our results demonstrate the complexity of analyzing shock wave interaction with two highly disparate gases, while also providing starting points for future theoretical and experimental work and validation of numerical simulations.

5.1 Introduction

In 1802, John Dalton's publication in *Memoirs of the Literary and Philosophical Society of Manchester* formulated the law of additive (or partial) pressures [7], stating that the total pressure in a non-reactive gas mixture – at constant temperature and volume – is equal to the sum of the partial pressures of the component gases.

In 1880, French physicist Émile Hilaire Amagat published his findings while researching the compressibility of different gases [6]. Amagat's law of partial volumes states that the total volume of a gas mixture is equal to the sum of the partial volumes each gas would occupy if it existed alone at the temperature and pressure of the mixture [8]. While some advancements have been made in experiments of shock interaction with a single-component gas [9, 10], much less is known about multi-component gas mixtures.

Shock interactions with gas mixtures are relevant to many engineering problems, including gas-cooled reactor power plants [11, 12], mixing processes in supersonic and hypersonic combustion [13, 14, 15, 16], and astrophysical phenomena [17, 18]. Our

Chapter 5. Dalton's and Amagat's laws fail in gas mixtures with shock propagation

experiment was originally designed to determine which thermodynamic law (Dalton or Amagat) is more suitable for predicting properties of gas mixtures interacting with a planar shock wave. Post-shock properties are obtained using the Rankine-Hugoniot equations [1, 2, 3, 4, 5], which calculate post-shock values, such as pressure, temperature, and density, based on incident shock Mach number and upstream (pre-shock) conditions.

For a proper comparison of theoretical and experimental values of post-shock properties, pressure and temperature must be measured immediately before (downstream of), and immediately after (upstream of) the shock front. Pressure measurements are not difficult: high frequency response pressure transducers (PTs) are readily available. Temperature measurements are more challenging. Thermocouples are intrusive and lack the necessary response time [$\mathcal{O}(10^{-6})$ sec]. Infrared (IR) detectors, on the other hand, have ultra-fast response times [$\mathcal{O}(10^{-8})$ sec], and are inherently non-intrusive. Here we present temperature measurements using an Infrared Associates Mercury-Cadmium-Telluride (MCT), liquid-nitrogen-cooled infrared detector operating at 77 K, with a response time of 60 ns (60×10^{-9} sec). Coupled with a Thorlabs stabilized broadband infrared light source, with a color temperature of 1500 K, the MCT detector provides line-of-sight bulk temperature measurements both before and after the shock.

For our experiment, we selected two highly disparate gases forming a binary gas mixture: sulfur hexafluoride (SF_6) and helium (He). SF_6 and He are relatively inexpensive, non-toxic, and have highly contrasting properties: molecular weight, viscosity, specific heat, presenting an extreme (and hopefully easy to interpret) case of a mixture with easily distinguishable components. Two molar concentrations of each gas were chosen; 50%/50% (50/50) and 25%/75% (25/75) sulfur hexafluoride to helium respectively.

Chapter 5. Dalton’s and Amagat’s laws fail in gas mixtures with shock propagation

The shock tube consists of two sections: driver and driven. The driver section is pressurized (with nitrogen) to a value depending on the desired strength of the shock wave. The driven section is pressurized with the test gas mixture, up to one of 3 different initial pressures: 39.3 kPa, 78.6 kPa, or 118 kPa (the average local atmospheric pressure in the lab is approximately 78.6 kPa). A thin-film polyester diaphragm separates the two sections. Once both sections have been evacuated using a vacuum pump, the driver is then filled with the driver gas, and the driven section is filled with our test gas mixture. When the driver and driven sections are at the desired pressure, a pneumatically-driven stainless steel rod, tipped with a broad arrowhead, ruptures the diaphragm, sending a planar shock into the driven section. Four pressure transducers, located on the top of the driven section, record the pressure pulse from the shock wave as it passes. The MCT detector and IR source are located coincident with the 4th downstream pressure transducer, providing nearly instantaneous temperature measurements immediately before, and immediately after the shock. For details of experimental methods and theoretical evaluation of post-shock properties, refer to the Methods and Materials section.

Each gas mixture was tested at three driver pressures (1006 kPa, 1145 kPa, 1282 kPa), and each of these was applied to three initial pressures (39.3 kPa, 78.6 kPa, 118 kPa) in the driven section, providing experimental datasets at 9 distinct pressure ratios (overpressures P_r), where pressure ratio is defined as the ratio of driver pressure to the driven pressure ($P_r = P_{driver}/P_{driven}$). Figure 5.1A is an experimental signal trace at a pressure ratio of $P_r = 10.9$, for a 50%/50% mixture of SF₆/He.

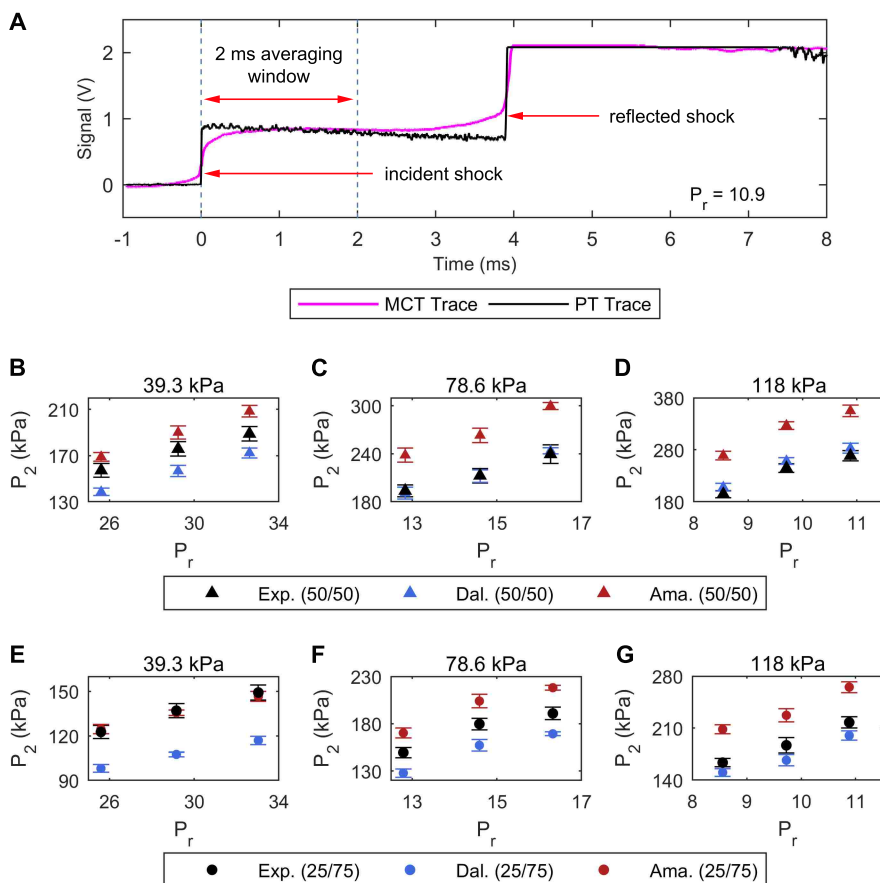


Figure 5.1: **Time history of recorded signals and post-shock pressure dependence on initial pressure ratio.** **A.** Sample pressure transducer (PT) and MCT detector signal traces, showing locations of incident and reflected shocks, as well as the 2 ms averaging window (dashed blue lines) used in data analysis. The black line is the signal trace from the 4th downstream PT, and the magenta line is the MCT signal trace. **B.-D.** Post-shock pressure, P_2 , versus pressure ratio, P_r for a 50/50 (by mole) binary mixture of SF_6 and helium, respectively. **E.-G.** Post-shock pressure versus pressure ratio for a 25/75 binary mixture of SF_6 and helium. In all panels (**B.-G.**), black symbols correspond to experimental values, blue symbols represent Dalton's law predictions, and red symbols denote Amagat's law predictions. Vertical error bars correspond to total uncertainty in post-shock pressure P_2 . Horizontal error bars are omitted as they do not extend past the physical size of the symbols. The driven pressure associated with each dataset is displayed above the corresponding panel.

The black line shows the signal (V) from the 4th downstream pressure transducer (PT), the magenta line – the signal (V) from the MCT detector. Average values of the signals from each PT are determined in a 2 millisecond window after shock impact (dashed blue line). This average value, combined with a calibration curve for each PT (provided by the manufacturer), provides us with the post-shock pressure, P_2 (kPa). To obtain the incident shock velocity, u_1 (m/s), the distance between two successive pressure transducers is divided by the time it takes the shock wave to travel between them. Measurements of temperature for the MCT are obtained by taking the maximum value of the signal within the same 2 ms window (Fig. 5.1A). A rigorous calibration experiment was conducted with the MCT detector and IR light source to determine post-shock temperature, T_2 (K).

5.2 Results

Multiple experiments were conducted for each gas mixture; a minimum of 6 experiments for each of the 9 pressure ratios. P_r ranges from 8.54 to 32.6 for the 50/50 SF₆/He mixture, and from 8.56 to 33.0 for the 25/75 SF₆/He mixture. Experimental results in Figs. 5.1-5.4 were produced by statistical analysis [19] of the dataset of measurements described above and correspond to mean values for each pressure ratio. Theoretical predictions are calculated as follows: the equations of state (EOS) are used to characterize the component gases. An ideal gas EOS is used for helium, while a virial expansion - up to the 4th virial coefficient - is used for sulfur hexafluoride. Inputs for the EOS are the initial pressure (P_1) and temperature (T_1) in the driven section of the shock tube. Once the components have been characterized (the process includes calculations of density, specific heat ratio, thermal expansion coefficient, isothermal compressibility, and speed of sound for both He and SF₆), we use Dalton's and Amagat's laws to determine thermodynamic coefficients for the gas

Chapter 5. Dalton's and Amagat's laws fail in gas mixtures with shock propagation

mixture. Specifically, we are interested in the specific heat ratio - γ - and the speed of sound - a . These values, combined with the incident shock speed (u_1), are used as inputs to the Rankine-Hugoniot equations, which are then used to determine post-shock temperature and pressure. Predictions displayed in Figs. 5.1-5.4 correspond to mean values for each pressure ratio. This process, and corresponding statistical analysis, is explained in detail in the Materials and Methods section.

Figure 5.1(B-G) are plots of post-shock pressure (P_2) versus pressure ratio (P_r) for the 50/50 mix (B,C,D) and the 25/75 mix (E,F,G). The corresponding initial pressures (in the driven section) are displayed above each panel (B-G). Vertical error bars correspond to total uncertainty in post-shock pressure. Horizontal error bars corresponding to uncertainty in pressure ratio (P_r) do not extend past the physical size of the symbols and are therefore omitted. Note the strong disagreement not only between experimental values and theoretical predictions, but also between the two mixture concentrations. Not only do these results disagree with both Dalton's law and Amagat's law well beyond experimental uncertainty, the disagreement varies with experimental value, leaving no clear answer: which law describes the experiment better overall?

Figure 5.2 shows the relationship between post-shock pressure (P_2) and incident shock speed (u_1) for A. the 50/50 SF₆/He mixture and B. the 25/75 SF₆/He mixture. In both plots, black symbols denote experimentally measured values, blue symbols correspond Dalton's law predictions, and red symbols represent Amagat's law predictions. Vertical error bars in both plots denote total uncertainty in post-shock pressure. Horizontal error bars (on experimental values) correspond to total uncertainty in incident shock speed. Note that horizontal error bars for both Dalton's and Amagat's laws are withheld, as the uncertainty in incident shock speed for both thermodynamic laws are identical to those for experimental measurements. Black arrows in Figs. 5.2A. and 5.2B. (upper left corner of each panel) show the direction

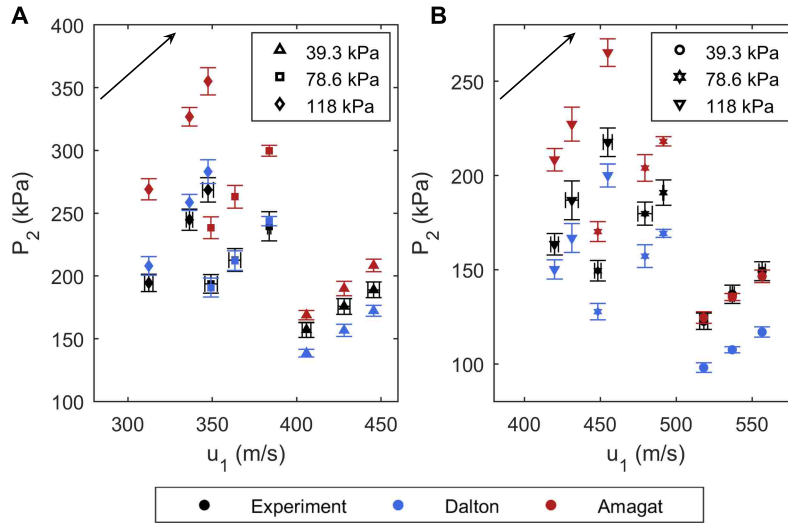


Figure 5.2: **Post-shock pressure variation with incident shock speed.** **A.** Post-shock pressure (P_2) versus incident shock speed (u_1) for a 50/50 (by mole) binary mixture of SF₆ to helium, respectively. **B.** Post-shock pressure versus incident shock speed for a 25/75 binary mixture of SF₆ to helium. In both plots, experimental values are given by black symbols, blue symbols correspond to Dalton's law predictions, and red symbols represent Amagat's law predictions. Black arrows show the direction of increasing driver pressure from 1006 kPa to 1282 kPa. Vertical error bars correspond to the total uncertainty in post-shock pressure P_2 (experimental measurements and theoretical predictions), which includes random and systematic uncertainties. Horizontal error bars correspond to total uncertainty in velocity measurements. Horizontal error bars for theoretical predictions are omitted, as the uncertainty in incident shock speed for both thermodynamic laws are identical to that of the experimental measurements.

Chapter 5. Dalton's and Amagat's laws fail in gas mixtures with shock propagation

of increasing driver pressure, from 1006 kPa to 1282 kPa. While it seems that experimental values are closer to Dalton's law predictions for the 78.6 kPa and 118 kPa data sets, data for 39.3 kPa is inconclusive. Again note the discrepancies between respective initial pressures and between the two mixtures. The next step is to evaluate post-shock temperature and compare with theoretical predictions.

Figure 5.3A. is a plot of post-shock temperature, T_2 , versus pressure ratio for the 50/50 SF₆/He mixture and Fig. 5.3B. is the same plot for the 25/75 SF₆/He mixture. Vertical error bars for experimental measurements and theoretical predictions correspond to total uncertainty in post-shock temperature. Note the inputs used to calculate predictions for both Dalton's and Amagat's laws are the initial pressure (P_1) and temperature (T_1) in the driven section of the shock tube, which are measured values. Therefore, these predictions will not fit smoothly on a curve; the curve fits shown in Fig. 5.3A. and 5.3B. serve merely as visual aids.

Again there is strong disagreement between experimentally obtained values of post-shock temperature and theoretical predictions. For the 50/50 mixture, it seems experimental values are closer to Dalton's law predictions, and for the 25/75 mixture, experimental values are closer to Amagat's law predictions; these discrepancies are not random. What could be responsible for this systematic disagreement?

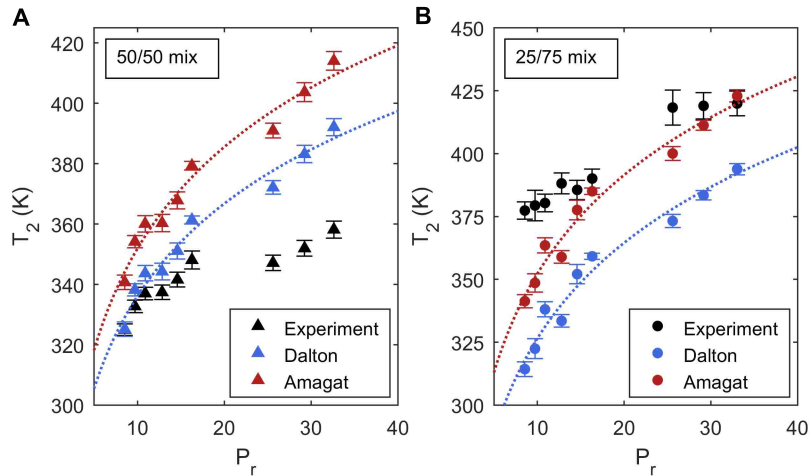


Figure 5.3: **Post-shock temperature dependence on initial pressure ratio.** In both plots, black symbols correspond to experimental values, blue symbols represent to Dalton's law predictions, red symbols denote Amagat's law predictions. Blue and red dotted lines in both plots are curve fits to Dalton's and Amagat's law predictions, respectively; they are simply used as guides to the eye. Vertical error bars correspond to total uncertainty in post-shock temperature T_2 , which includes both random and systematic uncertainties. **A.** post-shock temperature (T_2) versus pressure ratio (P_r) for a 50/50 binary mixture of SF_6 to helium. Here, experimental values are closer to Dalton's law predictions. **B.** post-shock temperature versus pressure ratio for a 25/75 binary mixture of SF_6 to helium. In contrast to data presented in **A**, experimental values for a 25/75 mixture are closer to Amagat's law predictions.

5.3 Discussion

A compelling theoretical analysis of finite-strength shock propagation through a binary gas mixture was published by Sherman [20] (1960) for inert gas mixtures consisting of argon (Ar) and helium (for a range of molar concentrations of each component). Using a continuum approach, Sherman focused on determining the structure of a shock wave of arbitrary strength, which includes ordinary-, baro-, and thermal-diffusion effects. He concluded that baro-diffusion speeds up the heavier component, and slows down the lighter component relative to the mass velocity of

the mixture [20]. He also determined thermal-diffusion will have the opposite effect, slowing down the heavier component and speeding up the lighter. Therefore, thermal diffusion would (at least partially) counteract baro-diffusion within the shock wave. Sherman calculated his results through numerical integration of the Navier-Stokes equations. A primary assumption associated with this analysis was in always imposing thermal equilibrium between species through the shock wave. However, Sherman indicates these assumptions (and corresponding analysis) may not be valid for strong shock waves, or for mixtures with large molecular mass ratios. In fact, he states that one might intuitively expect that the maximum shock strength for which these calculations give realistic predictions would be reduced (somewhat significantly) as the molecular mass ratio increases, due to the difficulty in maintaining thermal equilibrium between the gas components [20].

In 1967, Bird [21] produced an interesting attempt to model shock propagation through a binary mixture of 50/50 Ar-He, representing the gas molecules as rigid elastic spheres - with the appropriate masses and diameters - and compared his results with the analytical predictions of Sherman. His model did not have the same temperature constraints as Sherman, and predicted even greater differences in velocity, temperature, and concentration profiles than the analytical profiles of Sherman. Furthermore, Bird's findings suggest the temperature non-equilibrium between species increases with low concentrations of the heavy gas component and that this [non-equilibrium] can persist for a considerable distance downstream of the shock [21]. For reference, the molecular mass ratio with respect to binary mixtures of Ar-He is approximately 10, while the molecular mass ratio associated with the current work (SF₆ - He) is around 36.5.

The studies conducted by Sherman and Bird reasonably concluded that shock propagation through gas mixtures with relatively massive molecules would cause differences in their behavior, but the results only pertained to gas molecule velocity,

concentration, and temperature profiles - on time (and length) scales much smaller than these considered in the current work. Perhaps the results shown in Figs. 5.1-5.3, taken in context with these early studies, suggest a different explanation, beyond experimental uncertainty.

Is a kinetic molecular theory (KMT) [22, 23] explanation possible? Dalton's and Amagat's laws predate KMT, but each law makes implicit assumptions about reversibility. Both laws assume thermodynamic equilibrium. However, while Dalton's law assumes the gases are always perfectly mixed, Amagat's law assumes the gases will separate over time. This assertion is interesting because that is exactly what we see in experiments. The molecular mass of sulfur hexafluoride is approximately 36.5 times greater than that of helium. If the gases are not constantly mixed, they will begin to separate (under normal conditions, the gases will separate within a few minutes). Prior to taking measurements described here, our initial guess was that Amagat's law might provide a better prediction for these dissimilar gases. The time scale of that separation, however, is much longer than the time scale of the experiment associated with the shock passage, thus leading to both Dalton's law (infinite separation time) and Amagat's law (the gases in the mixture are in effect always separated) failing to produce a match with experiment.

What relaxation time scale is relevant for the equilibrium status of a shocked gas mixture? Relaxation time is defined as the time within which a perturbed gas will reach statistical (thermodynamic) equilibrium [24]. In binary gas mixtures whose constituents have widely different molecular masses ($M_{SF_6} \gg M_{He}$), disparate relaxation times are manifest, governing the approach to equilibrium of the various degrees of freedom [25]. According to Mora and Fernández-Feria [25], for such mixtures, the process of equilibration can be characterized by three different relaxation times: two for self-equilibration of the component gases, and a third one associated with the slower process of interspecies equilibration. For this analysis, these relax-

ation times are the post-shock mean free time (or average time between molecular collisions) for each of the gas components (τ_{He} and τ_{SF_6}) and the change in collision time between them ($\Delta\tau = \tau_{He} - \tau_{SF_6}$). What is remarkable about this method is that the mean free time is temperature and pressure dependent (see Methods).

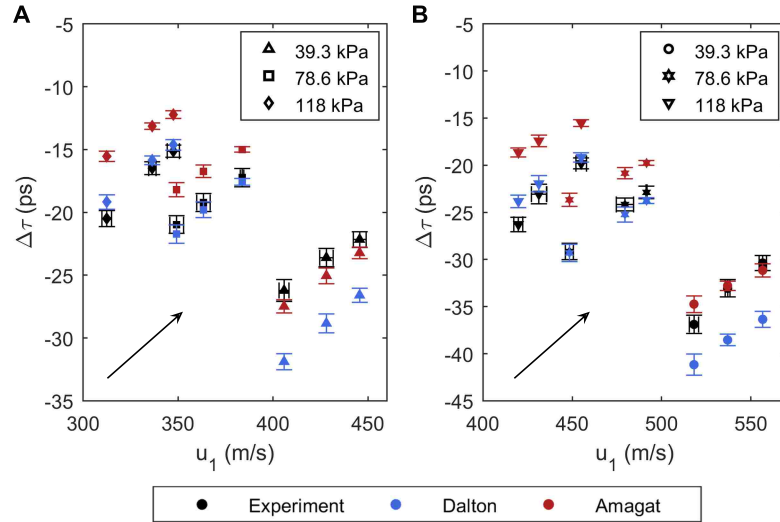


Figure 5.4: **Kinetic theory correlations with incident shock speed.** **A.** change in collision time, $\Delta\tau = \tau_{He} - \tau_{SF_6}$, for a 50/50 (by mole) binary mixture of SF₆ to helium, respectively. **B.** change in collision time for a 25/75 binary mixture of SF₆ to helium. In both plots, experimental values are given by black symbols, blue symbols denote Dalton's law predictions, and red symbols represent Amagat's law predictions. Vertical error bars correspond to total uncertainty in $\Delta\tau$, and horizontal error bars correspond to total uncertainty in velocity measurements. Similar to Fig. 5.2, horizontal error bars for theoretical predictions are omitted, and black arrows show the direction of increasing driver pressure from 1006 kPa to 1282 kPa. These data closely resemble the trends we observe above (Figs. 1-3).

Figure 5.4 is a plot of the change in collision time, $\Delta\tau$ (in picoseconds), versus incident shock velocity (u_1) for A. the 50/50 SF₆/He mixture and B. the 25/75 SF₆/He mixture. Symbol type and color in Fig. 5.4 have been arranged similar to Fig. 5.2. Again, the black arrow in both plots points in the direction of increasing driver pressures. Note again the systematic discrepancies in these data, consistent

with the spread of experimental data points. The negative values for $\Delta\tau$ are due to the fact that the average collision time for SF_6 is an order of magnitude greater than that of He. While Figs. 5.1-5.3 show discrepancies produced by Dalton's and Amagat's laws in predicting post-shock properties (pressure and temperature) on a macroscopic scale, Fig. 5.4 provides a context for these discrepancies, relating them to the simplest quantitative parameter describing the disparity between component gas behavior on a microscopic scale. Therefore, if the component gases behave differently, i.e. have a large difference in response time, on a microscale, is it not reasonable to assume these discrepancies manifest on a macroscale? This hypothesis is reinforced by the results obtained from Sherman [20] and Bird [21], especially considering the large molecular mass difference between the species.

The simple explanation that kinetic molecular theory can provide is that differences in the response time of the molecules account for the disagreement between theory and experiment. This explanation appears to agree with our data, at least qualitatively. These observations show that Dalton's and Amagat's laws fail to accurately describe the behavior of a gas mixture that underwent shock acceleration, with implications that the same failure can manifest in other non-equilibrium situations.

5.4 Materials and Methods

5.4.1 Experimental setup

Two gas mixtures were tested: 50%/50% and 25%/75% sulfur hexafluoride (SF_6) to helium (He), by mole, respectively. Experiments were conducted at the Shock Tube Facility in the Mechanical Engineering Department at the University of New Mexico (UNM). The shock tube itself is approximately 5.2 m long, with a 2 m long driver

section, and a 3.2 m long driven section (7.62 cm inside square cross-section).

To begin an experiment, we separate the driver and driven sections of the shock tube with a thin-film polyester diaphragm. Both sections are then evacuated using an ITT Pneumotive vacuum pump to -78.6 kPa. The driven (test) section is filled with the test mixture to a predetermined pressure (39.3 kPa, 78.6 kPa, or 118 kPa). The driver is filled with nitrogen to another predetermined pressure (1006 kPa, 1145 kPa, or 1282 kPa). The pressure in the driver section depends on the desired strength (or Mach number) of the shock wave [6]. Once the pressure in both sections has stabilized, a pneumatically-driven stainless steel rod tipped with a broad arrowhead punctures the diaphragm, sending a normal shock down the length of the driven section. Four pressure transducers (with a response time $\leq 1 \mu\text{s}$), located on the top of the driven section (≈ 0.8 meters apart), record the pressure history of the shock wave as it passes. These data can then be used to determine the velocity of the shock wave, u_1 , and the post-shock pressure, P_2 . The MCT detector and IR source are placed on opposite sides of the shock tube, perpendicular to the optical axis and located coincident with the 4th downstream pressure transducer. Two zinc selenide (ZnSe) optical windows are placed on either side of the shock tube, mounted flush with the inside of the test section. These optical windows are used to create an airtight, unobstructed light path from the IR source, through the test gas in the driven section, to the sensor on the MCT detector. They are also used as broadband filters to decrease the wavelength range of the incoming light from the IR source to between $7 \mu\text{m}$ and $12 \mu\text{m}$ (the IR source outputs light between $0.5 \mu\text{m}$ and approximately $20 \mu\text{m}$). A germanium notch filter, mounted on the MCT detector itself, further reduces the range of incoming light to between $7.5 \mu\text{m}$ and $9.0 \mu\text{m}$. Note the target range for these experiments was chosen between $7.5 \mu\text{m}$ and $8.5 \mu\text{m}$, based on the infrared absorption spectrum of sulfur hexafluoride [26].

Calibration curves that relate the signal (V) from the pressure transducers to

pressure (kPa) in the driven section are provided for each transducer by the manufacturer. For the MCT detector, a calibration experiment was conducted to determine the relationship between signal (V) and temperature (K). This experiment used an aluminum cylinder with ZnSe optical windows mounted on each side, with components and geometry identical to that of the shock tube setup described above. The cylinder chamber is evacuated with a vacuum pump and filled with the test gas mixture at a prescribed pressure (target pressures were determined from previous experiments [27]). A helical coil resistance heater, placed on the inside of the calibration cylinder, is then activated to increase the temperature of the test gas to a predetermined value. A Vincent Associates Uniblitz LS6 laser shutter (6 mm aperture, 1.7 ms open time) is placed along the optical axis in front of the MCT detector, which effectively simulates an instantaneous increase in temperature, as would be seen by the sensor when the shock wave passes [6]. Once the laser shutter is activated, the signal from the detector is recorded and used as a baseline for that pressure-temperature (P-T) combination. For each gas mixture, data was obtained at up to 25 P-T combinations, with a minimum of six measurements at each combination. This method provided ample data to determine a calibration curve for each gas mixture.

5.4.2 Thermodynamic models

The following theoretical analysis was used to determine post-shock pressure and temperature for both Dalton's and Amagat's laws. Equations of state (EOS) are needed to characterize the gas components; the Ideal Gas (Eqn. 1) EOS was used

Chapter 5. Dalton's and Amagat's laws fail in gas mixtures with shock propagation

for helium and a virial expansion (Eqn. 2) was used for sulfur hexafluoride.

$$P\nu = RT \quad (5.1)$$

$$P = \frac{RT}{\nu} \left(1 + \frac{B(T)}{\nu} + \frac{C(T)}{\nu^2} + \frac{D(T)}{\nu^3} + \frac{E(T)}{\nu^4} \right) \quad (5.2)$$

Here, P is the pressure (N/m²), ν is the specific volume (m³/mol), $R = 8.314$ J/mol-K is the universal gas constant, T is the temperature (K), $B(T)$ is the second virial coefficient, $C(T)$ is the third virial coefficient, and so forth [28]. Algebraic expressions of the temperature provided by the hard-core square well (HCSW) model intermolecular potential are used to represent $B(T)$ and $C(T)$, while $D(T)$ and $E(T)$ are represented as polynomial functions of the inverse temperature [29].

$$B(T) = b_0[1 - (\lambda^3 - 1)\Delta] \quad (5.3)$$

$$C(T) = \frac{1}{8}b_0^2(5 - c_1\Delta - c_2\Delta^2 - c_3\Delta^3) \quad (5.4)$$

$$D(T) = \sum_{n=0}^3 d_n T^{-n} \quad (5.5)$$

$$E(T) = \sum_{n=0}^3 e_n T^{-n} \quad (5.6)$$

where $\Delta = e^{\epsilon/k_b T} - 1$ (k_b is Boltzmann's constant) and the coefficients c_1 , c_2 , and c_3 are given by

$$c_1 = \lambda^6 - 18\lambda^4 + 32\lambda^3 - 15 \quad (5.7)$$

$$c_2 = 2\lambda^6 - 36\lambda^4 + 32\lambda^3 + 18\lambda^2 - 16 \quad (5.8)$$

$$c_3 = 6\lambda^6 - 18\lambda^4 + 18\lambda^2 - 6 \quad (5.9)$$

Values for d_n ($n = 1, 2, 3$), e_n ($n = 1, 2, 3$), b_0 , λ , and ϵ/k_b are provided by Hurly et al [29].

Inputs for the EOS are the initial pressure (P_1) and temperature (T_1) of the test gas in the driven section. Once the component gases have been characterized, we use Dalton's law and Amagat's law to determine thermodynamic coefficients for the mixture. We are specifically looking for the speed of sound a , and the specific heat ratio, γ . These variables, coupled with the incident shock speed u_1 (determined from experiment) are used as inputs for the Rankine-Hugoniot equations (Eqns.10-13), which relate post-shock properties in terms of initial conditions (pre-shock) and incident shock Mach number M_1 .

$$M_1 = \frac{u_1}{a} \quad (5.10)$$

$$M_2^2 = \frac{M_1^2 + 2/(\gamma - 1)}{[2\gamma/(\gamma - 1)] M_1^2 - 1} \quad (5.11)$$

$$T_1 \left(1 + \frac{\gamma - 1}{2} M_1^2 \right) = T_2 \left(1 + \frac{\gamma - 1}{2} M_2^2 \right) \quad (5.12)$$

$$\frac{P_1}{P_2} = \frac{1 + \gamma M_2^2}{1 + \gamma M_1^2} \quad (5.13)$$

The subscripts 1 and 2 correspond to conditions before and after the shock, respectively. Once the post-shock temperature (T_2) and pressure (P_2) for each thermodynamic law (Dalton and Amagat) have been calculated, we can directly compare the results with experimental values. All theoretical calculations and analysis of experimental data (including statistical analysis) were performed in MATLAB.

5.4.3 Kinetic molecular theory

Central to kinetic molecular theory are the following assumptions [30]:

- The size of the particle is negligibly small, i.e. the particles themselves occupy no volume, even though they have mass. At the maximum concentration of

Chapter 5. Dalton's and Amagat's laws fail in gas mixtures with shock propagation

molecules in our experiments, the Van der Waals correction to pressure associated with molecular volume would not exceed 2.5%.

- The average kinetic energy of a particle is proportional to the temperature (K).
- Particle collisions are perfectly elastic; they may exchange energy, but there is *no overall loss of energy*.

The following equations were used for kinetic theory analysis. The mean free path (l) is given by

$$l = \frac{k_b T}{\sqrt{2} \pi d^2 P} \quad (5.14)$$

where $k_b \approx 1.381 \times 10^{-23} \text{ m}^2 \text{ kg s}^{-2} \text{ K}^{-1}$ is the Boltzmann constant, T is the temperature (K), d is the kinetic diameter, which for helium is $0.260 \times 10^{-9} \text{ m}$ and for SF_6 is $0.550 \times 10^{-9} \text{ m}$, and P is the pressure (Pa).

Mean molecular speed (μ_m) is obtained via

$$\mu_m = \sqrt{\frac{8TR_s}{\pi}} \quad (5.15)$$

where R_s is specific gas constant: for helium, $R_s = 2.0773 \times 10^{-3} \text{ J/kg-K}$, and for SF_6 , $R_s = 56.9269 \text{ J/kg-K}$.

Average collision time (τ) is calculated using

$$\tau = \frac{l}{\mu_m} \quad (5.16)$$

The change in average collision time, $\Delta\tau$ is simply the average collision time of helium, τ_{He} , minus the average collision time of sulfur hexafluoride, τ_{SF_6}

$$\Delta\tau = \tau_{He} - \tau_{SF_6} \quad (5.17)$$

5.4.4 Statistical analysis

A comprehensive statistical analysis was performed on all experimental data, according to steps outlined in Wheeler and Ganji [19].

Statistical analysis on all measurements (pressure, temperature, and velocity) begins with outlier rejection using the Modified Thompson Tau technique [19]. In this method, for any n measurements, with a mean value \bar{x} and standard deviation S , the data is arranged in ascending order (x_1, x_2, \dots, x_n). The extreme (highest and lowest) values are suspected outliers. For these suspected points, a deviation is calculated as

$$\delta_i = |x_i - \bar{x}| \quad (5.18)$$

and the largest value is selected. This value is compared with the product of τ (tabulated with respect to n) times the standard deviation S . If the value of δ exceeds τS , then this value can be rejected as an outlier (only one value is eliminated for each iteration). The mean and standard deviation of the remaining values are then recomputed and the process is repeated until no more outliers exist. Note that n decreases with each outlier rejection.

Pressure measurements were obtained using multiple devices. Therefore, an estimation of the combined degrees of freedom according to the Welch-Satterthwaite formula (Eqn. 18) is necessary [19].

$$\nu_x = \frac{\left[\sum_{i=1}^m S_i^2 \right]^2}{\sum_{i=1}^m (S_i^4 / \nu_i)} \quad (5.19)$$

where ν_i is the degrees of freedom for the measuring device, and ν_x is the value of the combined degrees of freedom for variable x . Degrees of freedom for temperature and velocity measurements is simply $\nu_x = n - 1$. When ν_x has been determined, the

students t-distribution value (t) is found based on a 95% level of confidence. The total random uncertainty in the mean value $P_{\bar{x}}$ is computed by

$$P_{\bar{x}} = \pm \frac{S_x}{\sqrt{n}} \quad (5.20)$$

where S_x/\sqrt{n} is the estimate of the standard deviation of the mean.

Systematic uncertainty for each variable is determined using the mean value for the measurement and manufacturer supplied information, such as linearity, hysteresis, and uncertainty in the measuring device. Sources of systematic error are pressure transducers, pressure gauges, oscilloscopes, and the MCT detector. Total systematic error is given by

$$B_x = \left[\sum_{i=1}^k B_i^2 \right]^{1/2} \quad (5.21)$$

where B_i is the systematic error for measuring device i . Once all sources of random and systematic error have been determined, the total uncertainty in the mean ($W_{\bar{x}}$) is given by

$$W_{\bar{x}} = (B_x^2 + P_{\bar{x}}^2)^{1/2} \quad (5.22)$$

The mean value for a given set of measurements is used in all plots, and error bars represent total uncertainty (\pm) in the mean value.

Table 5.1 details the number of measurements n , degrees of freedom ν (combined or otherwise), and the t -distribution value for post-shock pressure P_2 , incident shock speed u_1 , and post-shock temperature T_2 , for the 50/50 binary mixture of SF₆ and helium. P_r denotes the pressure ratio according to mean values of driver and driven pressures for a given set of experiments. Table 5.2 details statistics for a 25/75 mixture of SF₆ and helium. All statistical analysis was performed in MATLAB.

Chapter 5. Dalton's and Amagat's laws fail in gas mixtures with shock propagation

Table 5.1: Statistical information of experimental measurements for a 50/50 binary mixture of SF₆ and helium, where n is the number of samples, ν is the degrees of freedom (combined or otherwise), and t is the student's t -distribution value.

P_r (50/50)	n_{P_2}	ν_{P_2}	t_{P_2}	n_{u_1}	ν_{u_1}	t_{u_1}	n_{T_2}	ν_{T_2}	t_{T_2}
32.61	15	6	2.4469	5	4	2.7764	5	4	2.7764
16.27	23	10	2.2281	4	3	3.1824	7	6	2.4469
10.88	20	10	2.2281	6	5	2.5706	5	4	2.7764
29.24	20	16	2.1199	5	4	2.7764	6	5	2.5706
14.60	21	11	2.2010	5	4	2.7764	5	4	2.7764
9.70	21	10	2.2281	5	4	2.7764	6	5	2.5706
25.60	22	15	2.1314	6	5	2.5706	6	5	2.5706
12.83	22	15	2.1314	5	4	2.7764	6	5	2.5706
8.54	22	17	2.1098	6	5	2.5706	6	5	2.5706

Chapter 5. Dalton's and Amagat's laws fail in gas mixtures with shock propagation

Table 5.2: Statistical information of experimental measurements for a 25/75 binary mixture of SF₆ and helium, where n is the number of samples, ν is the degrees of freedom (combined or otherwise), and t is the student's t -distribution value.

P_r (25/75)	n_{P_2}	ν_{P_2}	t_{P_2}	n_{u_1}	ν_{u_1}	t_{u_1}	n_{T_2}	ν_{T_2}	t_{T_2}
33.03	20	12	2.1788	6	5	2.5706	6	5	2.5706
16.32	24	20	2.0860	4	3	3.1824	5	4	2.7764
10.88	18	8	2.3060	6	5	2.5706	6	5	2.5706
29.16	28	21	2.0796	6	5	2.5706	6	5	2.5706
14.59	19	10	2.2281	6	5	2.5706	6	5	2.5706
9.73	21	12	2.1788	6	5	2.5706	6	5	2.5706
25.59	21	11	2.2010	6	5	2.5706	6	5	2.5706
12.79	20	13	2.1604	4	3	3.1824	6	5	2.5706
8.56	18	10	2.2281	6	5	2.5706	6	5	2.5706

References

- [1] F. White, *Fluid Mechanics* (McGraw-Hill, Boston, MA, 2003).
- [2] R. Zucker, O. Biblarz, *Fundamentals of Gas Dynamics* (Wiley, Hoboken, NJ, 2002).
- [3] E. Goldman, L. Sirovich, The structure of shock-waves in gas mixtures. *J. Fluid Mech.* **35**, 575-597 (1969).
- [4] J. Anderson, *Modern Compressible Flow With Historical Perspective* (McGraw-Hill, New York, 1982).
- [5] J. John, *Gas Dynamics* (Prentice-Hall, New Jersey, 1984).
- [6] P. Wayne, S. Cooper, D. Simons, I. Trueba-Monje, J. H. Yoo, P. Vorobieff, C. R. Truman, S. Kumar, Investigation of Dalton's and Amagat's laws for gas mixtures with shock propagation. *Int. J. Comp. Meth. and Exp. Meas.* **6**, 1-10 (2017).
- [7] J. Dalton, Essay IV. On the expansion of elastic fluids by heat. *Mem. Proc. - Manch. Lit. Philos. Soc.* **5** (1802).
- [8] Y. Çengel, J. Cimbala, R. Turner, *Fundamentals of Thermal-Fluid Sciences* (McGraw-Hill, New York, 2011).
- [9] L. Bernstein, "Tabulated solutions of the equilibrium gas properties behind the incident and reflected normal shock-wave in a shock tube" (C.P. No. 626, Ministry of Aviation, Aeronautical Research Council Current Papers, 1963).
- [10] L. Davies, D. Edwards, "An experimental investigation of the reflected-shock pressure-time profiles in air, oxygen, nitrogen, argon, carbon dioxide and acetylene" (R. & M. No. 3446, Ministry of Aviation, Aeronautical Research Council Reports and Memoranda, 1967).

References

- [11] J. Tournier, M. El-Genk, Noble gas binary mixtures for gas-cooled reactor power plants. *Nucl. Eng. Des.* **238**, 1353-1372 (2008).
- [12] J. Diaz, Preface gaseous core reactors. *Nucl. Technol.* **69**, 129-133 (1985).
- [13] A. Ferri, G. Moretti, S. Slutsky, Mixing processes in supersonic combustion. *J. Soc. Ind. Appl. Math.* **13**, 229-258 (1965).
- [14] C. Gruenig, F. Mayinger, Supersonic combustion of Kerosene/H₂-mixtures in a model scramjet combustor. *Combust. Sci. and Tech.* **146**, 1-22 (1999).
- [15] J. Tao, Studies of a combined way of flame stability in ramjet combustor. *Def. Technol.* **14**, 441-445 (2018).
- [16] F. Marble, E. Zukoski, J. Jacobs, G. Hendricks, I. Waitz, Shock enhancement and control of hypersonic mixing and combustion. *American Institute of Aeronautics and Astronautics*, AIAA 90-1981 (1990).
- [17] P. Lorén-Aquilar, M. Bate, Two-fluid dust and gas mixtures in smoothed particle hydrodynamics II: an improved semi-implicit approach. *Mon. Not. R. Astron. Soc.* **454**, 4114-4119 (2015).
- [18] R. Anand, On dynamics of imploding shock waves in a mixture of gas and dust particles. *Int. Journ. of Non-Linear Mech.* **65**, 88-97 (2014).
- [19] A. Wheeler, A. Ganji, *Introduction to Engineering Experimentation* (Prentice Hall, New Jersey, 2010).
- [20] F. Sherman, Shock-wave structure in binary mixtures of chemically inert perfect gases. *J. of Fluid Mech.* **8**, 465-480 (1960).
- [21] G. Bird, The structure of normal shock waves in a binary gas mixture. *J. of Fluid Mech.* **31**, 657-668 (1968).
- [22] L. Loeb, *The Kinetic Theory of Gases* (Dover Publications, New York, 1961).
- [23] C. Collie, *Kinetic Theory and Entropy* (Longman Inc., New York, 1982).
- [24] L. Landau, E. Lifshitz, *Statistical Physics* (Pergamon Press, New York, 1980).
- [25] J. Mora, R. Fernández-Feria, Kinetic theory of binary gas mixtures with large mass disparity. *Phys. Fluids* **30**, 740 (1987).
- [26] R. Lagemann, E. Jones, The infrared spectrum of sulfur hexafluoride. *J. Chem. Phys.* **19**, 534 (1951).

References

- [27] I. Trueba-Monje, J. Yoo, paper presented at the AIAA Region IV Student Conference, Houston, TX, April 2016.
- [28] H. Callen, *Thermodynamics and An Introduction to Thermostatistics* (Wiley, New York, 1985).
- [29] J. Hurly, D. Defibaugh, M. Moldover, Thermodynamic properties of sulfur hexafluoride. *Int. J. Thermophys.* **21**, 739-765 (2000).
- [30] N. Tro, *Chemistry: A Molecular Approach* (Prentice Hall, New Jersey, 2011).